

AD-A100 824

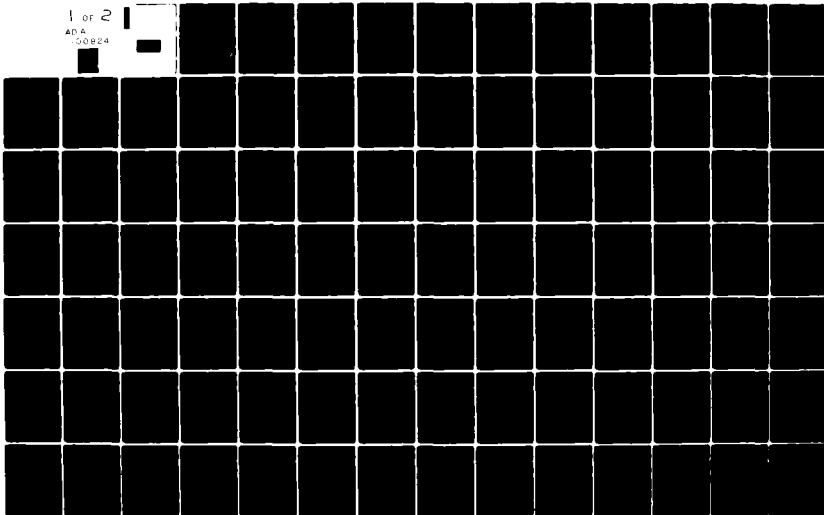
AIR FORCE INST OF TECH WRIGHT-PATTERSON AFB OH SCHOO--ETC F/6 20/4  
THE NUMERICAL SOLUTION OF INCOMPRESSIBLE TURBULENT FLOW OVER AI--ETC(U  
FEB 81 H A HEGNA.

UNCLASSIFIED

AFIT/DS/AA/81-1

NL

1 OF 2  
ADA  
100824



Accession For	
NTIS GRA&I	<input checked="" type="checkbox"/>
DTIC TAB	<input type="checkbox"/>
Unannounced	<input type="checkbox"/>
Justification	
By _____	
Distribution/ _____	
Availability Codes _____	
Avail and/or	
Dist	Special
A	

THE NUMERICAL SOLUTION OF INCOMPRESSIBLE  
TURBULENT FLOW OVER AIRFOILS

DISSERTATION

AFIT/DS/AA/81-1

Harwood A. Hegna  
Captain USAF

DTIC  
ELECTED  
S JUL 1 1981 D  
D

Approved for public release; distribution unlimited

THE NUMERICAL SOLUTION OF INCOMPRESSIBLE  
TURBULENT FLOW OVER AIRFOILS

DISSERTATION

Presented to the Faculty of the School of Engineering  
of the Air Force Institute of Technology  
Air University  
in Partial Fulfillment of the  
Requirements for the Degree of  
Doctor of Philosophy

by

Harwood A. Hegna, B.A.E., M.S.A.E., M.S.M.E.  
Captain USAF

Approved for public release; distribution unlimited

THE NUMERICAL SOLUTION OF INCOMPRESSIBLE  
TURBULENT FLOW OVER AIRFOILS

by

Harwood A. Hegna, B.A.E., M.S.A.E., M.S.M.E.

Captain

USAF

Approved:

<u>Willie H. Halden</u>	<u>12 Feb 81</u>
Chairman	
<u>Stephen F. Knott</u>	<u>12 Feb 81</u>
<u>Harold E. Wright</u>	<u>12 Feb 81</u>
<u>John Jones Jr.</u>	<u>12 Feb 81</u>
<u>J. R. S. Shug</u>	<u>12 Feb 81</u>

Accepted:

J. P. Grossman, Ph.D. 12 Feb 81  
Dean, School of Engineering

#### ACKNOWLEDGMENTS

The beginning of a dissertation is like a walk of faith where the results are hoped for yet the means of acquiring those results not seen. The successful completion of such an endeavor causes me now to pause and reflect not only on the results which are described herein but also on the journey taken these past two plus years.

The opportunity afforded me by the United States Air Force to further my education while on active duty is appreciated. The motivation and technical support that I have received from my advisor, Dr. Wilbur Hankey, Jr., AFIT Adjunct Professor, are gratefully acknowledged. The professionalism displayed in the Computational Aerodynamics Group within the Flight Dynamics Laboratory, the sponsors of this research, has been a source of both technical and personal growth. I have also come to know those individuals as close friends. I have been blessed with my beloved wife, Helen, who joined me in marriage midway through this work and has given me her wholehearted loving support. Finally I thank my God who sustains me along my life's walk of which this journey has been a part.

HARWOOD A. HEGNA

February, 1981

## TABLE OF CONTENTS

	<u>Page</u>
ACKNOWLEDGMENTS . . . . .	iii
LIST OF FIGURES . . . . .	vi
LIST OF TABLES . . . . .	viii
NOTATION . . . . .	ix
ABSTRACT . . . . .	xix
I. INTRODUCTION . . . . .	1
II. BODY-FITTED CURVILINEAR COORDINATE SYSTEM	
A. Transformation . . . . .	15
B. Coordinate Line Attraction . . . . .	17
C. Body Surface Point Distribution . . . . .	20
III. GOVERNING EQUATIONS	
A. Basic Equations of Motion . . . . .	22
B. Boundary and Initial Conditions . . . . .	28
C. Turbulence Model . . . . .	29
D. Force Coefficients . . . . .	37
IV. NUMERICAL METHOD	
A. Grid Transformation . . . . .	41
B. Navier-Stokes Finite Difference Equations . . . . .	44
C. Boundary and Initial Conditions . . . . .	52
D. Turbulence Model . . . . .	56
E. Force Coefficients . . . . .	61
V. DISCUSSION OF RESULTS . . . . .	63

TABLE OF CONTENTS (Continued)

	<u>Page</u>
VI. CONCLUSIONS AND RECOMMENDATIONS. . . . .	83
BIBLIOGRAPHY . . . . .	86
APPENDICES	
A. Grid Transformation Relations. . . . .	114
B. Finite Difference Approximations . . . . .	117
C. Grid Modification for Wake Resolution. . . . .	119
D. Contour Integral Method for Determining Body Force Coefficients. . . . .	121
E. Time Increment Influence on SOR Convergence. . . . .	125
F. Far Field Boundary Conditions. . . . .	129
G. Inviscid Flow Results. . . . .	133
H. Experimental Data. . . . .	135

LIST OF FIGURES

<u>Figure</u>		<u>Page</u>
1	Physical and Transformed Planes . . . . .	93
2	Regions of Turbulent Flow. . . . .	94
3	Portion of 79x44 Body-Fitted Grid (First 30 Constant $\eta$ Lines). . . . .	94
4	Mean Flow Streamline Contours ( $\alpha = 5^\circ$ ) . . . . .	95
5	Mean Flow Streamline Contours ( $\alpha = 7.5^\circ$ ) . . . . .	95
6	Mean Flow Streamline Contours ( $\alpha = 9.5^\circ$ ) . . . . .	96
7	Mean Flow Streamline Contours ( $\alpha = 11.5^\circ$ ). . . . .	96
8	Mean Flow Velocity Field ( $\alpha = 5^\circ$ ). . . . .	97
9	Mean Flow Velocity Field ( $\alpha = 7.5^\circ$ ). . . . .	97
10	Mean Flow Velocity Field ( $\alpha = 9.5^\circ$ ). . . . .	98
11	Mean Flow Velocity Field ( $\alpha = 11.5^\circ$ ). . . . .	98
12	Mean Flow Pressure Contours ( $\alpha = 5^\circ$ ) . . . . .	99
13	Mean Flow Pressure Contours ( $\alpha = 7.5^\circ$ ) . . . . .	99
14	Mean Flow Pressure Contours ( $\alpha = 9.5^\circ$ ) . . . . .	100
15	Mean Flow Pressure Contours ( $\alpha = 11.5^\circ$ ). . . . .	100
16	Surface Mean Pressure Coefficients ( $\alpha = 5^\circ$ ). . . . .	101
17	Surface Mean Pressure Coefficients ( $\alpha = 7.5^\circ$ ). . . . .	101
18	Surface Mean Pressure Coefficients ( $\alpha = 9.5^\circ$ ). . . . .	102
19	Surface Mean Pressure Coefficients ( $\alpha = 11.5^\circ$ ). . . . .	102
20	Mean Flow Velocity Versus Surface Normal Distance Nondimensionalized by Computed Boundary Layer Thickness at Chord Locations on Upper Surface ( $\alpha = 5^\circ$ ). . . . .	103
21	Mean Flow Velocity Versus Surface Normal Distance Nondimensionalized by Computed Boundary Layer Thickness at Chord Locations on Upper Surface ( $\alpha = 7.5^\circ$ ). . . . .	103
22	Mean Flow Velocity Versus Surface Normal Distance Nondimensionalized by Computed Boundary Layer Thickness at Chord Locations on Upper Surface ( $\alpha = 9.5^\circ$ ). . . . .	104

LIST OF FIGURES (Cont'd)

<u>Figure</u>		<u>Page</u>
23	Mean Flow Velocity Versus Surface Normal Distance Nondimensionalized by Computed Boundary Layer Thickness at Chord Locations on Upper Surface ( $\alpha = 11.5^\circ$ )	104
24	Wake Mean Flow Velocity Profiles at Chord Locations with Origin on Chordline ( $\alpha = 5^\circ$ )	105
25	Wake Mean Flow Velocity Profiles at Chord Locations with Origin on Chordline ( $\alpha = 7.5^\circ$ )	105
26	Wake Mean Flow Velocity Profiles at Chord Locations with Origin on Chordline ( $\alpha = 9.5^\circ$ )	106
27	Wake Mean Flow Velocity Profiles at Chord Locations with Origin on Chordline ( $\alpha = 11.5^\circ$ )	106
28	Reynolds Stress $\overline{u'v'}$ Contours ( $\alpha = 5^\circ$ )	107
29	Reynolds Stress $\overline{u'v'}$ Contours ( $\alpha = 7.5^\circ$ )	107
30	Reynolds Stress $\overline{u'v'}$ Contours ( $\alpha = 9.5^\circ$ )	108
31	Reynolds Stress $\overline{u'v'}$ Contours ( $\alpha = 11.5^\circ$ )	108
32	Experimental Reynolds Stress $\overline{u'v'}$ Contours for NACA 4412 Airfoil ( $\alpha = 14^\circ$ and $Re = 1.5 \times 10^6$ ), Ref. 96	109
33	Surface Mean Pressure Coefficients Comparing Numerical Inviscid Methods with Experimental Data at $\alpha = 0^\circ$	109
34	Lift Coefficient Curve	110
35	Drag Polar Curve	110
36	Contour Integration Geometry for 2-D Flow	111
37	Maximum Error of SOR Solution for $U$ , $P$ , $P_b$ Versus Number of Iterations with $\Delta t = 0.0005$ ( $\alpha = 8^\circ$ )	112
38	Maximum Error of SOR Solution for $U$ , $P$ , $P_b$ Versus Number of Iterations with $\Delta t = 0.001$ ( $\alpha = 8^\circ$ )	112
39	Maximum Error of SOR Solution for $U$ , $P$ , $P_b$ Versus Number of Iterations with $\Delta t = 0.005$ ( $\alpha = 8^\circ$ )	113
40	Inviscid Flow Streamline Contours ( $\alpha = 11.5^\circ$ )	113

## LIST OF TABLES

<u>Table</u>	<u>Page</u>
I Computed Characteristics of Turbulence Near the Airfoil Leading Edge ( $X = -0.5$ ) . . . . .	68
II Computed Laminar Separation Bubble Characteristics . . . . .	68
III Computed Far Wake Characteristics. . . . .	72
C.I I Index ( $\xi$ Line) Designation for Grid Systems in Wake . . . . .	120
H.I Experimental Surface Pressure Coefficients for NACA 0012 Airfoil at Various Angles of Attack, $Re = 170,000$ . . . . .	136
H.II Experimental Velocity Field Measurements (Two Sets) Near Surface of NACA 0012 Airfoil. . . . .	137
H.III Experimental Velocity Field and Reynolds Stress Measurements in the Near Wake of NACA 0012 Airfoil. . . . .	141
H.IV Physical Coordinate Grid Locations for Experimental Data Measurements. . . . .	145

## NOTATION

### Symbols

$\epsilon$	Radius of cylinder in the far field boundary condition.
A	Coefficient matrix in Reynolds stress model; constant in inner eddy viscosity relaxation factor; cross-section area for two-dimensional contour integrals; and coefficient matrix for finite difference equations.
$A_k$	The kth amplification factor at a $\xi$ line in the coordinate attraction technique.
$A^+$	Laminar sublayer relaxation distance.
$A_1, A_2, A^3$	Constants occurring in the surface point distribution method.
ALFA	Modified grid transformation coefficient $\alpha/J^2$ .
b	Column matrix of "constants" in finite difference equations expression.
$\underline{b}$	Body force per unit mass.
B	Constant in the inner eddy viscosity relaxation factor; and coefficient of $p_{ij}$ denoting a combination of grid transformation quantities in Equation E.4.
BETA	Modified grid transformation coefficient $\beta/2J^2$ .
c	Airfoil chord.
$c_1, c_2$	The x and y components of unit outward normal vector from the body surface.
$c_b, c_f$	Contours which define the body surface and far field boundary.
$c_n$	Coefficients in Blasius' series.
$c_1, c_2$	Contours which define the cut in the physical plane.
$c_{fx}, c_{fy}$	The x and y components of the force coefficients.
$c_{MP}$	Counterclockwise moment coefficient about point $(x_p, y_p)$ .
D	Flow field dilatation or divergence.
$D_L$	Laminar sublayer damping factor.
$D_1, D_2$	Combinations of grid transformation quantities defined by Equations A.4 and A.5.

<u>Symbol</u>	
D( $\zeta$ )	Coordinate attraction damping factor.
E	Convergence error criteria.
f	Inner eddy viscosity relaxation factor; and maximum airfoil thickness as a fraction of the chord.
$\underline{f}$	Force per unit length of span exerted by the fluid on the airfoil.
f( $\zeta$ )	Blasius' series solution.
f( $\zeta, r$ )	General function in the computational plane.
F <sub>1</sub> , F <sub>2</sub>	The x and y components of a general vector function $\underline{F}(x, y, t)$ .
$\underline{F}$	Force exerted by the fluid on a body.
F(s)	Airfoil thickness function.
$\underline{F}(x, y, t)$	General vector function.
g( $\zeta, r$ )	General function in the computational plane.
G	An empirical constant in the model for the gradient diffusion term.
GAMA	Modified grid transformation coefficient $\gamma/J^2$ .
H <sub>12</sub>	Local shape factor $\beta^*/\gamma$ .
H( $\zeta, r_k$ )	Difference function used in the coordinate attraction method given by Equation 21.
i	Complex number.
$\hat{i}$	Unit vector in the x coordinate direction.
I	Numerical index for the ith $\zeta$ location.
IC1, IV1	Numerical upwind difference designators for i-1.
IC2, IV2	Numerical upwind difference designators for i-2.
IMAX	Numerical designator for the maximum number of $\zeta$ lines.
j	Unit vector in the y coordinate direction.
J	Jacobian of the grid transformation; and numerical index for the jth $\zeta$ location.

Symbol

JC1, JV1	Numerical upwind difference designators for j-1.
JC2, JV2	Numerical upwind difference designators for j-2.
JMAX	Numerical designator for the maximum number of $\xi$ lines.
k	Turbulent kinetic energy; and summation index.
$\hat{k}$	Unit vector in the direction perpendicular to the x-y plane.
$k_1, k_2, k_3$	Inner, outer, and far wake parameters in the turbulence eddy viscosity model.
$k_{1i}, k_{1f}$	The initial and final values for the parameter $k_1$ in the inner eddy viscosity relaxation factor.
K( $\xi$ )	Number of points specified in the boundary layer using the coordinate attraction method.
L	Turbulence length scale; and a characteristic length in the contour integral force calculation method.
$L_B$	Length of the calculated laminar separation bubble.
M	Pressure gradient parameter $-\frac{1}{2} Re \frac{du_e}{ds}$ .
n	Summation index; designates the nth time step; and a normal coordinate direction.
$\hat{n}$	Unit vector in the n coordinate direction; and a unit outward normal vector for a closed contour.
$n_1, n_2$	The x and y components of the unit outward normal vector of the body surface.
N	The sum of the laminar and turbulent viscosity coefficients in a rate equation approach to turbulence.
$N_Q$	Specified constant or function in a model for the turbulent gradient diffusion term.
p	Fluid static pressure variable.
$p^*$	Current value of the fluid static pressure obtained from the finite difference equation.
$P(\xi, \eta)$	Attraction function for $\xi$ lines.
q	Turbulence velocity scale defined by $(\overline{u'_i u'_i})^{1/2}$ .
Q	Coefficient of $u_{ij}$ denoting a combination of grid transformation quantities used in Equation E.2.

Symbol

$Q_k$	Velocity characteristic of large eddy motions in a model for the turbulent gradient diffusion term.
$Q(\xi, \eta)$	Attraction function for $\gamma$ lines.
$r$	Constructive grid parameter; and radius in the far field boundary condition model.
$\underline{r}$	Position vector relative to origin in the physical plane.
$R$	Region in the physical plane.
$\underline{R}$	Vector representation for the convective and viscous terms in the momentum equation.
$R(r)$	Radial stretching function in the constructive grid method.
$Re$	Freestream Reynolds number $U_\infty c/\nu$ .
$Re_t$	Turbulent Reynolds number defined by Equation 37.
$Re_s^*$	Reynolds number based on the local boundary layer displacement thickness and defined as $u_e^{2.5}/\nu$ .
$Re_\zeta$	Reynolds number based on the local boundary layer momentum thickness and defined as $u_e^{1.5}/\nu$ .
RHS	Time dependent and nonlinear terms in the Poisson pressure equation.
$s$	Arclength or surface tangent coordinate; and generalized airfoil chord direction variable.
$s_d$	Delay distance in the inner eddy viscosity relaxation factor.
$s_r$	Relaxation distance in the inner eddy viscosity relaxation factor.
$s_r$	General contour which encloses a two-dimensional body.
$s_n(\xi)$	Function which specifies the rate of change of arclength with $n$ at the body surface.
$s_b$	General body contour in the contour integral method.
sgn	Sign function.
$t$	Constructive grid parameter; time variable; and the maximum airfoil thickness.
$T$	Characteristic time period $c/U_\infty$ .
$\bar{T}$	Traction stress tensor.

Symbol

$u$	Variable which denotes the local $x$ component of flow field velocity.
$u^*$	Current value of the $u$ component of velocity obtained from the finite difference equation.
$\dot{u}$	Tangential field velocity component relative to the body surface tangential direction.
$U$	Column matrix representation of the variables at the grid point locations for the system of finite difference equations.
$U_\infty$	Magnitude of the freestream velocity.
$U_C$	Quantity which is proportional to the component of the local fluid velocity in the $\xi$ direction.
$UV$	Combination of grid transformation coefficients $-\zeta^2/2J^2$ .
$UX, UY$	The derivative of the local $u$ velocity with respect to $x$ and $y$ evaluated in the computational plane.
$v$	Variable which denotes the local $y$ component of the flow field velocity.
$v^*$	Current value of the $v$ velocity component obtained from the finite difference equation.
$\dot{v}$	Normal field velocity component relative to the surface normal direction.
$V$	Control volume.
$v_k, V_k$	The $k$ th velocity component in indicial notation.
$V_C$	Quantity which is proportional to the component of the local fluid velocity in the $\nu$ direction.
$VV$	Combination of grid transformation coefficients $-\zeta^2/2J^2$ .
$VX, VY$	The derivative of the local $v$ velocity component with respect to $x$ and $y$ evaluated in the computational plane.
$w_0$	Function which gives the maximum velocity defect in the wake at each location downstream.
$W$	Nondimensional complex valued velocity $u-iv$ .
$\tilde{W}$	Complex valued velocity $U_\infty$ ( $u-iv$ ).

<u>Symbol</u>	
$WL_1$	Non-interacting length in the near wake measured from the trailing edge of the airfoil.
$WL_2$	Turbulent interaction length in the near wake measured from the trailing edge of the airfoil.
$WL_{av}$	Average value of $WL_1$ and $WL_2$ .
$x$	Coordinate in the physical plane defining the airfoil chord axis; and a local tangential coordinate in the boundary layer turbulence model.
$x_k$	The kth coordinate in indicial notation.
$x_L$	Turbulent transition length measured along the body surface.
$x_p$	The x coordinate of a location in the physical plane about which a moment is computed; and a new x coordinate location obtained by the interpolation of adjacent grid lines.
$x_R$	The x coordinate which locates the position of the shear layer reattachment which forms the bubble in the numerical solution.
$x_t$	The x coordinate which locates the start of transition to turbulence on the upper airfoil surface in the numerical solution.
$x_T$	The x coordinate which locates where fully turbulent flow first occurs downstream of the leading edge on the upper airfoil surface in the numerical solution.
XETA	Modified grid transformation metric $x_r/2J$ .
XXI	Modified grid transformation metric $x_z/2J$ .
y	Coordinate in the physical plane normal to the airfoil chord; a local normal coordinate in the boundary layer turbulence model.
$y_k$	Computed location of the kth point within the boundary layer for equal velocity increments in the coordinate attraction method.
$y_p$	The y coordinate of a location in the physical plane about which a moment is computed; a new y coordinate location obtained by the interpolation of adjacent grid lines.
$y_t(x)$	Airfoil thickness function for NACA four digit airfoil sections.

Symbol

YETA	Modified grid transformation metric $y_r/2J$ .
YXI	Modified grid transformation metric $y_r/2J$ .
z	Input axis variable for calculating x coordinates of the final distributed surface points.
Z	Nondimensional complex variable $x+iy$ in the far field boundary condition model.
$\tilde{Z}$	Complex variable $c(x+iy)$ in the far field boundary condition model.
$\alpha$	Geometric angle of attack; and a grid transformation coefficient $x_n^2 + y_n^2$ .
$\alpha_L$	Geometric angle of attack.
$\alpha_1$	The value $f''(0)$ in the Blasius' series.
$\xi$	Grid transformation coefficient $x_{\xi_r} + y_{\xi_r}$ .
$\gamma$	Grid transformation coefficient $x_r^2 + y_r^2$ ; and the intermittency factor defined in Equation 63.
$\Gamma$	Clockwise circulation around a body.
$\Gamma(x)$	Turbulent transition factor function.
$\delta$	Local boundary layer thickness.
$\delta_w$	Local wake half width.
$\delta^*$	Local displacement thickness defined by Equation 64.
$\delta_{ji}$	Kronecker Delta.
$\Delta y$	Input displacement in last two y positions at the outer boundary in the coordinate line attraction method.
$\varepsilon$	Dissipation rate of turbulent energy.
$\varepsilon_i$	Inner layer eddy viscosity.
$\varepsilon_M$	Turbulent eddy viscosity.
$\varepsilon_o$	Outer layer eddy viscosity.
$\varepsilon_w$	Wake value of the eddy viscosity.
$\varepsilon_{ic}$	Inner layer eddy viscosity for comparison in limiting technique.
$\varepsilon_{ow}$	Far wake eddy viscosity value.

Symbol

$\eta$  Coordinate in the computational plane which is used to define the body surface.

$n_k$  Summation parameter defined as  $(k-1)^\frac{1}{2}$ .

$n_p$  A selected contour integral path around the body.

$\zeta$  Local momentum thickness; and the angular coordinate in complex polar variables.

$\psi(\theta)$  Function which specifies the angle that the incoming  $\zeta$  lines make with the body surface coordinate.

$\lambda$  Transition distance defined as the distance required to vary  $\zeta(x)$  from  $1/4$  to  $3/4$ .

$\zeta_R$  Turbulent reattachment criteria defined as  $(\zeta/\zeta_e) du_e/ds$ .

$\nu$  Dynamic viscosity coefficient.

$\mu_D$  Potential doublet strength.

$\nu$  Kinematic viscosity  $\nu = \mu/\rho$ .

$\xi$  Coordinate in the computational plane which emanates from the body surface grid points and is orthogonal to  $\eta$  in the computational plane.

$\pi$  Ratio of circumference to diameter of a circle.

$\rho$  Fluid density.

$\sigma$  Similarity parameter in Blasius' series of Equation 16; and a grid transformation coefficient defined by Equation A. 7.

$\sigma_B, \sigma_I$  Inner and outer control volume surfaces.

$\tau$  Grid transformation coefficient defined by Equation A.8.

$\tau_{ij}$  Element of the viscous stress tensor.

$\tau_{tij}$  Element of the turbulent stress tensor.

$\tau_{Tij}$  Element of the total stress tensor,  $\tau_{ij} + \tau_{tij}$ .

$\psi_d$  Transonic small disturbance potential doublet function.

$\psi_v$  Transonic small disturbance potential vortex function.

$\gamma$  Acceleration parameter for pressure iteration given by Equation 40 defined as  $2 \cdot J^2 / ((1 + \gamma)t)$ .

$\psi$  Inviscid stream function.

### Symbol

$\omega$  Magnitude of the local flow field vorticity,  $\text{curl } \underline{v}$ ; and a local acceleration parameter.

$\omega_p$  Acceleration parameter for the field pressure finite difference equations.

$\omega_{pb}$  Acceleration parameter for the surface pressure iteration.

$\omega_{uv}$  Acceleration parameter for the u and v velocity component finite difference equations.

### Subscript

b Denotes a location on the body surface.

e Denotes a location at the edge of the boundary layer or wake.

f Denotes a location on the computational far field boundary.

i Denotes the  $\xi$  coordinate location in the computational plane for finite difference equations; and an indicial notation index in differential equations.

j Denotes the  $r$  coordinate location in the computational plane for finite difference equations; and an indicial notation index in differential equations.

k A component index in indicial notation.

max,min Denote the maximum and minimum values of a variable.

s Denotes a value at the laminar separation point which defines the beginning of the bubble.

w Denotes a value in the wake region.

x,xx Denote differentiation with respect to x.

y,yy Denote differentiation with respect to y.

t,t Denote differentiation with respect to t.

$\xi,\xi$  Denote differentiation with respect to  $\xi$ .

$\underline{\quad}$  Denotes a vector quantity.

### Superscript

\* Denotes a quantity in the transformed plane.

$\overline{\quad}$  Denotes a turbulence time averaged quantity.

Superscript

- ' Denotes a turbulent fluctuating quantity.
- ~ Denotes a temporary nondimensional variable definition.
- s Iteration number in the successive-over-relaxation iteration procedure.
- n Pertaining to n contours.
- ξ Pertaining to ξ contours.

Prefix

- d Derivative operator.
- D Substantial derivative operator ( $D-/Dt = \partial-/Dt + v^* \underline{\partial}/\underline{x}$ ).
- Δ Increment.
- Σ Summation.
- ∇ Del-operator defined as  $\hat{i} \frac{\partial}{\partial x} + \hat{j} \frac{\partial}{\partial y}$ .
- ∂ Partial derivative operator.

ABSTRACT

Numerical solutions are obtained for two-dimensional incompressible turbulent viscous flow over airfoils of arbitrary geometry. An algebraic eddy viscosity turbulence model based on Prandtl's mixing length theory is modified for separated adverse pressure gradient flows. Finite difference methods for solving the inviscid stream function equation and the incompressible laminar Navier-Stokes equations are used. A finite difference method for solving the Reynolds averaged incompressible turbulent two-dimensional Navier-Stokes equations is employed.

The inviscid stream function equation and the Navier-Stokes equations are transformed using a curvilinear transformation. A body-fitted coordinate system with a constant coordinate line defining the airfoil section surface is transformed to a rectangular coordinate system in the transformed or computational plane. An elliptic partial differential Poisson equation for each coordinate is used to generate the coordinate system in the physical plane for arbitrary airfoils.

The two-dimensional time dependent Reynolds averaged incompressible Navier-Stokes equations in the primitive variables of velocity and pressure and a Poisson pressure equation are numerically solved. Turbulence is modelled with an adverse pressure gradient eddy viscosity technique. An implicit finite difference method is used to solve the set of transformed partial differential equations. The system of linearized simultaneous difference equations, at each time step, is solved using successive-over-relaxation iteration. Far field boundary conditions are

examined. Solutions for a NACA 0012 airfoil at angles of attack varying from five to 11.5 degrees at a chord Reynolds number of 170,000 are obtained. Velocity profiles near the airfoil surface and surface pressure distributions are presented and compared with experimental data. Lift and drag coefficients agree well with experimental values. The computed lift coefficients near stall are within 5% of the experimental measurements, and the numerical drag coefficients agree within ten drag counts in the region of maximum lift to drag ratio. The short laminar separation bubble near the suction pressure peak is numerically determined. The variation of bubble length and turbulent transition length with angle of attack are similar to experimental trends.

## SECTION I

### INTRODUCTION

Much effort has been expended by the aeronautical community in determining the aerodynamic characteristics of airfoils. Linear methods are extensively used in design work for studying configurations at small angles of attack with negligible flow separation. Experimental wind tunnel investigations are used to determine the characteristics near stall where separation phenomena become important. Recent developments in numerical techniques have stimulated research on another approach, namely the numerical solution of the Navier-Stokes equations. These equations model the viscous effects which contribute to airfoil stall. For this reason, numerical Navier-Stokes methods offer the possibility of determining the aerodynamic characteristics for airfoils experiencing stall. Numerical methods can also complement experimental methods by efficiently extending the range of parameters under investigation. Furthermore, numerical methods eliminate model support interference and wall interference effects found in wind tunnel testing.

The purpose of this investigation is to develop a numerical Navier-Stokes method that will accurately determine the aerodynamic characteristics of incompressible turbulent viscous flow over two-dimensional airfoils near stall.

The development of a numerical method for turbulent flow requires a suitable technique for distributing points throughout the flow field and a model which describes the behavior of turbulence within specific regions of the flow field. A survey of numerical grid generating techniques and available turbulence models is presented. The quantity of literature concerned with the Navier-Stokes equations is extensive. Therefore, a

summary of the literature, which describes formulations of the Navier-Stokes equations and their numerical solving techniques applied to flows over airfoils, is given. The research objectives for this work are then discussed, and a summary of the remaining sections is presented.

Body-fitted curvilinear coordinate systems greatly enhance the application of numerical methods to practical boundary value problems involving partial differential equations. The representation of a boundary surface as a coordinate line reduces the difficulties associated with numerically specifying boundary conditions by interpolation in finite differences methods. In the physical  $(x,y)$  plane, values for one computational coordinate  $\xi$  are specified at selected points on both the body surface and the outer boundary. Constant values for the other computational coordinate  $\nu$  are specified on both the body surface and the outer flow boundary. The transformed computational  $(\xi, \nu)$  plane then becomes a rectangular region with an orthogonal grid. Winslow (1) and Chu (2) introduced the concept for two-dimensional regions interior to a closed boundary. Their transformed coordinates are solutions of Laplace's equation in the physical plane and define a triangular mesh system in the physical plane. Amsden and Hirt (3) took the physical coordinates to be solutions of a modified Laplace's equation in the transformed plane.

Thompson, Thames, and Mastin (4,5,6) generalized the method for the automatic generation of body-fitted coordinates for any two-dimensional, multi-connected region. They also introduced the use of forcing functions in a Poisson equation which provides mesh control in regions with large gradients. Hodge (7) developed an automated grid line attraction method based on boundary layer theory which determines the coefficients in his

forcing function. Hodge assumed a Blasius boundary layer profile and distributed his grid points at approximately equal velocity increments in the boundary layer. Steger and Sorenson (8) introduced auxiliary conditions for the forcing functions which provide angle and distance control at the inner boundary surface. The angle with which a  $\xi$  line intersects the body surface is specified by a function  $(\xi)$ , and the rate of change of arclength with  $\xi$  on a  $\xi$  line at the body surface is prescribed by  $s_\xi(\xi)$ . Sorenson (9) later imposed similar conditions on an outer computational boundary. These auxiliary conditions are used to solve for coefficients in the chosen exponential forcing functions. The geometric conditions hold exactly only in the limit as  $\xi$  approaches zero. Sorenson reported that numerical instabilities occur for large changes in the coefficients during successive iterations and for boundaries with sharp corners. He implemented a limit function which damped the change of the value for each coefficient over one iteration; and at sharp corners he computed average values of each coefficient from data at the neighboring boundary points. Mastin and Thompson (10) have also extended the elliptic body-fitted coordinate generation technique to three dimensions for simple geometries.

Some other specific grid generation techniques which use properties of elliptic differential equations have also been reported. Meyder (11) constructed an orthogonal curvilinear coordinate system by using electric field theory. He solved the potential equation twice with different sets of mixed Dirichlet and Neumann boundary conditions for the electric potential and electric force lines, respectively. These solutions, however, were obtained in the physical plane using interpolation and became the curvilinear coordinate lines in the physical plane. The coordinate metrics were then used to formulate a finite difference equation which was also solved in the

physical plane. Conformal mapping techniques which employ the Theodorsen-Garick (12) transformation have been examined by Ives (13). He introduced the use of fast Fourier transform methods and developed a new class of transformations which maps the flow field of a two-element airfoil onto the region between two concentric circles. Conformal techniques are not capable of being extended to three-dimensional geometries (4). Neither of these approaches offers a convenient means for mesh control in regions of large flow gradients.

Recently, a geometric grid generation technique has been introduced by Gibeling, Shamroth, and Eiseman (14). The technique parameterizes ( $t$ ) the body and outer boundary surfaces and uses a stretching function  $R(r)$  for mesh attraction along constructed lines perpendicular to the body surface. Unit increments for ordered pairs  $(t,r)$  generate the corresponding computational plane. Further refinements which provide angle and arclength variation control at a body surface have subsequently been developed by Eiseman (15,16,17).

The search for an accurate and universal turbulence model has paralleled the development of body-fitted grid generation techniques. In principle, the Navier-Stokes equations completely describe the turbulent fluctuating fluid motion. The required mesh resolution, necessary to resolve the turbulent eddies with varying length scales, when translated into computer resources presently make this approach unfeasible. Many quantities of engineering interest in turbulent flows involve a mean value taken over a time interval. The time interval is sufficiently long to include many fluctuations while small compared with the characteristic time of the mean flow. The Navier-Stokes equations can then be re-formulated using these mean flow variables. This Reynolds averaging procedure introduces the mean of terms

involving fluctuating quantities. The Reynolds stress components  $\overline{u_i' u_j'}$  are the most common terms of this type. In order to solve the averaged form of the Navier-Stokes equations, "turbulence closure" must be achieved by suitably modelling these additional terms. This approach to turbulence has led to models which introduce auxiliary relationships ranging from algebraic equations to several partial differential equations. These models are commonly categorized and are now summarized according to the number of additional partial differential equations which comprise the model.

The algebraic or zero equation models have their origins in Boussinesq's (18) eddy viscosity hypothesis and Prandtl's (19) mixing length model. The local turbulent stresses are assumed proportional to the local mean flow strain rates with the proportionality constant defined as an equivalent or eddy viscosity. The eddy viscosity models of Cebeci-Smith (20), Mellor-Herring (21), and Patankar-Spalding (22) represent this approach. The boundary layer in each method is divided into an inner near wall layer and an outer wake layer with separate expressions for the eddy viscosity coefficient. In the Cebeci-Smith and Patanker-Spalding models the inner mixing length varies as a linear function of the normal distance from the wall modified with a Van Driest (23) laminar sublayer correction. The Cebeci and Mellor models both base the outer length scale on the displacement thickness while the Patanker-Spalding model uses the boundary layer thickness directly. These models have been successfully extended and applied (24) to a wide variety of boundary layer flow geometries involving compressibility, heat and mass transfer, and curvature effects. In addition, the mean flow models are computationally efficient. Launder and Spalding (25) point out, however, that these models predict a vanishing eddy viscosity where the velocity gradient is zero and have not been successful for large separated recirculating flows.

The one equation turbulence model introduced by Prandtl (26) is an extension of the algebraic technique. In this approach the solution of the partial differential turbulent kinetic energy equation usually provides a local velocity scale given by  $q^2 = \overline{u'_i u'_i}$  where summation is implied. The length scale L is prescribed by an algebraic expression as before. Terms involving fluctuating quantities other than q must still be modelled. Glushko (27), Mellor and Herring (28), and Wolfshtein (29) model the gradient diffusion term  $-(\overline{(u'_k p_{ij})} + \overline{u'_k (u'_i u'_i)})/2$  with a gradient of  $q^2$  given as  $N_Q \epsilon_M S_k (q^2/2)$  where  $N_Q$  is a specified constant or function and  $\epsilon_M$  is the eddy viscosity. The Reynolds stress is related to the mean flow as in the algebraic approach except that the eddy viscosity is assumed proportional to  $qL$ . Bradshaw, et al (30) model the gradient diffusion term with an expression  $G q^2 Q_k$  where G is an empirical constant or function and  $Q_k$  is a velocity characteristic of large eddy motions. They also write the Reynolds stress directly as a function of q in the form  $\tau_{tij} = A_{ij} q^2$ . In each model the isotropic dissipation is modelled by a form  $q^2/L$ . Nee and Kovasznay (31) use a rate equation for the total viscosity  $N = L + \epsilon_M$  in place of the kinetic energy equation. They formulated expressions for the generation and dissipation terms involving various constants and the length scale. Launder and Spalding (25) observe that the one differential equation models require a moderate increase in computer resources but do not in general provide more accurate results than the results obtained from algebraic methods.

Kolmogorov (32) introduced the somewhat more complex type of turbulence model which uses two partial differential equations. A form of the turbulent kinetic energy equation provides a local velocity scale. The local length scale is obtained from a second equation. Ng and Spalding (33) formalized

this approach by introducing the energy-length equation derived by Rotta (34). They also used the Glushko closure model in the turbulent energy equation. This class of two equation models is named the  $k - kL$  turbulence model where the eddy viscosity is proportional to  $k^2 L$ . Saffman (35) has used a transport equation for the mean vorticity . together with the turbulent kinetic energy. The eddy viscosity becomes proportional to  $k/\omega$  in this  $k - \omega$  class of closure models for turbulence. The local length scale is assumed to be proportional to  $k^{1/2}/\omega$ . Wilcox and Rubesin (36) have modified this approach for compressible flows and generalized the constitutive equation. Jones and Launder (37) use a transport equation for the rate of dissipation of turbulent energy  $\varepsilon$  along with the turbulent kinetic energy equation. Glushko type closure models are assumed for the terms involving fluctuating quantities in both equations. This  $k - \varepsilon$  class of two equation models has a local length scale proportional to  $k^{3/2}/\varepsilon$  with the eddy viscosity proportional to  $k^{1/2}/\varepsilon$ . The two equation models have been applied to various boundary layer and free shear layer flows with a variety of constants and closure models. The two equation models require significant increases in computational resources and have not led to a model of universal applicability (24,25).

The search for a more general turbulence model has led to the use of the transport equations for the Reynolds stresses. In this approach the eddy viscosity concept is discarded. Closure models, however, are still required for the terms containing fluctuating quantities other than the Reynolds stresses. Donaldson (38) introduce closure models which express the fluctuating terms as functions of the Reynolds stress and chosen length scales. Hanjalic and Launder (39) introduce closure models which use the Reynolds stress and retain the equations for turbulent kinetic energy

$k$  and turbulent dissipation  $\epsilon$ . Only cases with the simplified two-dimensional boundary layer approximations have been investigated. The extensive computational resources and initial state of development of these models preclude this type of approach from practical consideration as a turbulence model for a complex flow field computation.

Theoretical turbulence models of further complexity have appeared. Kolovandin and Votutin (40) introduced a statistical theory where additional equations are obtained for other correlations of the fluctuating quantities. Ferziger (41) took a meteorological viewpoint of turbulent flows by numerically simulating large scale eddies while modeling the small scale structures with an eddy viscosity technique. This approach is a first step toward numerically solving a turbulent flow field with the instantaneous equations of motion.

The review of available turbulence models provides the basis for selecting a suitable approach for use in the numerical solution. The algebraic and the two equation eddy viscosity models appear to be realistic choices. As previously reported (25), the one equation techniques yield unimproved results compared with algebraic methods and at additional cost in computer resources. The two equation methods require the solution of additional partial differential equations. In these methods, terms involving fluctuating quantities, except the Reynolds stresses, must still be modelled using additional coefficients. For these reasons, the simpler algebraic eddy viscosity technique, which requires considerably less computer resources, is employed. If the physical phenomena associated with separated adverse pressure gradient flows can be included in the turbulence model, then the accurate calculation of the aerodynamic characteristics may be accomplished with an algebraic technique.

A survey of the previous research involving numerical solutions of the Navier-Stokes equations for flow over airfoils establishes the pre-

diction level of computational methods and also reviews the numerical algorithms. The grid generation technique and turbulence model employed, when applicable, are also included.

Early numerical solutions of the Navier-Stokes equations for flow over airfoils used the vorticity-stream function formulation with an automated grid generation technique (4). Walker (42) applied the method to the laminar flow over a flat plate and compared the numerical solution with Blasius' (43) solution. Thames (44) used body-fitted coordinates with the vorticity-stream function approach and solved the Navier-Stokes equations for various bodies in doubly connected regions. He obtained solutions for the flow over airfoils at chord Reynolds numbers less than  $10^4$ . Problems mainly attributed to wall vorticity developed for solutions of airfoils at angle of attack.

Mehta and Lavan (45) also used a vorticity-stream function method in studying the laminar starting vortex and separation bubbles for impulsively started incompressible laminar flow over a Joukowski airfoil at Reynolds numbers less than  $10^4$ . They used three point backward time differences and centered spatial differences. The computational grid was obtained through a conformal transformation followed by a radial stretching transformation.

Reddy and Thompson (46) applied an integro-differential, vorticity-velocity field method for the solution of incompressible flow in doubly connected regions. Backward time, centered spatial (BTCS) differences were applied to the Navier-Stokes equations. The difference equations were solved using successive-over-relaxation (SOR) iteration. They also employed the coordinate mesh attraction technique with a time dependent expanding mesh system. Symmetric airfoils at zero angle of attack with a Reynolds number less than  $10^6$  were considered. At the higher Reynolds numbers, the calculation of surface vorticity required a large num-

ber of grid points on the surface which greatly increased the required computer time. A steady state solution was not obtained.

The vorticity-velocity field formulation has been applied by Sankar and Wu (47) to the case of incompressible laminar flow about an oscillating airfoil. They used a 12% thick Joukowski airfoil at a Reynolds number of 1000. Triangular finite elements were constructed near the airfoil surface and a rectangular mesh was used away from the airfoil. A conformal transformation was used to map the airfoil in the physical plane onto a unit circle in the computational plane. Sankar and Tassa (48) investigated this same problem with a compressible flow formulation of the Navier-Stokes equations. They used a conformal transformation followed by an algebraic radial stretching transformation. The alternating-direction-implicit (ADI) finite difference method of Briley and McDonald (49) was used to obtain solutions for Reynolds numbers less than  $10^4$  and a Mach number of 0.2. In a separate research effort, Sugavanam and Wu (50) attempted to use a two equation k- turbulence model with a vorticity-velocity formulation. A conformal transformation for a 12 percent thick Joukowski airfoil was used. They experienced difficulties in obtaining a converged solution even after eight hours of CYBER 74 CPU time were expended. Variations for both lift and drag of the order of 50 percent occurred.

The use of the primitive variables of velocity and pressure for incompressible flow was introduced by Harlow and Welch (51) in the explicit forward time, centered spatial (FTCS) March-and-Cell (MAC) method. They included a Poisson equation for pressure which is obtained by taking the divergence of the momentum equation. They also found that the velocity divergence terms in the momentum equations were required for the pressure field calculation. Hirt and Harlow (52) further developed the method. Hodge (53) considered the case of laminar incompressible viscous flow for an airfoil at angle of attack. He used a form of the Thompson, et al (4)

body-fitted grid transformation and applied an implicit BTCS differencing method to the Navier-Stokes equations. The system of difference equations was solved with SOR iteration. Various methods of calculating the pressure field were investigated. Hodge concluded that the momentum equations should retain the velocity divergence terms and that a Poisson pressure equation should be used to satisfy continuity. Ghia, Hankey, and Hodge (54) applied a Poisson pressure equation and the primitive variables form of the Navier-Stokes equations to study incompressible driven flow in a square cavity for Reynolds numbers under 1000. They used an alternating-direction-implicit (ADI) finite difference technique for the momentum equations and SOR iteration for the pressure equation. A Neumann boundary condition derived from the normal component of the momentum equations was employed to compute the wall pressure.

The Poisson pressure equation has been further examined by Chien (55) for internal flows. He observed that the calculation of pressure by direct integration of the momentum equations can be inaccurate when large velocity variations are present. He found that forms of the pressure equation were more suitable for computing the pressure field near boundaries. Recently, Hodge, et al (7) applied an implicit backward time finite difference method with both upwind and centered spatial differences to the Navier-Stokes equations in primitive variables form. A Poisson pressure equation was used to obtain a solution for laminar flow over airfoils at angle of attack with a Reynolds number of order  $10^5$ . The solution contains a large oscillating separated region which gives approximate trends in lift but very poor agreement with available drag data (56).

Early numerical Navier-Stokes investigations of turbulent flow over airfoils considered two-dimensional transonic viscous flow at small angles

of attack. Deiwert (57) applied MacCormack's explicit method (58) with a 50x38 rectangular based exponentially stretched mesh. He used 20 uniformly spaced points to define the upper airfoil surface and imposed the Neumann boundary layer condition  $\delta p/\delta n = 0$  on the surface. Steger (59) used the implicit Beam-Warming method (60) with a 71x33 grid obtained from a modified Thompson transformation (4). He calculated the solution on the branch cut with a linear extrapolation procedure and evaluated surface pressures using the momentum equations for the direction normal to the surface. Walitt, et al (61) applied the first order method of Trulio (62) coupled with a boundary layer technique used near the airfoil leading edge. They used a 130x68 mesh system but did not capture the full suction pressure on the upper surface near the airfoil nose. Each investigation used a Cebeci-Smith (63) type algebraic eddy viscosity model and the Reynolds averaged compressible Navier-Stokes equations.

Recently, Shamroth and Gibeling (64) used the Briley-McDonald (49) implicit finite difference formulation with a constructive type 81x30 grid system to compute turbulent flow over an airfoil at an angle of attack of 6 degrees and Reynolds number of  $10^6$ . They first tried a two equation  $k-\epsilon$  turbulence model but experienced convergence problems near the leading edge and far field flow regions. They reported obtaining large or negative values for the turbulent viscosity in essentially laminar regions. The turbulent kinetic energy equation with an algebraically prescribed length scale was then used. Major discrepancies occurred for the mean pressure distribution solution in the suction peak and trailing edge regions of the airfoil surface. They also noted that the constructive grid technique caused a crossing of grid lines of the same family for highly cambered airfoils.

The examination of existing numerical solutions of the Navier-Stokes

equations for two-dimensional flow over airfoils reveals Reynolds number and angle of attack restrictions. As a result, numerical Navier-Stokes methods for the accurate computation of the flow field and resulting aerodynamic characteristics for an airfoil near stall are unavailable. The development of such a numerical method for solving incompressible two-dimensional turbulent flow over airfoil sections near stall does, therefore, constitute a significant contribution in computational aerodynamics. The fulfillment of this research goal requires the formulation of an adequate turbulence model for use in both leading and trailing edge separated regions. The far field boundary conditions for incompressible flows must also be examined.

The selection of a suitable numerical approach for incompressible turbulent flows is based on several considerations. An implicit technique is preferred because of the required small grid spacing near the body surface necessary to resolve viscous stresses. Stability criteria of explicit methods would impose a small time step restriction as a result of the grid size. The numerical method should be capable of predicting laminar flow for Reynolds numbers approaching turbulent flow conditions since regions of laminar flow may occur. The use of primitive variables is readily extended to three dimensions and provides for the direct calculation of the pressure field. These criteria are satisfied by an implicit finite difference procedure developed by Hodge (53,7) which uses primitive variables and successive over-relaxation iteration. The implicit finite difference method is employed in this investigation.

The remaining sections of this research effort discuss the technique employed in achieving the defined research goal. In Section II a form of the Thompson numerically generated body-fitted coordinate system is described. The methods of attracting grid lines to the body surface and distributing

surface points are also discussed. The governing equations for incompressible two-dimensional turbulent flow in primitive variables are presented in Section III. Boundary and initial conditions are discussed. An algebraic eddy viscosity turbulence model formulated for adverse pressure gradient separated flows is described. An algebraic type of turbulence model has been chosen because of the previous computational successes for other turbulent flow problems and the definite computational efficiency obtained by this approach. The method for evaluating force coefficients exerted on the body by the flow field is then discussed. The numerical techniques used in obtaining a solution are presented in Section IV. First, the finite difference method for numerically generating the grid is given. The Navier-Stokes equations are then written in finite difference form. The numerical method used to implement the boundary and initial conditions is described. The computational procedure for introducing turbulence is next discussed. The finite difference and numerical integration techniques for calculating the force coefficients are then presented. The formal discussion of the numerical solutions and comparisons with experimental data are given in Section V. The conclusions derived from this research work and recommendations for future work are set forth in Section VI.

## SECTION II

### BODY-FITTED CURVILINEAR COORDINATE SYSTEM

In this section the technique is described which numerically generates body-fitted curvilinear coordinate systems as previously developed by Thompson, Thames, and Mastin (4,5). Coordinate lines are attracted to the body surface with a method introduced by Hodge (7). The distribution of grid points which define the body surface is discussed.

#### A. Transformation

The doubly-connected, two-dimensional region  $\Omega$  bounded by closed contours  $\Gamma_b$  and  $\Gamma_t$  of arbitrary shape is to be transformed into a rectangular domain  $\tilde{\Omega}^*$  as shown in Figure 1. The general transformation from the physical  $(x, y)$  plane to the transformed or computational  $(\xi, \eta)$  plane is given by

$$\xi = \xi(x, y) \quad \eta = \eta(x, y) \quad (1)$$

The inverse transformation, if it exists, can be expressed as

$$x = x(\xi, \eta) \quad y = y(\xi, \eta) \quad (2)$$

The related Jacobian is given as

$$J = x_{\xi} y_{\eta} - x_{\eta} y_{\xi} \quad (3)$$

where the subscripts denote differentiation.

The existence of the inverse transformation has been studied by Thames (6). He showed that if the functions of Equation 1 are continuous, differentiable at a point, and the Jacobian is non-singular, then the general transformation has an inverse in a disk about the point. In addition, if the  $\xi$  and  $\eta$  transformation functions are harmonic, then a weak maximum principle is obeyed. Then, no extrema will exist in regions  $\Omega$  and  $\tilde{\Omega}^*$  except the function  $J$  will not be zero there.

Partial derivatives are transformed using the chain rule and inverse transformation relations. For a sufficiently differentiable function  $f$  of  $x$  and  $y$ , the derivatives transform as follows:

$$f_x = (y_\eta f_\xi + y_\zeta f_\tau)/J \quad (4)$$

$$f_y = (-x_\eta f_\xi + x_\zeta f_\tau)/J \quad (5)$$

Higher order derivatives are similarly derived.

The system of elliptic coordinate generating equations is chosen to be

$$\xi_{xx} + \xi_{yy} = P(\xi, \tau) \quad (6a)$$

$$\tau_{xx} + \tau_{yy} = Q(\xi, \tau) \quad (6b)$$

with the boundary conditions on curve  $C_b$

$$\xi = \xi_b(x, y) \quad \tau = \tau_b \quad (7)$$

and on curve  $C_f$

$$\xi = \xi_f(x, y) \quad \tau = \tau_f \quad (8)$$

where  $\xi_b(x, y)$  and  $\xi_f(x, y)$  are prescribed functions and  $\tau_b$  and  $\tau_f$  are prescribed constants. The other two sides  $C_1^*$  and  $C_2^*$  in the rectangular region are transformed from the branch cut  $C_1 - C_2$ . The functions  $x(\xi, \tau)$  and  $y(\xi, \tau)$  and all derivatives are continuous across this cut. These boundary conditions insure that the body and the far field boundaries are defined by constant  $\tau$  lines. The generalized functions  $P$  and  $Q$  are utilized in attracting the coordinate lines in various regions.

The rectangular grid system in the transformed plane is used for the computations. The mesh generating system, Equations 6a and 6b, is transformed to the computational plane and becomes

$$\alpha x_{ij} + 2\beta x_{ji} + \gamma x_{ii} = -J^2 [x_j P(\xi, \eta) + x_i Q(\xi, \eta)] \quad (6a)$$

$$\alpha y_{ij} + 2\beta y_{ji} + \gamma y_{ii} = -J^2 [y_j P(\xi, \eta) + y_i Q(\xi, \eta)] \quad (6b)$$

where

$$\alpha = x_i^2 + y_i^2 \quad (10)$$

$$\beta = x_j^2 + y_j^2 \quad (11)$$

$$\gamma = x_i x_j + y_i y_j \quad (12)$$

The boundary conditions, Equations 7 and 8, similarly become on curve  $C_b^*$ ,

$$x = f_b(\xi, \eta_b) \quad y = g_b(\xi, \eta_b) \quad (13)$$

and on curve  $C_f^*$

$$x = f_f(\xi, \eta_f) \quad y = g_f(\xi, \eta_f) \quad (14)$$

The functions  $f_b$ ,  $f_f$ ,  $g_b$ , and  $g_f$  are determined by the known contours  $C_b$  and  $C_f$  and the functions  $\xi_b$  and  $\xi_f$ .

### B. Coordinate Line Attraction

The resolution of viscous terms near the body surface requires a fine mesh spacing in this region. The forcing functions  $P$  and  $Q$  are used to attract  $\xi$  and  $\eta$  lines, respectively. In this work the  $\xi$  line spacing is accomplished by specifying the boundary condition function  $\xi_b(x, y)$ . The  $\eta$  line spacing is adjusted through the use of the  $Q$  function proposed by Thompson (4) and modified by Hodge (7)

$$Q(\xi, \eta) = -\sum_{k=1}^{K(\xi)} A_k(\xi) \exp[-D(\xi) \cdot -\eta_k] \quad (15)$$

where  $A_k$  are the amplification factors,  $D$  is the damping factor,  $K$  is the number of terms, and  $\eta_k = (k - 1)\eta$ . The amplification and damping factors are determined by requiring that the tangential velocity  $u$  be a linear

function of  $\zeta$ . In this case, the second and higher order derivatives with respect to  $\zeta$  become zero thereby minimizing the truncation error of  $u$  in the transformed plane.

Hedge (7) has developed a technique which approximately satisfies the above criterion. The required point distribution on a  $\zeta$  line is determined using Blasius' flat plate boundary layer solution. The similarity series solution (43) is given by

$$f(\zeta) = \sum_{n=0}^{\infty} (-1)^n \frac{C_{n+1}}{(3n+2)!} \zeta^{3n+2} \quad (16)$$

where the similarity variable  $\zeta = y[u_e/x]^{\frac{1}{2}}$ .  $u_e$  is the edge boundary layer velocity and  $\nu$  is the kinematic viscosity. Differentiating Equation 16 with respect to  $\zeta$  gives an expression for the tangential velocity  $u$  in the boundary layer

$$f'(\zeta) = \frac{u}{u_e} = \sum_{n=0}^{\infty} (-1)^n \frac{C_{n+1}}{(3n+1)!} \zeta^{3n+1} \quad (17)$$

The first four coefficients of the Blasius series are  $C_0 = 1$ ,  $C_1 = 1$ ,  $C_2 = 11$ , and  $C_3 = 375$ . Also, from Equation 17 the factor  $\zeta_1$  is related to  $f$  by  $\zeta_1 = f''(0)$  which is 0.33206. Equation 17 is conveniently written as

$$f'(\zeta) - \frac{u}{u_e} = 0 \quad (18)$$

Then, for a given  $\zeta$  line (which determines  $x$ ) and a selected number of points in the boundary layer, values for  $\zeta$  which give equal tangential velocity increments are calculated from Equation 18. The corresponding  $y$  distances are computed by using the definition of  $\zeta$  which yields

$$y = \zeta \left( \frac{x}{u_e} \right)^{\frac{1}{2}} \quad (19)$$

These computed  $y$  distances become the desired points near the body for the  $\zeta$  line intersections with the specified  $\zeta$  line.

The second part of the boundary layer grid line attraction technique involves calculating values of  $A_k$  and  $D$  which when used in  $Q$  give the desired  $\eta$  line spacing. Near the body surface, the  $\tau$  transformation equation, Equation 6b, can be written

$$(\eta_{yy_b}) \approx Q(\xi, \tau) \quad (20)$$

where variations with respect to  $x$  are neglected. If the expression for the forcing function  $Q$  in Equation 15 is substituted into Equation 20, then Equation 20 can be integrated with respect to  $\tau$  to obtain

$$\left(\frac{dr}{dy}\right)^2 = \sum_{k=1}^K 2(A_k/D) [\exp(-D H(r, r_k)] + H(\text{sgn}(r_k - r), 0.)$$

$$[1 - \exp(-D|r - r_k|)] \quad (21)$$

where the difference function  $H$  and sgn function are defined as follows

$$H(r, r_k) = \begin{cases} 0 & \text{if } r \leq r_k \\ r - r_k & \text{if } r > r_k \end{cases}$$

$$\text{sgn}(r_k - r) = \begin{cases} 1 & \text{if } r_k - r \geq 0 \\ -1 & \text{if } r_k - r < 0 \end{cases}$$

Now evaluate the expression for  $(dr/dy)^2$ , Equation 21, at  $r = 0$  and  $r = r_{\max} - \Delta r$  which gives the approximate expressions written in Equations 22 and 23, respectively.

$$\frac{1}{2} \left(\frac{dr}{dy}\right)^2 \Big|_{r=0} \doteq \frac{1}{D} \sum_{k=1}^K A_k \quad (22)$$

$$\frac{1}{2} \left(\frac{dr}{dy}\right)^2 \Big|_{r=r_{\max} - \Delta r} \doteq \frac{1}{D} \sum_{k=1}^K A_k \exp[-D(r_{\max} - \Delta r - r_k)] \quad (23)$$

The derivative in Equation 22 can be evaluated using the  $y$  values obtained previously. The derivative in Equation 23 can be specified by choosing an

$r_{\max}$  based on the placement of the outer boundary. Then Equations 22 and 23 can be combined to give the following equation for the damping factor D:

$$D = \ln 2 \left( \frac{dy}{dx} \right)^2 \Big|_{x=0} \left( \frac{dy}{dx} \right)^{-2} \Big|_{x=r_{\max}} - \frac{1}{2} \left( \frac{dy}{dx} \right)_{x=r_{\max}}^2 + r_E \quad (24)$$

With the damping factor D known, the analytic expression (Equation 21) can be evaluated on each interval of successive y values obtained from the Blasius solution along with the last  $\Delta x$  interval near the outer boundary. This procedure gives a system of K equations for the K unknowns  $A_k$  which are then solved. Therefore, values for the amplification factors and damping factor are obtained at each  $\xi$  line which are used to compute a body fitted grid system.

### C. Body Surface Point Distribution

The body surface can be defined by either a given set of points or by an analytical expression. The body surface grid points can then be determined by either interpolation or evaluation of the analytical expression.

The NACA 0012 airfoil section is used in this investigation. This airfoil has been used in several investigations (65) and is an AGARD (66) designated test airfoil section. The NACA four digit series airfoils have an analytic description of the body surface given by (67)

$$y_t(x) = 5t[0.2969x^{\frac{1}{2}} - 0.126x - 0.3516x^2 + 0.2843x^3 - 0.1015x^4] \quad (25)$$

where x is the distance along the chord (nondimensionalized by chord),  $y_t$  is the upper surface ordinate, and t is the thickness given as a fraction of the chord. For the NACA 0012 airfoil,  $t = 0.12$ . The thickness function given by Equation 25 does not close the body at the trailing edge ( $x=1$ ).

A circular arc is used to close the body. The arc is constructed to have a center on the chord line, to have points of tangency with the upper and lower airfoil surfaces near  $x = 0.99$ , and to intersect the chord line at  $x = 1.0$ .

The distribution of grid points on the airfoil surface is based on both resolving streamwise flow field gradients and defining the surface curvature. These criteria require the clustering of points in the nose and trailing edge regions of the airfoil. The following analytic transformation is used to obtain the desired clustered distribution of  $x$  abscissa values

$$x = \left[ \frac{\tanh\left(\frac{z - A_1}{A_2}\right) - \tanh\left(-\frac{A_1}{A_2}\right)}{\tanh\left(\frac{1 - A_1}{A_2}\right) - \tanh\left(-\frac{A_1}{A_2}\right)} \right]^{A_3} \quad (26)$$

where  $z$  represents the input set of equally incremented values ( $0 \leq z \leq 1$ ),  $x$  represents the clustered set of abscissae ( $0 \leq x \leq 1$ ), and  $A_1$ ,  $A_2$ , and  $A_3$  are arbitrary constants. The constant  $A_1$  determines the center of the hyperbolic function and is used to cluster points toward one end. The constant  $A_2$  varies the slope of the function at the center and thus determines the distribution near mid chord. The exponent  $A_3$  can also affect the clustering of points at the ends. If  $A_3 > 1$ , more points occur near  $x = 0$ ; while if  $A_3 < 1$ , points are clustered more at  $x = 1$ .

### SECTION III

#### GOVERNING EQUATIONS

The time dependent incompressible viscous Navier-Stokes equations for two-dimensional flows are presented. The primitive variables of fluid velocity and pressure are used. The Reynolds averaged Navier-Stokes equations are obtained. Boundary and initial conditions are given. A modified turbulence model based on Prandtl's mixing length theory is described which expresses the Reynolds stresses in terms of mean flow quantities for separated adverse pressure gradient flows. An expression for the force exerted by the flow field on the body is derived. The equations and boundary conditions are transformed by the curvilinear transformation discussed in Section II and written in the computational plane.

##### A. Basic Equations of Motion

The time dependent incompressible Navier-Stokes equations, which describe conservation of linear momentum, in orthonormal indicial notation are given by

$$\rho \left( \frac{\partial v_i}{\partial t} + \delta_j (v_j v_i) \right) = -\delta_i p + \delta_j \tau_{ji} \quad (27)$$

where  $\rho$  is the fluid density,  $p$  is the fluid static pressure,  $v_i$  are the components of fluid velocity, and  $\tau_{ji}$  is the viscous stress tensor. The subscript  $i = 1$  corresponds to the  $x$  direction and  $i = 2$  to the  $y$  direction. Conservation of mass for an incompressible flow is given by

$$\delta_j v_j = 0 \quad (28)$$

Turbulent flow is introduced by assuming that the flow quantities can be described in terms of mean and fluctuating quantities in the form

$$v_i = \bar{v}_i + v'_i \quad p = \bar{p} + p' \quad \tau_{ji} = \bar{\tau}_{ji} + \tau'_{ji}$$

where the bar (-) indicates a mean quantity and the prime ('') indicates a fluctuating quantity. In this form, a time average of a fluctuating quantity is assumed to be zero. Substitute these expressions into Equations 27 and 28 and time average each equation to obtain the Reynolds averaged Navier-Stokes equations for two-dimensional incompressible turbulent flow given below.

$$\frac{\partial \bar{V}_i}{\partial t} + \partial_j (\bar{V}_j \bar{V}_i) = -\partial_i \bar{p} + \partial_j (\bar{\tau}_{ji} - \bar{\tau} \bar{V}_j \bar{V}_i) \quad (29)$$

$$\partial_j \bar{V}_j = 0 \quad (30)$$

The term  $\bar{\tau} \bar{V}_j \bar{V}_i$  is known as the turbulent Reynolds stress. The incompressible form of the constitutive equation which relates the stress as a function of the rate of strain is now introduced as

$$\bar{\tau}_{ji} = \mu (\partial_j \bar{V}_i + \partial_i \bar{V}_j) \quad (31)$$

where  $\mu$  is the dynamic viscosity coefficient. The turbulent Reynolds stress is similarly modelled with an algebraic eddy viscosity approach based on Prandtl's mixing length theory. The corresponding expression is

$$-\bar{\tau} \bar{V}_j \bar{V}_i = \varepsilon_M (\partial_j \bar{V}_i + \partial_i \bar{V}_j) \quad (32)$$

where  $\varepsilon_M$  is the turbulent eddy viscosity. In this way, the additional unknown  $\bar{\tau} \bar{V}_j \bar{V}_i$  is expressed in terms of the mean flow variables. This turbulence closure requires, however, an expression for the eddy viscosity. Models for the eddy viscosity are examined in Section III C.

The expressions for the viscous laminar and turbulent stresses, Equations 31 and 32, are substituted into Equation 29 to obtain the simplified turbulent incompressible Navier-Stokes equations

$$\frac{\partial \bar{V}_i}{\partial t} + \partial_j (\bar{V}_j \bar{V}_i) = -\frac{1}{\rho} \partial_i \bar{p} + \frac{(\mu + \varepsilon_M)}{\rho} (\partial_j \partial_j \bar{V}_i + \partial_i \partial_j \bar{V}_j) \quad (33)$$

The following nondimensional variables are introduced:

$$\tilde{x}_i = \frac{x_i}{c}, \quad \tilde{v}_i = \frac{\tilde{v}_i}{U_\infty}, \quad \tilde{p} = \frac{\tilde{p} - p_\infty}{\frac{U_\infty^2}{c}}, \quad t = \frac{tU_\infty}{c} \quad (34)$$

where  $c$  is the airfoil chord,  $U_\infty$  is the freestream velocity, and  $p_\infty$  is the freestream static pressure. Substituting these nondimensional variables into Equations 30 and 33, with the time average and nondimensional symbols understood, gives the following set of equations

$$D = \cdot_j v_j = 0 \quad (35)$$

$$\frac{\partial v_i}{\partial t} + \cdot_j (v_j v_i) = -\tilde{s}_i \tilde{p} + \frac{1}{Re_t} (\tilde{s}_j \cdot_j v_i + \cdot_i \cdot_j v_j) \quad (36)$$

where  $D$  is the divergence of velocity and  $Re_t$  is the turbulent Reynolds number. The turbulent Reynolds number is defined as

$$Re_t = \frac{Re}{\frac{\epsilon_M}{L}} \quad (37)$$

where  $Re = U_\infty c / \nu$ , the Reynolds number.

Another simplification would be to apply Equation 35 in Equation 36. The divergence  $D$  is contained in both the convective and viscous terms. Although analytically correct, the velocity divergence is in general not identically zero in a numerical result. The approach used by Hodge (53) and developed by Harlow and Welch (51) is to keep the divergence  $D$  in the convective term as a correction term. This approach is used here so that the viscous divergence term is set equal to zero in Equation 36. Since the convective term is important throughout the flow field while the viscous term is important only near the airfoil surface, it appears reasonable to drop the viscous divergence term and keep the convective divergence term.

as a correction term. Thus, the appropriate set of equations becomes

$$\frac{\partial v_i}{\partial t} + \partial_j(v_j v_i) = -\partial_i p + \frac{1}{Re_t} (\partial_j \partial_j v_i) \quad (38)$$

$$D = \partial_j v_j \quad (39)$$

The calculation of pressure in the primitive variables formulation must be carefully handled. The pressure does not appear in the continuity equation nor does a time derivative of pressure occur. Two approaches have been extensively used to overcome this difficulty. Both techniques compute the pressure by utilizing the velocity divergence D as a correction factor. The calculated pressure is made to satisfy continuity. The first method, introduced by Chorin (68), computes pressure using an iteration procedure with D as the correcting term. The expression is

$$p^{(s+1)} = p^{(s)} - ;D \quad (40)$$

where s denotes the iteration number and ; is an acceleration parameter which can be either a constant or can be related to a successive-over-relaxation (SOR) solution of a Poisson equation for pressure as shown by Hodge (53). The second method uses a Poisson equation for pressure derived from the divergence of the momentum equation expressed in Equation 38.

The form of the equation is shown in Equation 41.

$$D_t = \nabla \cdot R - \nabla^2 p \quad (41)$$

where R represents the convective and viscous terms. If the R expression is algebraically simplified with D used wherever possible, the following simplified incompressible Poisson pressure equation is obtained

$$D_t = -[(uD)_x + (vD)_y + u_x^2 + 2u_x u_y + v_y^2 + uD_x + vD_y] \\ + \frac{1}{Re_t} (D_{xx} + D_{yy}) - (p_{xx} + p_{yy}) \quad (42)$$

This equation contains both spatial and time derivatives of the velocity divergence as well as the fluid velocities and pressure. Again, continuity is used as a correcting factor for calculating pressure. Further simplification can occur if small variations in the velocity divergence are assumed. In this case, the spatial derivatives of D are set to zero in Equation 42 and the result becomes

$$D_t + (u_x^2 + 2u_x u_y + v_y^2) = - (p_{xx} + p_{yy}) \quad (43)$$

Hodge (53) used both Equations 42 and 43 and found no apparent difference in the flow field solutions for his case of laminar flow. Also, Chorin's method of Equation 40 is related to the pressure Equation 43. Hodge (53) showed that the Chorin technique is approximately related to a solution of the Poisson pressure equation using SOR iteration on a coarse grid of twice the spacing. The Poisson pressure equation technique is chosen for the interior flow field because of the increased coupling which occurs in a finite difference representation. The body surface pressure, however, is calculated using the iteration technique of Equation 40. Here mass conservation is imposed directly and the difficulty of evaluating the Laplacian of pressure at the body surface in Equation 43 is avoided.

The following set of equations taken from Equations 38, 39 and 43 becomes the system used for the solution of incompressible turbulent viscous two-dimensional flow over airfoils:

$$u_t + uu_x + vu_y + uD = -p_x + \frac{1}{Re_t} (u_{xx} + u_{yy}) \quad (44)$$

$$v_t + uv_x + vv_y + vD = -p_y + \frac{1}{Re_t} (v_{xx} + v_{yy}) \quad (45)$$

$$D_t + u_x^2 + 2u_x u_y + v_y^2 = -(p_{xx} + p_{yy}) \quad (46)$$

$$D = u_x + v_y \quad (47)$$

The numerical solution of the governing equations is obtained by performing the computations in the computational plane obtained with the curvilinear transformation discussed in Section II. This method requires that the equations are transformed to the computational plane. The governing equations, Equations 44 through 47, are transformed using the relations given in Section II and Appendix A. The resulting set of corresponding transformed equations becomes:

$$u_T + \frac{u}{J} (y_x u_z - y_z u_x) + \frac{v}{J} (x_z u_x - x_x u_z) + u' =$$

$$= \frac{1}{J} (y_x p_z - y_z p_x) + \frac{1}{Re_t} \left( \frac{(u_{xz} - 2u_{xz})^2}{J^2} + \frac{u_{zz}}{J^2} \right)$$

$$+ u_x \left( \frac{\tau}{J^2} \right) + u_z \left( \frac{\tau}{J^2} \right)$$

$$v_T + \frac{u}{J} (y_x v_z - y_z v_x) + \frac{v}{J} (x_z v_x - x_x v_z) + v' =$$

$$= \frac{1}{J} (x_z p_x - x_x p_z) + \frac{1}{Re_t} \left( \frac{(v_{xz} - 2v_{xz})^2}{J^2} + \frac{v_{zz}}{J^2} \right)$$

$$+ v_x \left( \frac{\tau}{J^2} \right) + v_z \left( \frac{\tau}{J^2} \right)$$

$$p_T + \frac{1}{J^2} (y_x u_z - y_z u_x)^2 + 2(y_x v_z - v_x y_z)(x_z u_x - x_x u_z)$$

$$+ (x_z v_x - x_x v_z)^2 = - \frac{p_{xz}^2 - \frac{1}{J^2} (u_{xz}^2 + v_{xz}^2)}{J^2}$$

$$+ p_x \left( \frac{\tau}{J^2} \right) + p_z \left( \frac{\tau}{J^2} \right)$$

$$\tau = (u_x u_z - y_x u_y) + (x_z v_x - x_x v_z)$$

## B. Boundary and Initial Conditions

The complete definition of the flow problem requires the specification of sufficient boundary and initial conditions. The Navier-Stokes equations are coupled, nonlinear, first order in time, second order in space, elliptic partial differential equations. The elliptic nature of the equations for velocity requires boundary conditions at each boundary. The first order derivatives of pressure require a boundary condition describing the free-stream pressure. The time derivative terms require initial conditions on velocity and pressure throughout the flow field.

Boundary conditions on the airfoil surface are considered first. The continuum no-slip boundary condition for a viscous fluid at a stationary solid surface is imposed on the tangential velocity at the surface. In addition, the normal component of velocity must be zero for a stationary surface with no transpiration. These conditions are met by the specification of the Dirichlet boundary conditions

$$u_b = 0 \quad v_b = 0 \quad (5.2)$$

where the subscript b denotes body surface. The pressure on the airfoil surface is computed, and no body boundary condition is required by the first derivative pressure term.

The far-field boundary conditions for velocity and pressure specify the free-stream flow field. Let  $\mathbf{r}$  be a position vector in the flow field with the origin at the airfoil mid-chord. Then, as the distance  $r$  from the airfoil becomes large the fluid velocity and pressure approach their nondimensional freestream values as follows:

$$\begin{aligned} \text{lim}_{r \rightarrow \infty} (u + v i) &= \cos \alpha i + \sin \alpha j \\ r &\rightarrow \infty \end{aligned} \quad (5.3)$$

$$\begin{aligned} \text{lim}_{r \rightarrow \infty} p &= p_0 \\ r &\rightarrow \infty \end{aligned} \quad (5.4)$$

where  $\alpha$  is the angle of attack of the airfoil chord with respect to the freestream.

The first order time derivative terms require initial conditions for the velocity and pressure in the field. From a theoretical viewpoint, since the asymptotic steady solution is desired, any continuous initial specification of velocity and pressure (subject to the prescribed boundary condition) is permissible.

The boundary conditions and initial conditions are also transformed to the computational plane. The values for each condition remain unaltered and are thus not repeated here. The location in the transformed plane depends on the specific transformation chosen to generate the computational grid. This matter is discussed in Section IV where the numerical procedures are described. The sensitivity analysis of the outer boundary location is addressed in Appendix F.

### C. Turbulence Model

Turbulence modelling is of considerable interest in theoretical, experimental, and computational research work. Many aerodynamic problems of practical interest contain regions of turbulent flow. Several models have been developed which vary in complexity from Prandtl's mixing length theory to techniques employing auxiliary differential equations for mixing length, viscosity coefficients, and turbulent kinetic energies. The accuracy of each model varies with both the geometry and the flow field quantity used for comparing results. In computational work, the ability to translate the turbulence model into numerical procedures and the computer resources required are additional factors which need to be considered.

In this investigation, turbulence is modelled with an algebraic eddy viscosity approach based on Prandtl's mixing length theory. The basic concept of this method is that the turbulent Reynolds stress,  $\tau_{ij}^{turb}$ ,

can be related to the strain rate of the mean flow in a way analogous to that for laminar viscous stresses. The fundamental expression was previously introduced in Equation 32 to obtain the simplified turbulent incompressible Navier-Stokes equation, Equation 33. The algebraic eddy viscosity has been used extensively in obtaining numerical solutions for a variety of aerodynamic problems (24,25,69).

The eddy viscosity model for turbulent flow with zero pressure gradient near a solid surface, which incorporates the modifications of Cebeci and Smith (63), Van Driest (23), and Deiwert (57), is given below and then discussed.

$$\epsilon_i = \left( k_1 \frac{v_p}{L} \right)^2 \left( \bar{u}_y^2 + \bar{v}_x^2 \right) \quad (55)$$

$$\epsilon_o = \left( k_2 \frac{\bar{u}}{u_e} \right)^6 \quad (56)$$

$$n_L = 1 - \exp \left[ - \frac{y}{A} + \left( \frac{\tau_b}{\bar{u}^2} \right)^{1/2} \right] \quad (57)$$

$$\tau = 1 + 5.5 \left( y/\delta \right)^6 \quad (58)$$

$$\delta^* = \int_0^y \left( 1 - \frac{\bar{u}}{\bar{u}_e} \right)^{-1} dy \quad (59)$$

The tangential surface direction is given by  $x$  and the normal surface direction by  $y$ . The inner and outer eddy viscosities,  $\epsilon_i$  and  $\epsilon_o$ , model the Law of the Wall and Law of the Wake (70) regions. The inner mixing length is assumed proportional to the distance  $y$  from the surface.  $k_1$  is the Von Karman constant. The Van Driest (23) damping factor models the laminar sublayer region where  $\tau_b$  is the surface shear stress and  $A^*$  is the decay constant. The displacement thickness  $\delta^*$  defined by Equation 59 is the outer layer length scale. The intermittency factor  $\tau$ , defined in Equation 58, models the decrease of the turbulence intensity from a fully turbulent region to the inviscid region away from the body surface. The intermittency is a function of the normal distance from the wall.

nondimensionalized by the local boundary layer distance  $\delta$ . The local edge boundary layer velocity  $u_e$  is the outer layer characteristic velocity. The standard Cebeci-Smith (63) values for the constants are  $k_1 = .41$ ,  $k_2 = .0168$ , and  $A^+ = 26$ . Continuity of the eddy viscosity distribution is achieved by switching from the inner to the outer model whenever  $\delta$  first exceeds  $x_e$ .

Recently, Jobe and Hankey (71) compared this eddy viscosity model given by Equations 55 through 59 with experimental data for several constant adverse pressure gradient attached flows. They varied the  $k_1$ ,  $k_2$ , and  $A^+$  parameters in a numerical turbulent boundary layer program until the solutions matched the experimental boundary layer velocity profiles and skin friction coefficients. These parameters had substantially different values than the previously cited values obtained for zero pressure gradient flows. They found that when the flow encounters an adverse pressure gradient the inner eddy viscosity parameters rapidly adjust to the values of  $k_1 = .65$  and  $A^+ = 50$ . The outer eddy viscosity constant appears to linearly increase with distance measured from the start of the adverse pressure gradient. Thus Jobe and Hankey (71) found that  $k_2$  can vary from a value of  $.0168$  to values of  $.03$  or greater given that the adverse pressure gradient exists for a sufficient length downstream.

The use of an eddy viscosity model similar in form to the one given in Equations 55 through 59 for an airfoil at angle of attack requires examination of the typical flow field characteristics. The upper surface of the airfoil has a pressure distribution which includes a region of low pressure, the suction peak, near the airfoil leading edge. The suction peak is followed by an adverse pressure gradient region. The pressure gradient tends to decrease as the flow recovers toward the trailing edge. The

turbulence model that is used for an upper surface turbulent boundary layer should include the effects of this adverse pressure gradient. The inner eddy viscosity parameters, therefore, take on the Jobe and Hankey (71) values of  $k_1 = .65$  and  $A^+ = 52$  in this region. The outer eddy viscosity parameter  $k_2$  may also change in the adverse pressure gradient region. However, the rate of change is affected by the pressure gradient and downstream distance. The pressure gradient does decrease rapidly as the flow proceeds downstream. Any tendency for  $k_2$  to increase is probably offset by the decreasing adverse pressure gradient. Thus, the value of  $k_2$  is kept at the equilibrium value of .0168.

The eddy viscosity model with the discussed adverse pressure gradient modifications is now written in terms of the nondimensional variables introduced in Equations 34 and 37. All length quantities are nondimensionalized with respect to the airfoil chord. The mean and nondimensional quantities are henceforth implied. The eddy viscosity model becomes

$$\frac{\partial}{\partial x} \left( k_1 P_L \right)^2 (u_y^2 + v_x^2) = Re \quad (65)$$

$$\frac{\partial}{\partial x} = k_2 u_e \epsilon^* Re \quad (66)$$

$$P_L = 1 - \exp \left[ - \frac{x}{A^+} (u_{yb} Re) \right] \quad (67)$$

$$\epsilon^* = [1 + 5.5 (\gamma/\beta)^{6.5}]^{-1} \quad (68)$$

$$\epsilon^* = \int_0^x \left( 1 - \frac{u}{u_e} \right) dy \quad (69)$$

where  $k_1$ ,  $k_2$  and  $A^+$  are considered adverse pressure gradient parameters.

The eddy viscosity model must also represent the physical characteristics in large separated regions which occur during airfoil stall. Trailing edge

stall occurs when the turbulent boundary layer separation moves toward the leading edge of the airfoil as the angle of attack increases. The pressure distribution in a trailing edge separated region has small gradients (72). This observation motivates another change to the eddy viscosity model. The inner eddy viscosity parameter is relaxed back toward the equilibrium value of .41. The separation point, which precedes the return to zero pressure gradient, is selected as the point to start the exponential decay. The following relaxation form with distances nondimensionalized by the chord is used

$$f = A \cdot 1 + B \exp\left(-\frac{s - s_d}{s_r}\right) \quad s \geq s_d$$

$$f = 1 \quad s < s_d \quad (6.5)$$

where  $f$  is the relaxation factor which multiplies the initial value of  $k_{1i}^2$ ,  $k_{1f}^2$ ,  $s$  is the distance downstream from the trailing edge separation point,  $s_d$  is the delay distance,  $s_r$  is the relaxation distance, and  $A$  and  $B$  are constants. The constants  $A$  and  $B$  are determined by applying the conditions  $f = 1$  at  $s = s_d$  and  $f = k_{1f}^2/k_{1i}^2$  as  $s$  approaches infinity where  $k_{1f}$  is the asymptotic value of  $k_1$  downstream. Thus,  $A$  and  $B$  become

$$A = k_{1f}^2/k_{1i}^2 \quad B = A^{-1} - 1 \quad (6.6)$$

Measurements of Bachalo (73) and Baker (74) in the trailing edge separation region indicate the presence of a lower but finite turbulent intensity when compared with the separated turbulent shear layer. The velocity derivative terms in the inner eddy viscosity and damping factor expressions, Equations 60 and 62, can approach zero in a region near a velocity inflection point. In this case, a zero eddy viscosity is permitted in a turbulent separated region which is contrary to the apparent flow structure. This same zero eddy viscosity behavior can also occur in the case of shedding separation bubbles from the airfoil surface. In order to prevent the appearance of

laminar regions within the turbulent, adverse pressure gradient, separated flow field during airfoil stall, a limiting technique is employed. The inner eddy viscosity is prevented from decreasing in value as the normal distance from the surface increases. This restriction simulates the uniform turbulent intensities measured (73,74) in the trailing edge separated region. The inner eddy viscosity is further limited by imposing a condition of no decrease in the downstream direction. This limit provides for a finite turbulent intensity in separated regions which may develop in the turbulent boundary layer. The limit is initiated by obtaining the distribution of eddy viscosity in the attached boundary layer near the leading edge of the airfoil. This distribution  $\varepsilon_{ic}$  is compared with the distributions calculated by the model at downstream locations. The outer eddy viscosity, which has no velocity derivative, is not limited in any way. The "limiting" technique is passive in the sense that the locally computed value for the inner eddy viscosity is used whenever possible. Numerical experiments without the "limiting" technique displayed unphysical results because the conventionally modelled eddy viscosity is divergent. The inception of separated flow decreased the eddy viscosity thereby causing further separation. The "limiting" concept is necessary to prevent this unphysical result.

The transition from laminar flow to fully turbulent flow is modelled using the transition model of Dhawan and Narasimha (75). The expression for the transition factor  $\Gamma$  is given below

$$\Gamma = 1 - \exp\left(-.412\left(\frac{x - x_t}{l}\right)^2\right) \quad (67)$$

where  $x$  is the tangential direction coordinate on the body surface,  $x_t$  is the location where transition starts, and  $l = x_{t=3/4} - x_{t=1/4}$  defines the distance required to expand from  $\Gamma = 1/4$  to  $\Gamma = 3/4$ .

Some of the expressions in the turbulent boundary layer eddy viscosity

model are conveniently expressed in terms of quantities in the transformed plane described in Section II. The velocity derivatives in the inner eddy viscosity model are formulated by determining the tangential and normal components of velocity,  $\tilde{u}$  and  $\tilde{v}$  respectively, to the body surface  $r = r_1$  at a position  $\xi$ .

$$\tilde{u}(\xi, r) = c_2 u(\xi, r) - c_1 v(\xi, r) \quad (68)$$

$$\tilde{v}(\xi, r) = c_1 u(\xi, r) + c_2 v(\xi, r) \quad (69)$$

where  $c_1$  and  $c_2$  are components of the unit outward normal to the body surface at position  $(\xi, r_1)$  given by

$$c_1 = -y_{r_1} / \sqrt{r_1} \quad c_2 = x_{r_1} / \sqrt{r_1}$$

Then, the directional derivative definition is used to obtain the surface normal derivative of  $\tilde{u}$  and the surface tangential derivative of  $\tilde{v}$  expressed as

$$\frac{\partial \tilde{u}}{\partial n} = [c_1(y_{r_1} \tilde{u}_\xi - y_\xi \tilde{u}_{r_1}) + c_2(x_{r_1} \tilde{u}_\eta - x_\eta \tilde{u}_{r_1})]/J \quad (70)$$

$$\frac{\partial \tilde{v}}{\partial s} = [c_2(y_{r_1} \tilde{v}_\xi - y_\xi \tilde{v}_{r_1}) - c_1(x_{r_1} \tilde{v}_\eta - x_\eta \tilde{v}_{r_1})]/J \quad (71)$$

which correspond to the  $u_y$  and  $v_x$  derivatives of the Cartesian eddy viscosity model expressions, Equations 60 through 64.

The turbulence structure in the far wake is modelled with an eddy viscosity expression similar to the outer eddy viscosity model in the turbulent boundary layer. The model is based on the assumption of a self-preserving, equilibrium turbulent wake with constant pressure in incompressible flow. The approach has been experimentally investigated by Narasimha and Prabhu (76) who obtained the following expression

$$\epsilon_w = k_3 w_o^2 \quad (72)$$

where  $w_o(x) = \max_y (U_o - u(x, y))$  is the maximum velocity defect in the wake,  $w_o$  is a half wake width defined where the velocity defect becomes one half the maximum value, and  $k_3$  is a constant equal to .065. If the experimentally

integrated value of the wake defect function is used, then Equation 72 can be written in terms of the parameters of edge velocity and displacement thickness similar to boundary layers as follows:

$$\frac{\delta_w}{\delta_e} = k_3 u_e \delta_w^* Re \quad (73)$$

where  $u_e$  is the nondimensional velocity at the edge of the wake,  $\delta_w^*$  is the nondimensional displacement thickness for the half wake as defined by Equation 64, and  $k_3$  becomes .0634. This expression has been utilized by Green, et al (77) in an integral method for predicting two-dimensional incompressible and compressible turbulent wakes of lifting airfoils. For an incompressible, constant pressure wake the momentum integral equation reduces to a statement that the momentum thickness is a constant. These conditions exist in the far wake of an airfoil. In addition, in the far wake the displacement and momentum thicknesses become equal as shown by the experimental results of Narasimha and Prabhu (76). Thus the far wake eddy viscosity is approximately constant. The transition in the wake from the turbulent core region to the inviscid freestream region on each side of the wake is modelled with the intermittency factor of Equation 63 where  $\delta$  is now the wake half width and  $y$  is the normal distance from the wake center.

The turbulent near wake region mixing rates where the wall boundary layers merge and eventually become the far wake are not well understood from either an analytical or experimental viewpoint. In the flow regime under consideration, a laminar boundary layer from the lower airfoil surface mixes with a turbulent boundary layer from the upper surface. An eddy viscosity model similar to that used in the outer turbulent boundary layer and the far wake is used. Inouye, et al (78) applied the Cebeci-Smith (63) outer layer model in the near wake of a flat plate and obtained good agreement for the mean velocity profiles. They allowed the constant  $k_2$  to reach twice the

equilibrium value of .0168 over a length of one chord from the trailing edge. The computed eddy viscosity was still about 50% low when compared with experiment at the one chord distance. Later, Burggraf (79) compared several turbulence models for various near wake flows and concluded that the Cebeci-Smith model adequately predicted the mean velocity profiles.

The merging of the upper and lower surface boundary layers is modelled with a simplified interaction hypothesis approach introduced by Bradshaw (80). The two layers are initially allowed to develop downstream a distance  $WL_1$  without interaction. At this point the eddy viscosity is increased exponentially in the adjacent laminar boundary layer from a zero value to the far wake calculated value  $\varepsilon_{ow}$  at a distance  $WL_2$  from the trailing edge. This eddy viscosity variation is formulated as follows

$$\begin{aligned}\varepsilon &= 1/2 \varepsilon_{ow} \left(1 + \tanh\left(8 \frac{s - WL_{av}}{WL_2 - WL_1}\right)\right) & s > WL_1 \\ \varepsilon &= 0 & s \leq WL_1\end{aligned}\quad (74)$$

where  $WL_{av}$  is the distance from the trailing edge to a location half way between the distances  $WL_1$  and  $WL_2$  and  $s$  is the local distance from the trailing edge. The coefficient 8 is selected so that  $\varepsilon = 0$  at  $s = WL_1$  and  $\varepsilon = \varepsilon_{ow}$  at  $s = WL_2$  because at  $s = WL_2$  the hyperbolic tangent function becomes equal to 0.9993 while at  $s = WL_1$  it becomes - 0.9993. The eddy viscosity profile in the turbulent boundary layer near the trailing edge is extended into the near wake.

#### D. Force Coefficients

The force which is exerted on the body by the moving fluid around the body can be determined from the Cauchy integral equation for conservation of linear momentum applied at the body surface or on a closed path surrounding the body. The basic expressions for the force coefficients formulated

in the  $(x, y)$  physical plane coordinate system are given by Equations D.12a and D.12b derived in Appendix D for an incompressible turbulent viscous flow.

Consider first the body surface where the components of velocity are identically zero from the no slip boundary conditions. In this case, the equations become

$$C_{fx} = \int_{S_b} \left[ -2n_1 p + \frac{1}{Re} (4n_1 \frac{\partial u}{\partial x} + 2n_2 (\frac{\partial u}{\partial y} + \frac{\partial v}{\partial x})) \right] ds \quad (75)$$

$$C_{fy} = \int_{S_b} \left[ -2n_2 p + \frac{1}{Re} (2n_1 (\frac{\partial u}{\partial y} + \frac{\partial v}{\partial x}) + 4n_2 \frac{\partial v}{\partial y}) \right] ds \quad (76)$$

where the integration is over the body contour denoted by  $S_b$ . The first term in each expression is the contribution caused by pressure forces while the second term is the viscous stress contribution.

The force coefficients, Equations 75 and 76, determined at the body surface can be transformed to the computational plane by using the relations for the outward normal vector to an  $\eta$  contour, line integrals and derivatives given in Appendix A. The transformed equations become

$$C_{fx} = 2 \int_{\xi_{\min}}^{\xi_{\max}} \left[ y_\xi p + \frac{1}{ReJ} (y_\xi u_{\eta\xi} + y_\xi (y_\eta u_\eta - x_\eta v_\eta)) \right] d\xi \quad (77)$$

$$C_{fy} = 2 \int_{\xi_{\min}}^{\xi_{\max}} \left[ -x_\xi p + \frac{1}{ReJ} (x_\xi v_{\eta\xi} - x_\xi (y_\eta u_\eta - x_\eta v_\eta)) \right] d\xi \quad (78)$$

where the no slip boundary condition which implies  $u_\xi = v_\xi = 0$  on the body surface is used. The viscous stress terms are further simplified by using continuity at the body surface and the vorticity ( $\zeta \propto y$ ) Equation A.14 on the body surface to obtain

$$C_{fx} = \int_{\xi_{min}}^{\xi_{max}} \left( 2y_{\xi p} - \frac{2x_{\xi p}}{Re} \right) d\xi \quad (79)$$

$$C_{fy} = \int_{\xi_{min}}^{\xi_{max}} \left( -2x_{\xi p} - \frac{2y_{\xi p}}{Re} \right) d\xi \quad (80)$$

where the vorticity on the body surface  $\omega$  is given by

$$\omega = - (y_v v_r + x_v u_r) / J \quad (81)$$

The corresponding moment (positive counterclockwise) about a point P located within the body cross-section with coordinates  $(x_p, y_p)$  is given as

$$C_{MP} = \int_{\xi_{min}}^{\xi_{max}} \left[ (x - x_p) \left( -2x_{\xi p} - \frac{2y_{\xi p}}{Re} \right) - (y - y_p) \left( 2y_{\xi p} - \frac{2x_{\xi p}}{Re} \right) \right] d\xi \quad (82)$$

Next consider again the more general case of a closed path around the body whose force coefficients are given by Equations D.12a and D.12b. Assume that the closed path is an  $\gamma$  contour. Then, using the transformed expressions in Appendix A for the outward normal vector to an  $\gamma$  contour, integrals, and derivatives, the force coefficients for the body in terms of quantities on a constant  $\gamma_p$  line in the flow field become

$$C_{fx} = \int_{\xi_{min}}^{\xi_{max}} \left[ 2y_{\xi p} + \frac{2}{Re} \frac{2}{J} [u_r (x_r^2 + 2y_r^2) - u_r (x_r x_r + 2y_r y_r) + v_r (x_r y_r) - v_r (x_r y_r)] + 2u(u_y - vx_p) \right] d\xi - \frac{1}{J} \int_{B_p}^P \int_{\xi_{min}}^{\xi_{max}} 2u \, d\xi \, d\gamma \quad (83)$$

$$C_{f_y} = \int_{\xi_{\min}}^{\xi_{\max}} \left\{ -2x_{\xi} p + \frac{2}{Re_t J} [v_{\eta}(2x_{\xi}^2 + y_{\xi}^2) - v_{\xi}(2x_{\xi}x_{\eta}) + u_{\xi}(x_{\eta}y_{\xi}) - u_{\eta}(x_{\xi}y_{\xi})] + 2v(u_{\xi} - vx_{\xi}) \right\} d\xi - \frac{2}{\delta t} \int_{r_b}^{r_p} \int_{\xi_{\min}}^{\xi_{\max}} 2v[J] d\xi dr \quad (84)$$

where  $r_b \leq r_p \leq r_{\max}$ . The terms in the line integral represent in order pressure forces, viscous forces, and convective outflows of linear momentum. The area integral term is the time rate of increase of linear momentum contained in the control volume bounded by the body  $r_b$  contour and the selected  $r_p$  contour.

The corresponding lift and drag coefficients are then calculated using Equations D.13 and D.14.

## SECTION IV

### NUMERICAL METHOD

The numerical methods used to obtain solutions for incompressible turbulent flow over airfoils are presented. The numerical finite difference procedure which yields the grid transformation is first discussed. The implicit finite difference method for obtaining approximate solutions to the unsteady, incompressible, turbulent Navier-Stokes equations is next described. Numerical boundary conditions and initial conditions are considered. The numerical procedure for incorporating the turbulent eddy viscosity model is discussed. The computation of the force coefficients on the body is then presented.

#### A. Grid Transformation

The numerical solution of the governing equations for the transformation is carried out in the transformed or computational plane on a square mesh ( $\xi$ ,  $\tau$ ) system. The body contour  $C_b$  and the far field boundary  $C_f$  become constant  $\tau$  contours (Figure 1). The far field boundary is usually used to approximate infinity in incompressible flow problems. Constant  $\tau$  contours in the physical plane are required to transform to equi-spaced  $\tau$  coordinate lines with unit step size in the transformed plane. The spacing of  $\tau$  contours in the physical plane is controlled by the set of elliptic equations. The  $\xi$  contour spacing on the body surface and outer boundary in the physical plane is determined by the chosen point distribution on each surface. The constant  $\xi$  contours are also required to transform to equi-spaced  $\xi$  coordinate lines with unit step size in the transformed plane. The  $\xi$  lines are denoted by the subscript  $i$  with range  $1 \leq i \leq I_{MAX}$  where  $I_{MAX}$  is the number of  $\xi$  lines. Similarly, the  $\tau$  lines are identified by a subscript  $j$  with range

of  $1 \leq j \leq JMAX$  where  $JMAX$  is the number of  $\gamma$  lines. The values  $j = 1$  and  $j = JMAX$  are the body and outer boundary surfaces, respectively. The constant  $\gamma$  lines  $i = 1$  and  $i = IMAX$  denote the branch cut in the physical plane and are therefore identical.

The governing elliptic transformation equations, Equations 9a and 9b, are written with finite differences in quasi-linearized form for the location  $(i, j)$ . Second order accurate central differences given in Appendix B are used for evaluating each term. The highest order derivative contains the unknown at location  $(i, j)$  while the transformation coefficients, which contain lower order derivatives, are evaluated with previous values of the variables  $x$  and  $y$ . The difference expressions are given below where the indices  $i$  and  $j$  are understood when omitted.

$$x_{ij} = \frac{\alpha(x_{i+1} + x_{i-1}) - \frac{s^2}{2}(x_{i+1,j+1} - x_{i+1,j-1} + x_{i-1,j+1} - x_{i-1,j-1})}{\gamma(x_{j+1} + x_{j-1}) + \frac{J^2}{2}[(x_{i+1} - x_{i-1})P + (x_{j+1} - x_{j-1})Q]/2(\gamma + \beta)} \quad (85)$$

$$y_{ij} = \frac{\beta(y_{i+1} + y_{i-1}) - \frac{s^2}{2}(y_{i+1,j+1} - y_{i+1,j-1} + y_{i-1,j+1} - y_{i-1,j-1})}{\gamma(y_{j+1} + y_{j-1}) + \frac{J^2}{2}[(y_{i+1} - y_{i-1})P + (y_{j+1} - y_{j-1})Q]/2(\gamma + \beta)} \quad (86)$$

The  $i$  index near the branch cut is adjusted as follows:

when $i = 1$	then $i - 1 = IMAX - 1$
when $i = IMAX - 1$	then $i + 1 = 1$
when $i = IMAX$	then $i = 1$

The set of finite difference equations has the range of indices given by  $1 \leq i \leq IMAX - 1$  and  $2 \leq j \leq JMAX - 1$  which results in  $(IMAX-1)(JMAX-2)$  equations for the unknown values of  $x$  and  $y$  at the interior grid points.

The system of difference equations is solved using successive over relaxation (SOR) iteration. For a general function  $f$ , an approximate solution for  $f$  using SOR iteration has the form

$$f^{(s+1)} = \omega f^* + (1 - \omega)f^{(s)} \quad (87)$$

where  $s$  represents the iterate number,  $\omega$  is an acceleration parameter, and  $*$  represents the current value of  $f$  calculated from the difference equation. The acceleration parameter is always one for the first iteration. The system of linearized difference equations given by Equations 85 and 86 obtained from the elliptic generating differential equations is consistently ordered (81). Thus, local optimum acceleration parameters  $\omega_{ij}$  can be calculated from matrix theory (81) and are given by Hodge (52). Convergence of the iteration procedure is determined by comparing the absolute value of the difference in successive iterates with a prescribed error criteria  $E$ .

The SOR iteration technique requires an initial guess for the solution. Geometric contours with a shape similar to the outer computational boundary are used for constant  $\tau$  lines and straight lines which emanate from the body center are used for  $\delta$  lines. A similar approach has been successfully used by Thames (44) and Hodge (53).

The forcing function  $Q(\tau, \delta)$  defined by Equation 15 is evaluated throughout the  $(\tau, \delta)$  plane following the procedure described in Section II.B. The similarity parameter values  $\tau$  (which give equal increments of tangential velocity for a specified number of boundary layer points) are calculated from Equation 18 using Newton-Raphson iteration. The equivalent  $y$  values at a given  $x(\delta$  line) are found from the similarity relation, Equation 19. The  $y$  derivatives given by Equations 22 and 23 are then approximated using the above values for  $y$  and the specified  $\tau$  differences as follows:

$$\left(\frac{dy}{dx}\right)^2 = (y_j - y_1)^{-2} \quad \text{at } x = 0 \quad (25)$$

$$\left(\frac{dy}{dx}\right)^2 = (y_j)^{-2} \quad \text{at } x = x_{\max} = 1/2$$

where  $\Delta x = 1$ ,  $y_j$  are the boundary layer  $y$  values, and  $|y_j|$  is the specified far field  $y$  difference between the last two points on the given  $x$  line.

Then the damping factor  $D$  is found using Equation 24. Next the analytical expression for  $dy/dx$  in Equation 21 is evaluated on the far field interval  $|y_j|$  and on each boundary layer  $dy$  interval determined by the  $y_j$  values.

This system of equations for  $A_k(\beta)$  is solved using Gauss elimination. Thus, for a given  $x$  line, values for  $A_k$  and  $D$  are calculated for use in evaluating the  $Q(x, \cdot)$  forcing function. This function is then used during the SOR iteration for the transformation values of  $x$  and  $y$ .

Additional  $x$  contours can be added in the wake region by using the interpolating technique given in Appendix C.

#### B. Navier-Stokes Finite Difference Equations

Approximate solutions of the unsteady, Reynolds averaged, incompressible, turbulent, Navier-Stokes equations are obtained by using an implicit finite difference procedure. Explicit numerical methods can be used to obtain approximate solutions by advancing the time by small increments. The allowable time increments are constrained by numerical stability criteria. Implicit finite difference methods can also provide approximate solutions by marching in time with small time steps. Implicit methods usually do not have numerical stability constraints imposed on the time step. However, at each time step a large system of simultaneous difference equations must be solved. A matrix iterative technique such as SOR iteration is an attractive solution method because of the large matrix size. Convergence criteria are the introduced in place of stability criteria.

The implicit method consists of both a linearization of the equations and the application of finite differences to those equations. The x component, transformed, momentum equation given by Equation 48 is considered first. Re-arranging the convective terms, the equation becomes

$$u_t + u_x(u_{xx} - v_{xj}) + u_y(v_{xy} - u_{yj}) + u p = -p_x \frac{\Delta x}{J^2} + p_y \frac{\Delta y}{J^2} + \frac{1}{Re_t} \frac{u_{yy} - 2u_{xy} + u_{xx}}{J^2} + u_x \left( \frac{\cdot}{J^2} \right) + u_y \left( \frac{\cdot}{J^2} \right) \quad (89)$$

Equation 89 is now written in quasi-linear form where lower order derivatives of the variables occur in "coefficients". The current value for the unknown variable at location (i, j) occurs in the highest order derivative of each term while the "coefficients" are evaluated with the last available values for the variables  $u$ ,  $v$ , and  $p$ . In this form, the coefficient of  $u_x$  in the convective terms,  $(u_y - v_x)/J$ , is proportional to the component of velocity in the  $J$  direction. Similarly, the coefficient of  $u_y$  in the convective terms,  $(v_x - u_y)/J$ , is proportional to the component of velocity in the  $x$  direction. These quantities are designated UC and VC, respectively.

Finite difference expressions given in Appendix B are used to approximate the terms in Equation 89. First order accurate backward differences are used for the time derivative. The first derivatives of pressure are approximated with second order accurate central differences. Likewise, second order central difference expressions are used for the second derivatives of velocity in the viscous terms. Second order accurate upwind differencing is used for the velocity first derivatives in the convective terms. The quantities UC and VC determine the sign of the local velocity in the  $J$  and  $x$  directions. If UC  $\geq 0$ , then backward upwind differencing is used for the  $J$  derivatives while UC  $< 0$  dictates forward upwind differencing. Also, backward upwind differencing for  $x$  derivatives occurs if VC  $= 0$  while forward

upwind differencing is used if  $VC < 0$ . Second order accurate upwind differences are also used for the velocity first derivatives in the viscous terms. The direction is determined by the sign of the coefficients. Points on the  $J = 2$  and  $J = JMAX - 1$  contours use first order upwind differences for first derivatives if the velocity direction indicates flow from the body surface ( $J=1$ ) or the outer boundary ( $J = JMAX$ ). Near the body surface the grid spacing is extremely small, and velocity gradients are small near the outer boundary. Thus, in both cases the associated artificial viscosity has a negligible effect. The transformation derivatives in Equation 89 are evaluated with second order central differences. The velocity derivatives in the velocity divergence term are also evaluated using central differences.

Difference equations are written with the following convenient conventions. Terms which contain unknowns at location  $(i,j)$  are fully subscripted. The finite difference expression for location  $(i,j)$  as described previously is understood when only the term is given. The subscripts  $(i,j)$  and superscript  $n$  are assumed when omitted. The resulting difference equation for Equation 89 becomes

$$\begin{aligned}
 \frac{u_{ij} - u_{ij}^{n-1}}{\Delta t} + (3u_i - 4u_{IC1} + u_{IC2}) VC + (3u_j - 4u_{JC1} + u_{JC2}) WV + d \\
 = -\frac{y_i}{2J} (p_{i+1} - p_{i-1}) + \frac{y_j}{2J} (p_{j+1} - p_{j-1}) \\
 + \frac{1}{Re_t} \left( \frac{1}{J^2} (u_{i+1} - 2u_{ij} + u_{i-1}) + \frac{1}{J^2} (u_{j+1} - 2u_{ij} + u_{j-1}) \right) \\
 - \frac{1}{2J^2} (u_{i+1,j+1} - u_{i-1,j+1} + u_{i-1,j-1} - u_{i+1,j-1}) \\
 - (3u_i - 4u_{IV1} + u_{IV2}) V_1 - (3u_j - 4u_{JV1} + u_{JV2}) V_2
 \end{aligned} \quad (89)$$

where

for  $UC \geq 0$  for  $UC < 0$

$IC1 = i - 1$   $IC1 = i + 1$

$IC2 = i - 2$   $IC2 = i + 2$

for  $VC \geq 0$  for  $VC < 0$

$JC1 = j - 1$   $JC1 = j + 1$

$JC2 = j - 2$   $JC2 = j + 2$

and  $UV = -\zeta/2J^2$  and  $VV = -\xi/2J^2$

where

for  $UV \geq 0$  for  $UV \leq 0$

$IV1 = i - 1$   $IV1 = i + 1$

$IV2 = i - 2$   $IV2 = i + 2$

for  $VV \geq 0$  for  $VV \leq 0$

$JV1 = j - 1$   $JV1 = j + 1$

$JV2 = j - 2$   $JV2 = j + 2$

The difference equation for conservation of mass, Equation 51, for location  $(i, j)$  is given by

$$D = \frac{y_r}{2J} (u_{i+1} - u_{i-1}) - \frac{x_r}{2J} (v_{i+1} - v_{i-1}) - \frac{y_z}{2J} (u_{j+1} - u_{j-1}) \\ + \frac{x_z}{2J} (v_{j+1} - v_{j-1}) \quad (91)$$

The following finite difference derivatives and coefficients at location  $(i, j)$ :

$$\text{XETA} = x_r/2J \quad \text{XXI} = x_r/2J$$

$$\text{YETA} = y_r/2J \quad \text{YXI} = y_r/2J$$

$$\text{ALFA} = \alpha/J^2 \quad \text{GAMA} = \gamma/J^2 \quad \text{BETA} = -\xi/2J^2$$

With these definitions, Equation 90 can be written to provide an expression

for  $u_{ij}^n$  given by

$$\begin{aligned}
u_{ij}^* = & u_{ij}^{n-1} + \Delta t [-\text{YETA}(p_{i+1} - p_{i-1}) + \text{XXI}(p_{j+1} - p_{j-1}) \\
& + 'VC' (4u_{IC1} - u_{IC2}) + 'VC' (4u_{JC1} - u_{JC2}) - u] \\
& + \frac{1}{Re_t} [\text{ALFA}(u_{i+1} + u_{i-1}) + \text{GAMA}(u_{j+1} + u_{j-1}) \\
& + \text{BETA}(u_{i+1,j+1} - u_{i+1,j-1} + u_{i-1,j+1} - u_{i-1,j-1}) + 'VV' (4u_{JV1} - u_{JV2}) \\
& + 'VV' (4u_{JV1} - u_{JV2})] / [1 + \Delta t (3('VC' + 'VC' + 'VV' + 'VV')) \\
& + \frac{2}{Re_t} (\text{ALFA} + \text{GAMA})]
\end{aligned} \tag{92}$$

where \* denotes the value of the unknown calculated directly from the difference equation.

Several observations are made concerning the difference equation for  $u_{ij}$  given by Equation 92. The unknowns  $v_{ij}$  and  $p_{ij}$  do not appear explicitly. In fact  $p_{ij}$  does not appear at all. The y component of velocity  $v_{ij}$  does appear implicitly in the quasi-linear coefficients 'VC' and 'VV' as does  $u_{ij}$ . The previous value for  $u_{ij}$  occurs explicitly in the term containing the velocity divergence D. The finite difference linearization assumption requires that the latest prior values for  $u_{ij}$  and  $v_{ij}$  are used in these instances.

In an analogous manner, the y component, transformed momentum equation, Equation 4a, is written for  $v_{ij}^n$  and becomes

$$\begin{aligned}
v_{ij}^* = & v_{ij}^{n-1} + \Delta t [\text{NETA}(p_{i+1} - p_{i-1}) - \text{XXI}(p_{j+1} - p_{j-1}) \\
& + 'VC' (4v_{IC1} - v_{IC2}) + 'VC' (4v_{JC1} - v_{JC2}) - v] \\
& + \frac{1}{Re_t} [\text{ALFA}(v_{i+1} + v_{i-1}) + \text{GAMA}(v_{j+1} + v_{j-1})]
\end{aligned}$$

$$\begin{aligned}
& + \text{BETA}(v_{i+1,j+1} - v_{i+1,j-1} + v_{i-1,j-1} - v_{i-1,j+1}) + \text{UV}(4v_{JV1} - v_{JV2}) \\
& + [\text{VV}(4v_{JV1} - v_{JV2})] / [1 + \Delta t(UC + VC + UV + V)] \\
& + \frac{\tilde{\epsilon}}{\text{Re}_t} (\text{ALFA} + \text{GAMA})
\end{aligned} \tag{93}$$

Again,  $p_{ij}$  does not appear either explicitly or implicitly. The unknown  $u_{ij}$  appears implicitly in the coefficients UC and VC. Also,  $v_{ij}$  occurs implicitly in UC and VC and explicitly in the velocity divergence term. The most current previous values for  $u_{ij}$  and  $v_{ij}$  are used in these lower order coefficients.

The static pressure throughout the flow field is calculated from the Poisson pressure equation, Equation 50, derived in Section II. Second order accurate central differences are used to approximate the second derivatives of pressure in the transformed Laplacian term. The first derivatives of pressure in the Laplacian are approximated by second order accurate upwind differences. The direction is based on the sign of the coefficients C and T which is the same method used for the momentum equations. In this equation, a nonlinear source term occurs which is composed of transformation and velocity derivatives. The transformation derivatives are approximated with second order accurate central differences. Second order accurate upwind differences are used for the velocity derivatives. The direction of the differences at each location is determined by the direction of the local i and j velocity components related to UC and VC previously defined. The time derivative of the velocity divergence is approximated with a first order accurate backward difference. The requirement that the velocity divergence at the nth time step be zero is incorporated into the difference equation by setting  $D^n$  to zero. The numerical

non-zero quantity  $D^{n-1}$  is retained as a correction factor. In this way, the static pressure is found which tends to satisfy mass conservation at every location for each time step.

The following definitions are given for the finite difference representation of the source terms as described above:

$$UX = (y_r u_\xi - y_\xi u_r) / J$$

$$UY = (x_\xi u_r - x_r u_\xi) / J$$

$$VX = (y_r v_\xi - y_\xi v_r) / J$$

$$VY = (x_\xi v_r - x_r v_\xi) / J$$

If these definitions, the previous transformation coefficient definitions, and index conventions are used, the transformed pressure equation, Equation 59, is rearranged for the field static pressure  $p_{ij}^n$  given by

$$\begin{aligned} p_{ij}^n &= -\frac{p_{ij}^{n-1}}{J} + (UV)^2 + 2(VX)(UY) + (VY)^2 + \text{ALFA} (p_{i+1} + p_{i-1}) \\ &\quad + \text{ALFA}(p_{j+1} + p_{j-1}) + \text{BETA}(p_{i+1,j+1} - p_{i+1,j-1} + p_{i-1,j+1} \\ &\quad + p_{i-1,j-1}) + \text{UV}((4p_{IV1} - p_{IV2}) + \text{VV}((4p_{JV1} - p_{JV2})) / 3(\text{UV} \\ &\quad + \text{VV}) + \beta(\text{ALFA} + \text{GAMA}) \end{aligned} \quad (94)$$

In this equation  $p_{ij}$  does not appear implicitly. The velocity components  $u_{ij}$  and  $v_{ij}$  are only present implicitly in the nonlinear source terms.

The three difference equations, Equations 92 thru 94, form a set of equations for the flow variables  $u$ ,  $v$ , and  $p$  at location  $(i, j)$  in terms of the transformation derivatives and values of the variables at neighboring points. The quasi-linearization and differencing methods have decoupled the equations with respect to the higher order terms for the unknowns at location  $(i, j)$ .

The large system of finite difference equations which must be solved for the  $n^{th}$  time step is solved using SOR iteration given by

$$u_{ij}^{(s+1)} = \omega_{uv} u_{ij}^* + (1 - \omega_{uv}) u_{ij}^{(s)} \quad (95a)$$

$$v_{ij}^{(s+1)} = \omega_{uv} v_{ij}^* + (1 - \omega_{uv}) v_{ij}^{(s)} \quad (95b)$$

$$p_{ij}^{(s+1)} = \omega_p p_{ij}^* + (1 - \omega_p) p_{ij}^{(s)} \quad (95c)$$

where  $s$  is the iterate number,  $*$  designates the current value obtained from the difference equation, and  $\omega_{uv}$  and  $\omega_p$  are acceleration parameters. The acceleration parameters are always unity for the first iteration.

The computation of the wall static pressure is carried out separately as discussed in Section II. The pressure iteration technique of Chorin (68), given by Equation 40, avoids the difficulty of formulating one sided differences at the body for the Laplacian of pressure. Also, at the body surface, conservation of mass is directly imposed. Second order accurate upwind differences are used for the transformation and velocity first derivatives in the velocity divergence of Equation 51. The acceleration parameter  $\omega$ , which is related to SOR iteration of the Poisson pressure equation, is given by Hodge (53) as

$$\omega = 2\omega_{pb}/(\Delta t(\text{ALFA} + \text{GAMA})) \quad (66)$$

where  $\omega_{pb}$  is an acceleration parameter for the corresponding SOR iteration of the Poisson pressure equation. For consistency, the iteration equation is repeated as

$$p_b^{(s+1)} = p_b^{(s)} - \frac{\nabla P}{\Delta t} \quad (67)$$

where  $s$  represents the iterate number and the index notation is kept as described above.

The trailing edge pressure on an airfoil can be difficult to obtain using the iteration procedure if a sufficiently fine grid is not present.

Hodge (53) experienced such difficulties in his laminar flow work. The trailing edge pressure can then be calculated using an average of values obtained by linearly extrapolating the pressures calculated at the closest points on the upper and lower surfaces. For a two point linear extrapolation in the  $x$  direction, the pressure at the trailing edge becomes

$$p_1 = \frac{(x_1 - x_3) p_2 - (x_1 - x_2) p_3}{2(x_2 - x_3)} + \frac{(x_1 - x_{IMAX-2}) p_{IMAX-1} - (x_1 - x_{IMAX-1}) p_{IMAX-2}}{2(x_{IMAX-1} - x_{IMAX-2})} \quad (97a)$$

where the  $x$ 's are the  $x$  values at the selected surface points and the surface  $j = 1$  value is understood.

The iteration procedure follows a prescribed order at each point location ( $i, j$ ). Only the body surface pressure is computed on body points. At field points, the  $u$  velocity component is computed first, then the  $v$  velocity component, and finally the field pressure  $p$ . The points are ordered by varying the  $\tau(j)$  index from  $j = 1$  thru  $j = JMAX-1$  on successive  $\tau$  lines in the transformed plane. The  $\tau$  lines  $i = 1$  thru  $i = IMAX-1$  are traversed. Values for the variables at  $i = 1$  are set equal to the values at  $i = IMAX$  to insure continuity across the transformation branch cut. The  $i$  index is adjusted across the branch cut in a manner identical with that described for obtaining the transformation from equations 85 and 86.

### C. Boundary and Initial Conditions

Boundary and initial conditions are formulated for use in the computational plane in order to completely define the numerical problem. Boundary conditions on the body surface are conveniently specified with the body-fitted coordinate system. The first  $\tau$  contour is constructed to be the

body surface. The analytical no slip boundary conditions for velocity given by Equation 52 can be directly applied to the body surface in the computational plane and are given by

$$u_b = 0 \quad v_b = 0 \quad (98)$$

where the subscript b denotes the body surface contour. The surface pressure is calculated as discussed in Section IV.B.

The  $\xi$  lines  $i = 1$  and  $i = IMAX$  in the computational plane define the branch cut in the physical plane. No boundary conditions are required or allowed on these contours. The matching of solutions on these lines, which was described previously, provides a continuous solution across the cut.

The outer boundary in the physical plane frequently represents conditions at infinity (freestream conditions) given by Equations 53 and 54. In the body-fitted coordinate system, the outer boundary becomes the largest  $\xi$  line in the computational plane. The physical outer boundary is chosen to be a circle with a radius of 10 airfoil chords. The distribution of points on the outer boundary is readily specified on a circle; also, the initial input solution for obtaining the transformation as discussed in Section IV.A is simple to specify. Ghia and Hodge (82) applied a numerical inviscid analysis to a Joukowski airfoil at angle of attack using free-stream boundary conditions for different outer boundaries. They found that for a  $10^\circ$  angle of attack the lift coefficient differed by less than one percent and the maximum suction pressure coefficient by about two percent from the analytical result. Navier-Stokes solutions using a circular outer boundary with a smaller radius are compared with the 10 chord radius result to determine effects of boundary placement.

With the outer boundary elected to approximate the far field free-stream, the boundary conditions for velocity and pressure are specified.

As pointed out by Roache (83), caution must be exercised in applying the analytical conditions, Equations 53 and 54, which are strictly valid only in the limit of large distances from the body. If these conditions are used on a boundary at a finite distance away, the result may predict no drag since a wake cannot exist at the outer boundary. This problem is avoided by applying upstream and downstream boundary conditions on the outer boundary. The upstream boundary along which conditions are fixed is defined by the semicircle in the half plane  $x \leq 0$  where the  $x$  axis lies along the airfoil chord with the origin at the midchord. The downstream boundary for which some variables are permitted to be free is the semicircle in the half plane  $x > 0$ .

The upstream boundary conditions for the incoming undisturbed flow become

$$u_{i, JMAX} = \cos \alpha \quad v_{i, JMAX} = \sin \alpha \quad p_{i, JMAX} = 0 \quad (99)$$

where  $i$  ranges over all  $\xi$  contours which terminate on the upstream boundary.

The downstream boundary conditions must allow a wake downstream of a body to pass through the boundary. The no change boundary condition has been widely used (53,83) and meets this requirement. One approach requires no change of the velocity components in the freestream direction. Using the expressions for the directional derivative and gradient in the transformed plane, this boundary condition can be written for the  $u$  component of velocity as

$$u_r = u_z (x_r \sin \alpha - y_r \cos \alpha) / (x_z \sin \alpha - y_z \cos \alpha) \quad (100a)$$

where  $\alpha$  is the geometric angle of attack. Now consider a similar downstream boundary condition where the no change condition is imposed on the velocity components along the downstream  $\xi$  contours. In a similar manner, this condition in the transformed plane becomes

$$u_r = 0 \quad v_r = 0$$

(100b)

This boundary condition is identical with the freestream direction boundary condition of Equation 100a when the  $\xi$  contours are in the freestream direction. In this case,  $\tan \xi = y_r / x_r$ , and Equation 100a becomes identical with Equation 100b. This case does occur in the downstream wake region for the transformation obtained in Section IV.A. Small changes in the velocity components are found in the far wake region of bodies. The downstream far field inviscid flow field also has negligible changes as seen in the analysis of Appendix F. Thus, the no change conditions of Equation 100b approximate the small far field downstream variations in velocity while allowing the momentum defect in a wake to exit at the outer boundary.

The downstream outer boundary condition for pressure must be considered along with the velocity conditions. Hodge (53) investigated the use of a similar no change condition for pressure, namely,  $p_r = 0$  coupled with the velocity conditions of Equation 100b. His laminar solution developed pressure oscillations. The more restrictive condition of specifying the free-stream pressure in the far wake was successfully used by Hodge (53). The specification of pressure recovery with a freely developing velocity defect in the far wake gives a set of numerical boundary conditions which can physically represent the far wake at a finite far field downstream boundary. The downstream pressure boundary condition becomes

$$p_{i, JMAX} = 0 \quad (101)$$

The suitable description of the physics at the downstream computational boundary must be written in finite difference form. The no change condition approximated with a second order accurate central difference applied at the midpoint in the computational plane between the boundary point and first interior point on a downstream  $\xi$  contour ( $i$  index) gives

$$u_{JMAX} = u_{JMAX-1} \quad v_{JMAX} = v_{JMAX-1} \quad (102)$$

for the downstream boundary conditions of the velocity components. An alternate formulation is obtained by approximating the no change condition with a second order accurate upwind difference applied at the boundary point. Then, the downstream boundary conditions for the velocity components become

$$u_{JMAX} = (4u_{JMAX-1} - u_{JMAX-2})/3 \quad (10a)$$

$$v_{JMAX} = (4v_{JMAX-1} - v_{JMAX-2})/3$$

These boundary conditions also follow from a second degree polynomial fit with a zero derivative imposed at the downstream boundary.

The time dependent finite difference method given previously requires a set of initial values for the velocities and pressures at all the ( $i, j$ ) locations. This requirement parallels the result discussed for the differential equations in Section III.b. Two methods are used to provide initial conditions. In the first method, an inviscid solution with circulation for the flow field at the given angle of attack is obtained using SOR iteration as described in Appendix G. This solution then provides initial values for the Navier-Stokes solution. The second technique uses the Navier-Stokes solution for one angle of attack and rotates the velocities by the change in angle of attack. The set of initial values for velocity and pressure is then used to start a Navier-Stokes solution at the new angle of attack.

#### D. Turbulence Model

The numerical procedure which implements the eddy viscosity turbulence model described in Section III is discussed. The two layer model near the airfoil surface is presented followed by the far wake model. The procedure used in the near wake is then described. The eddy viscosity distribution throughout the flow field is calculated at the beginning of each time step.

SOR iteration is then used to determine the velocities and pressures at the new time level. The eddy viscosity distribution is not changed during the iteration process.

The inner viscosity computation from Equation 60 requires values of the tangential and normal velocity derivatives and the distance from the surface. These velocity derivatives are given by Equations 70 and 71 in the transformed plane. They are evaluated using second order accurate central differences for both the transformation derivatives and the u and v velocity component derivatives with respect to  $\xi$  and  $\eta$ . The inner eddy viscosity is identically zero at the surface ( $\zeta=1$ ) and need not be calculated separately. The corresponding velocity expression which is found in the exponent of the damping factor, Equation 62, must be evaluated at the airfoil surface for each  $\xi$  contour in regions of turbulence. The derivatives with respect to  $\tau$  are approximated by second order accurate forward differences found in Appendix B, and the derivatives with respect to  $\xi$  are evaluated using second order accurate central differences. The distance from the surface to the point (i, j) is measured along the constant  $\xi$  line represented by index i. The freestream chord Reynolds number appears throughout the model as a result of writing the equations in nondimensional form and is an input parameter.

The adverse pressure gradient turbulence model modification in the trailing edge region given by Equation 65 is implemented next. The origin of the distance s, measured along the airfoil surface from the trailing edge separation point, is determined by examining the u velocity component at point on the  $\xi$  contour next to the surface ( $j=2$ ). The search begins on the  $\xi_1$  line, corresponding to the 95 percent chord location and advances toward the airfoil leading edge along the second  $\xi$  line. The search terminates when a positive value for  $u_{i2}$  is detected with infinite attached flow. The relaxation factor

$f$  is then evaluated for each applicable  $\gamma$  line where trailing edge separation is detected. The inner eddy viscosity is multiplied by the relaxation factor which adjusts the adverse pressure gradient inner eddy viscosity constant  $k_1$ .

After the inner eddy viscosity is computed, the limiting technique evaluates the computed value. The inner eddy viscosity is prevented from decreasing in the outward normal and downstream tangential flow directions by comparing the value with previously computed values as given by the following sequence:

$$\gamma_{ij} \leftarrow \gamma_{i,j-1} \quad \text{and} \quad \gamma_{ij} \leftarrow \gamma_{i-1,j}$$

The larger value is selected during each comparison. The initial inner eddy viscosity limiting distribution is calculated in the attached boundary layer region with a favorable pressure gradient near the airfoil leading edge. The first or outward direction limiting condition is imposed here as well.

The limit value of the inner eddy viscosity is then compared with the calculated outer layer eddy viscosity. Whenever the inner eddy viscosity first exceeds the outer value, the outer eddy viscosity is then used for the remaining locations outward from the surface. This switch insures the continuity of the eddy viscosity distribution.

The computation of the outer eddy viscosity given by Equation 61 requires values for the local boundary layer edge velocity and the displacement thickness defined by Equation 64. These quantities are calculated for each  $\gamma$  contour which crosses the turbulent boundary layer. For a  $\gamma$  line, the local edge velocity  $u_e$  is defined to be the maximum tangential velocity measured relative to the local surface tangent line. The tangential velocity is given by Equation 68 and is evaluated as described previously for the inner eddy viscosity. The boundary layer thickness  $\delta$  is then the distance along the  $\gamma$  line from the surface to the first point where the tangential velocity is at

less than 0.99  $u_e$ . The displacement thickness is calculated using trapezoidal integration where the limits of integration are determined by the computed boundary layer thickness.

The resulting eddy viscosity distribution is next modified to simulate the transition from laminar to fully turbulent flow. The transition factor  $\beta$ , given by Equation 67, is calculated as follows. The starting location for transition on the airfoil surface must be specified. This location is specified by designating the first grid point on the surface downstream as well as the distance to that first grid point  $x_s$ . The transition distance  $s$  from the starting location to a given  $\gamma$  line is calculated by adding  $x_s$  to the distance between the successive surface grid points with known locations. The relaxation factor  $\beta$  is determined from the transition factor Equation 67 and the definition of  $\beta$ . If  $\beta = 3/4$  is specified when the transition distance equals three fourths of the total transition length, then  $1/\beta$  is given by

$$1/\beta = 2.4456/x_L \quad (104)$$

where  $x_L$  is the total assumed transition length. The eddy viscosity distribution computed previously on a  $\gamma$  line is multiplied by the corresponding constant  $\beta$  to obtain the revised distribution of turbulent eddy viscosity which includes the transition region.

The final modification made to the eddy viscosity distribution across the upper surface turbulent region involves the decrease of turbulence in the direction from the boundary layer toward the far field. The intermittency factor given by Equation 63 models this behavior. The previously calculated boundary layer thickness  $\delta$  and the distance from the airfoil surface to the  $(i, j)$  location on a  $\gamma$  line are used to compute the intermittency  $\alpha$  for that location. The previous values of the outer eddy viscosity are multiplied by the corresponding value of the intermittency factor to obtain the final eddy

viscosity distribution for the turbulent region above the airfoil surface at the  $n^{\text{th}}$  time step.

The procedure for computing the eddy viscosity distribution on a  $\gamma$  line across the turbulent flow zone above the airfoil is repeated downstream for each  $\gamma$  line through the 95 percent chord point. The  $\gamma$  contours near the trailing edge deviate from the local normal direction in excess of  $10^{\circ}$ . For locations in this small region, the eddy viscosity is found by using the last calculated value upstream in a direction tangent to the airfoil surface.

The calculation of the far wake eddy viscosity given by Equation 73 is similar to the computation of the outer layer eddy viscosity. In the wake region the  $\gamma$  contours are approximately orthogonal to the flow direction in the wake. The  $\gamma$  contours are thus conveniently defined paths across the wake for use in computing wake characteristics.

On an  $\gamma$  contour, the component of velocity in the freestream direction is computed for the grid points spanning the wake. The minimum of these directional velocity components in the wake is determined. The maximum values of the velocity components which occur on either side of the minimum value are found and designated the upper and lower edge velocities. Then the upper and lower edges of the wake are defined as the points where the local velocity component in the freestream direction first reaches 90 percent of the upper and lower edge velocities, respectively. The distances from the point of minimum velocity to the upper and lower wake edges are defined as the upper and lower wake thicknesses, respectively. These distances determine the limits of integration when calculating the upper and lower wake displacement thicknesses from Equation 64. The origin of the variable of integration is at the grid point where the minimum velocity occurs. The upper and lower wake displacement thicknesses are numerically evaluated with

trapezoidal integration. The half wake displacement thickness  $\frac{h_w}{2}$  is the average of the upper and lower displacement thicknesses. The far wake eddy viscosity is calculated from Equation 73 using the thickness  $\frac{h_w}{2}$  and an average of the upper and lower edge velocities.

The intermittency factor for each grid point on an ' contour is determined using the average value of the upper and lower wake thicknesses for ' in Equation 63. The local distance to each point is calculated from the location of minimum velocity along the ' contour.

The near wake model is numerically implemented by considering the upper turbulent and lower laminar boundary layers separately. The eddy viscosity distribution, which is calculated near the trailing edge of the airfoil at the 95 percent chord location, is extended into the near wake along a direction parallel to the airfoil surface defined by the 95 percent chord and 99 percent chord grid point locations. The chord line is the line of extension for the boundary layers in the near wake. The ' lines  $i = 1$  and  $i = I_{MAX}-1$  define the interaction zone in the near wake. The non-interacting distance  $WL_1$  in Equation 74 is based on the length of the lower laminar boundary layer thickness computed at the 95 percent chord location. This boundary layer thickness is computed by the same method used previously for the upper surface boundary layer. The distance  $WL_2$  along the chord line from the trailing edge to the location where the far wake eddy viscosity model begins is also calculated as a multiple of the laminar trailing edge boundary layer thickness. The eddy viscosity in the interaction zone is computed with the two calculated distances and the far wake eddy viscosity using Equation 74.

#### E. Force Coefficients

The forces and moments exerted on the airfoil body by the flow field are evaluated at the body surface using Equations 79, 80, and 81. The

integrals are evaluated using trapezoidal integration. The product terms in the integrands of the form  $(fg)$  are integrated by using products of averages,  $(f_i + f_{i+1})(g_j + g_{j+1})/4$ . The  $\tau$  derivatives are evaluated using second order accurate central differences, and the  $\tau'$  derivatives are formulated with second order accurate upwind forward differences. The lift and drag coefficients are calculated by adding the components of  $x$  and  $y$  direction force coefficients in the normal freestream (90 degrees counterclockwise) and freestream directions, respectively, using Equations D.13 and D.14.

The alternate technique based on the control volume analysis in Appendix D for computing the forces on the airfoil body is numerically implemented in a similar manner. The force coefficients in the  $x$  and  $y$  directions for a two-dimensional control volume defined by an  $\tau$  line are given by Equations 83 and 84, respectively. The line integrals are again computed with trapezoidal integration using products of averages. The  $\tau$  derivatives are evaluated with second order accurate central differences. The  $\tau'$  derivatives are evaluated with second order accurate central differences on the interior  $\tau'$  lines. Second order accurate upwind differences are used to approximate the  $\tau'$  derivatives on the body and outer boundary  $\tau$  lines. The area integral is also evaluated using trapezoidal integration. The Jacobian for an area element bounded by the  $i$  and  $i+1$   $\tau$  lines and  $j-1$  and  $j$   $\tau'$  lines is calculated by taking the average of the Jacobian values previously computed for the viscous term in the line integrals at the corresponding  $\tau$  segments on the  $j-1$  and  $j$   $\tau'$  lines. The area integrals are computed for both  $n$  and  $n-1$  time intervals using the previously computed flow field values. The time derivative is then evaluated using a first order accurate backward difference.

## SECTION V

### DISCUSSION OF RESULTS

Numerical solutions for two-dimensional incompressible turbulent viscous flow over a NACA 0012 airfoil section are obtained using the implicit finite difference method previously described. The NACA 0012 airfoil section is chosen because of its widespread use as a test case in both experimental and computational work (65,66). The solutions are for angles of attack of 5°, 7.5°, 9.5°, and 11.5° at a chord Reynolds number of 170,000. This Reynolds number is selected for comparison with both previous NACA data (5e) and for data obtained as part of this investigation at the Air Force F. J. Seiler Research Laboratory (84).

The numerically generated body-fitted coordinate system which was used for each solution is presented. The successive-over-relaxation (SOR) iteration numerical parameters and convergence criteria along with the steady state convergence criteria are then discussed. The velocity and pressure fields and streamline contours obtained from the numerical solutions are examined. The calculated laminar separation bubble characteristics are compared with empirical results. The position of transition to turbulence and the transition length relative to the separation bubble location are discussed. The computed airfoil surface mean pressure distributions are compared with both an inviscid solution and experimental data. The numerically predicted lift and drag forces exerted by the flow field on the airfoil are presented along with available experimental measurements. The effects that the placement and type of imposed far field boundary conditions have on the numerical solution are discussed. The sensitivity of the numerical solution to grid size is examined.

The curvilinear body-fitted grid shown in Figure 3 is numerically generated using boundary layer parameters for the attraction of contours towards the airfoil surface and linear interpolation for wake resolution given by Appendix C. The Blasius series flat plate chord Reynolds number of 200,000, a nondimensionalized boundary layer edge velocity of 1.2, and seven grid points specified in the boundary layer are used in the contour attraction technique (7). The distribution of airfoil surface points is accomplished with Equation 26 where  $A_1 = 0.6$ ,  $A_2 = 0.4$ , and  $A_3 = 1.0$ . Seventy-one  $\xi$  or surface points together with forty-four  $\tau$  contours are used. The transformation difference equations, Equations 85 and 86, were then solved using SOR iteration. The optimum local acceleration parameters varied between 0.8 and 1.5 throughout the flow field with essentially no change in the local values after 25 iterations. After 350 iterations, the maximum errors in the solution for both  $x$  and  $y$  were less than  $10^{-4}$ , and occurred near the outer boundary above the airfoil. Additional  $\xi$  lines were added in the airfoil wake region using the interpolation method described in Appendix C. Eight grid points (four at a time) were inserted on the rounded trailing edge. Table C.1 gives the  $\xi$  and  $\tau$  indexing for the final 79x44 grid shown in Figure 3 and the equivalent indices for the 71x44 original grid.

The airfoil is thus defined by a total of 79 points. Eleven grid points define the first 5% chord nose region and 17 points are used to define the rounded trailing edge. The maximum distance between successive surface grid points is 5% of the chord. The  $\xi$  lines intersect the surface contour within 10° of the local normal direction except in the last 5% chord region near the trailing edge.

The SOR iteration parameters and convergence criteria which are required by the numerical implicit procedure are similar for each angle of attack

solution. The acceleration parameters had values of 1.0 for the velocity components, 0.9 for the surface pressure, and 1.10 or 1.15 for field pressures. The larger value of  $\omega_p$  was used at  $9.5^\circ$  and  $11.5^\circ$  angles of attack. The convergence criteria for the SOR iteration required that the maximum change in the relative magnitudes of  $u$ ,  $v$ , and  $p$  for all locations be less than 1%. This criteria was relaxed to 5% for the  $9.5^\circ$  and  $11.5^\circ$  cases. Three iterations per time step were the maximum necessary during most of each computed case. For the  $9.5^\circ$  case, the approach to the steady state solution was re-run with  $\omega_{pb} = 0.95$  and  $\omega_p = 1.10$  for two characteristic times. An additional iteration per time step was required to maintain the same error tolerance. Computed values of lift and drag were virtually identical.

Although implicit SOR methods have been shown by linear stability analyses to be unconditionally stable, convergence at a given time required a small time step  $\Delta t < 0.001$ . The analysis in Appendix E based on linear matrix theory indicates that the diagonal dominance of the set of finite difference equations given by Equations 92 and 93 has a definite dependence on  $1/\Delta t$ . Diagonal dominance is a necessary and sufficient condition for convergence (81) of constant coefficient linear systems using SOR iteration. Although this system of equations has lower order nonlinearities and variable coefficients, the order of magnitude study of Appendix E indicates convergence if the most stringent requirement  $\Delta t \leq 0.0003$  is applied. A constant time step equal to 0.0005 was used for each solution. No convergence problems were encountered.

The finite difference method described in Section IV is a time dependent technique. The solution is advanced in time by  $\Delta t$  increments. The numerical solution was considered to have reached a steady state when changes in the computed values of the lift and drag coefficients were less than 1% over one characteristic or nondimensional time period. Each steady

state solution required three to six characteristic time periods and from two to four hours of CPU time on a CDC CYBER 750 computer.

The numerical solution of the mean flow field near the airfoil section at each angle of attack is presented by using streamline contours, velocity field vectors, and pressure contours. The mean streamline contours are shown in Figures 4 through 7. A small laminar separation bubble on the upper surface with negligible trailing edge separation is seen in Figure 4 for  $\alpha = 5^\circ$ . For an increased angle of attack equal to  $7.5^\circ$ , the separation bubble has decreased in size and moved forward toward the leading edge of the airfoil. Figure 5 also shows the turbulent trailing edge separation region which has also moved forward. The trailing edge separation region has grown significantly and has progressed to the quarter chord position when the angle of attack has reached  $11.5^\circ$ . This behavior is typically observed during trailing edge stall (72).

The velocity field vector plots presented in Figures 8 through 11 also illustrate the phenomena discussed above. In addition, a small scale clockwise rotational motion is observed in the rear portion of the trailing edge separation region. A circulatory flow pattern within the laminar separation bubble is seen for  $\alpha = 5^\circ$  in Figure 8. The boundary layer near the leading edge for each angle of attack contains at least five grid points along each  $\delta$  contour while approximately ten points resolve the lower surface laminar boundary layer near the trailing edge. This number of points should be sufficient to resolve the primary features. The pressure contours near the airfoil in Figures 12 through 15 clearly show expanding regions of low pressure above the airfoil and high pressure below the airfoil as the angle of attack increases. The large pressure variations in the upper surface suction peaks are also observed. The pressure field indicate that only small pressure variations occur in the wake for each angle of attack. The smooth and continuous numerical solution for the

pressure field is in sharp contrast to the large oscillatory results obtained by Hodge (7) for laminar flow.

For a moderately thick airfoil with a smooth surface in a flow with a low freestream turbulence intensity, the laminar boundary layer near the leading edge can separate upon encountering a strong adverse pressure gradient. Subsequently, shear layer instabilities can cause transition to turbulence. The increased mixing may reattach the shear layer and thereby form a separation bubble. The formation of separation bubbles and their relationship with the stalling characteristics of airfoils at various Reynolds numbers have been investigated by Gault (85), Gaster (86), Hoad, et al (87), and Arena and Mueller (88). The laminar separation bubble has been observed experimentally by Gregory and O'Reilly (89) for the NACA 0012 airfoil over a large range of Reynolds numbers. These experimental and empirical results will be used to compare with the numerical solutions.

In this investigation, the beginning of turbulent transition on the upper surface of the airfoil and the transition length have been based on the closure of the laminar separating shear layer. The surface mean pressure coefficients for  $\alpha = 5^\circ$  and  $7.5^\circ$  presented in Figures 16 and 17 clearly show the laminar bubble constant pressure region, downstream of the suction peak, followed by a rapid recovery. Transition in the numerical solution occurs near the downstream side of the bubble where the steep pressure recovery begins. This phenomenon has been reported by Wallis (90) and Arena and Mueller (88). The chord locations for the start of transition  $x_t$  and full turbulence  $x_T$ , relative to the separation and reattachment points of the bubble,  $x_S$  and  $x_R$  respectively, are given in Table I. For the smaller angles of attack, reattachment occurred prior to attaining fully turbulent flow. This behavior has been experimentally observed by Arena and Mueller (88) in their low Reynolds

TABLE I Computed Characteristics of Turbulence Near  
The Airfoil Leading Edge ( $x = -0.5$ )

$\alpha$ (Deg)	$x_S$	$x_t$	$x_R$	$x_T$
5.0	- 0.42	- 0.24	- 0.15	- 0.09
7.5	- 0.47	- 0.42	- 0.38	- 0.35
9.5	-	- 0.48	-	- 0.46
11.5	-	- 0.49	-	- 0.48

TABLE II Computed Laminar Separation Bubble Characteristics

$\alpha$ (Deg)	$M_S$	$H_{12S}$	$Re_{\xi^*S}$	$Re_{LS}$	$\xi_S^*$	$L_B$	$L_R$
5	.124	3.1	680	220	.0025	.27	-.002
7.5	.091	3.2	540	168	.0013	.09	-.002

number flow study.

The computed values of several parameters at separation for both  $\alpha = 5^\circ$  and  $\alpha = 7.5^\circ$  cases agree with empirical results and are presented in Table II. The pressure gradient parameter  $M = - \frac{1}{\delta} \text{Re}_e \frac{du_e}{ds}$  in nondimensional variables, where  $\delta$  is the momentum thickness and  $s$  is arclength, compares favorably with the laminar separation criteria of Curle and Skan (91) given by  $M \geq 0.09$ . The shape parameter  $H_{12} = \xi^*/\delta$  takes on values of 3.1 and 3.2 at laminar separation compared with an average value of 3.5 reported by Curle and Skan. The Reynolds number at separation based on the displacement thickness ( $\text{Re}_{\delta_S}$ ) has a value greater than 500 and predicts a short bubble using the Owen-Klanfer (62) criteria confirmed by Gault (85) and Crabtree (93). The bubble length  $L_B$  is of the order  $10^2 \delta_S$  and decreases rapidly with increased angle of attack as seen in Table II. This relationship also indicates a short bubble (90, 93) whereas long bubbles have lengths of the order  $10^4 \delta_S$  (85,86). The assumption that laminar separation precedes turbulent transition is verified with the computed Reynolds number at separation based on momentum thickness  $\text{Re}_S$ . Crabtree's (94) criteria indicates that transition has occurred if  $\text{Re}_S > 780$  when  $M_S$  first reaches 0.09. Thus, the solutions correctly predict that laminar separation occurs before transition to turbulence. The turbulent reattachment criterion for the bubble given by Roberts (65) is  $C = (C/\text{Re}_e) \frac{du_e}{ds} \geq -0.0059$ . This criterion is also satisfied as shown in Table II.

The trends discussed above for  $M_S$ ,  $L_B$ , and both boundary layer Reynolds numbers continue at the higher angles of attack. However, at angles of attack near stall the bubble length decreases to about 1% chord (60) which is the order of the % contour spacing near the leading edge. The numerical solutions at  $\alpha = 9.5^\circ$  and  $\alpha = 11.5^\circ$  consequently do not resolve the bubble, as

seen in Figures 18 and 19. The solutions become very sensitive to small changes in the turbulent transition length  $x_L$  and starting location  $x_t$ . For example, at  $\alpha = 9.5^\circ$  with an initial transition location of  $x_t = \sim 0.48$ , a change in transition length from 0.022 to 0.025 produced shedding of bubbles, large pressure oscillations, and a significant 30% increase in average drag compared with the steady state solution. The experimental pressure data were measured with diaphragm transducers capable of measuring frequencies well beyond 5000 Hz. No dominant frequency was observed. Head, et al (87) recently observed a small scale unsteadiness in a short region near the surface of a NACA 0012 airfoil at angle of attack. The laser velocimeter mean velocity histograms for a certain region near the leading edge exhibited dominant and small secondary mean velocities. Head, et al suggest that this behavior may indicate an unsteadiness within the laminar separation bubble. The remaining flow field, however, was steady.

The numerical solutions presented for each angle of attack are the result of a parametric study where the upper surface transition length and location were varied in order to close the bubble and maintain steady flow. In each case, a further increase in the transition length or movement downstream of the start of transition resulted in a non-physical oscillatory motion propagated downstream with an accompanied large increase in drag. The good agreement between the calculated and empirical separation bubble characteristics indicates that the origin of turbulence on the upper surface is satisfactorily modelled.

Computed boundary layer velocity profiles at four stations on the upper surface are compared with two sets of hot wire anemometry data (84) in Figures 20 through 23. The profiles were measured and computed at the same locations on constant  $\beta$  lines located approximately at 18%, 50%, 69%, and 92% chord. The profiles are nondimensionalized by the locally computed boundary layer thickness which is defined as the normal distance from the

surface to where the tangential velocity first attains 99% of the local edge velocity. Significant RMS fluctuations for each angle of attack were detected experimentally at the inner data point locations for stations two through four which indicate the presence of a turbulent boundary layer. No fluctuations were observed in the lower surface boundary layer at the 90% chord location. This result provides experimental evidence for the assumption that the lower surface boundary layer remains laminar in the presence of the favorable pressure gradient at the Reynolds number under investigation. The calculated boundary layer becomes thicker downstream compared with the experimental profiles. This result could be caused by grid boundary layer resolution errors propagated downstream or by deficiencies in the turbulence model. The hot wire data have an estimated experimental error of 5%.

The boundary layers on the upper and lower surfaces merge to form the wake downstream of the airfoil. Wake mean velocity profiles at chord locations of 0.58, 0.79, and 1.54 for each angle of attack are shown in Figures 24 through 27. The trailing edge is located at  $x = 0.5$ . The profiles are measured along constant  $\gamma$  lines with the origin on the extended chordline. The thicker numerical upper surface boundary layer propagates downstream. The computed large variations of velocity near the lower edge of the wake, which come from the lower surface boundary layer, are in good agreement with the hot wire anemometry measurements. The measurements were obtained at grid points using the original 71x44 grid while the numerical solutions were obtained from the 79x44 grid system described previously. The computed values of the wake displacement and momentum thickness approach approximately constant values within 15% of each other at a location of one chord downstream of the trailing edge. They were computed using second order accurate trapezoidal integration and are given in Table III.

TABLE III: Computed Far Wake Characteristics

$\alpha$ (Deg)	$\frac{w}{w}$	$w$
5.0	0.011	0.010
7.5	0.019	0.017
9.5	0.028	0.026
11.5	0.038	0.035

The Reynolds stress  $uv^T$ , nondimensionalized by  $w^2$ , was computed and contour plots are shown in Figures 28 through 31. The geometric pattern is qualitatively similar to the experimental data obtained by Coles and Wadcock (96) for a NACA 4412 airfoil which are shown in Figure 32. Some experimental measurements were made during the hot wire anemometry study (84) and are presented in Appendix H. This data also illustrates the rapid variation of negative and positive stresses in the upper and lower portions of the near wake, respectively. Magnitude of the order 0.01 have been observed (84, 96) in the near wake and were also obtained numerically where the contour values vary from -0.01 to +0.01 in Figures 28 through 31.

The computed surface mean pressure distributions for all four angles of attack, presented in Figures 16 through 19, favorably compare with the experimental data (84) which have an estimated error of 5 to 8%. An inviscid solution with imposed Kutta condition was computed using the approach outlined in Appendix G and is also shown. The computed Navier-Stokes laminar suction peak is well defined and increases rapidly with angle of attack. The lower surface pressure peak both moves downstream and becomes broader as the angle of attack increases. This behavior is also seen in the experimental data. A separation bubble is observed in the experimental data where the curvature rapidly changes. The bubble occurs further downstream when compared with the Navier-Stokes computation. This difference is probably caused by free-stream turbulence which can delay separation and the subsequent formation of the bubble. The experimental

data were measured in a wind tunnel with a freestream turbulence intensity of approximately 0.5% compared with the unperturbed freestream of the numerical solution. Some disagreement occurs in the trailing edge region where the computed result has a more pronounced flat trailing edge stall characteristic.

The computed inviscid surface pressure distribution consistently predicts both a larger suction peak on the upper surface and a larger pressure peak on the lower surface. The discrepancies increase with angle of attack. The inviscid solutions predict complete recovery at the trailing edge with a stagnation point and  $C_p = 1.0$ . The large pressure gradients in the inviscid and viscous solutions near the airfoil nose are resolved which indicates an adequate grid point distribution in the region.

An examination of the experimental and inviscid surface pressure distributions for zero angle of attack given in Figure 33 provides additional information. The inviscid pressure distributions, obtained with the SOR finite difference technique in Appendix C, for the upper and lower surfaces are indistinguishable. This physically correct symmetric result came directly from the numerical solution and was not specified as a boundary condition. Furthermore, the numerical inviscid result is virtually identical with an inviscid solution (67) using the method of Theodorsen (12). The experimental data for both surfaces agree well with the inviscid results which indicates the small effect that viscosity has on the pressure distribution for a streamlined symmetric airfoil at zero angle of attack. This agreement also provides evidence that the experimental airfoil section does approximate the NACA 0012 configuration. Viscous effects on the pressure distribution do occur (as was previously mentioned) as the angle of attack is increased even for small  $\alpha$ . A comparison between the experimental data for the two surfaces

reveals a slight suction peak on the lower surface. The suction peak suggests that the experimental zero angle of attack may actually be slightly negative. A small deviation in angle is plausible since the experimental zero was determined by manually adjusting the airfoil attitude until the pressure distributions on both surfaces appeared identical.

The lift coefficients obtained from the present turbulent Navier-Stokes solution, inviscid results, and two sets of experimental data are compared in Figure 34. The experimental results shown have been corrected for angle of attack. The effective experimental zero angle of attack for a symmetric airfoil section is defined to be the angle where the lift coefficient is zero. For the Seiler Laboratory results (54), the effective zero was found to be  $0.5^\circ$ . This small correction is in accord with the analysis of the nominal zero angle of attack pressure distribution results already presented. The experimental data have therefore been translated  $0.5^\circ$  in the negative  $\alpha$  direction in Figure 34. The NACA results (56) were similarly published in corrected form. Other common two-dimensional wind tunnel corrections including solid blocking, wake blocking, and streamline curvature effects were investigated. Empirical low-speed wind tunnel correction factors (57) using the Seiler Laboratory 2'x3' tunnel geometry were applied to the experimental data at  $11.5\%$  to account for blockage and wall interference. The corrected value for the lift coefficient and angle of attack became  $9.5^\circ$  of the uncorrected lift coefficient and  $+0.1^\circ$ , respectively. Neither data set shown in Figure 34 have been so corrected and the curves are null.

The two sets of experimental data contain some conflicts. The NACA data (56) maintain an approximately linear behavior over a wider range of angles of attack when compared with the more recent data (54).

AD-A100 824 AIR FORCE INST OF TECH WRIGHT-PATTERSON AFB OH SCHOO--ETC F/6 20/4  
THE NUMERICAL SOLUTION OF INCOMPRESSIBLE TURBULENT FLOW OVER AI--ETC(U  
FEB 81 H A HEGNA.  
UNCLASSIFIED AFIT/DS/AA/81-1 NL

2 of 2  
AFIT/DS/AA/81-1

END  
DATE FILMED  
7-81  
DTIC

The NACA lift curve then flattens more rapidly near stall. These minor differences may be explained by a larger freestream turbulence level in the NACA results which tends to delay the turbulent trailing edge separation. Also, the major variation of the lift curve at small angles of attack occurs for Reynolds numbers less than  $10^6$  (56, 89). Freestream turbulence can cause more rapid transition and result in an apparent freestream Reynolds number greater than the nominal turbulence-free value.

The computed turbulent Navier-Stokes lift coefficients for the four angle of attack cases are in excellent agreement with the experimental data as shown in Figure 34. The force components were computed using trapezoidal integration to sum the total surface stresses obtained from the flow field solution. The numerical results exhibit a gradual decrease in slope with increased angle of attack similar to the Seiler Laboratory data. This behavior is consistent with the data because the numerical solution has a quiescent incoming freestream with a corresponding smaller apparent Reynolds number. The significant effect that the viscous separation in the trailing edge region has on the lift coefficient for angles of attack greater than  $8^\circ$  is observed. The computed values are within 5% of the experimental results. The lift coefficient was also computed for each angle of attack using the contour momentum integral method described in Appendix D. The calculated values differ by less than 1% for n contour paths within one-half chord of the airfoil surface. This result demonstrates the near flow field consistency in resolving the lift force. The time dependent terms in Equations 83 and 84 always contributed less than 0.5% of the total computed lift which indicates again a converged steady solution.

Two inviscid flow predictions for the lift coefficient are shown in Figure 34 for comparison. The numerical inviscid finite difference results were computed with the second order accurate trapezoidal integration

technique used in the viscous calculations. The linear airfoil theory  $2\pi$  slope is included. The inviscid flow results over-estimate lift by 25% at an angle of attack of  $5^\circ$ . This discrepancy increases with angle of attack because the viscous effects which induce stall are not present in an inviscid calculation.

The computed drag coefficients for the four cases are compared with available experimental data (56) in Figure 35. The force components were computed using trapezoidal integration to sum the total surface stresses obtained from the flow field solution. The drag component is in the direction of the incoming freestream flow. The rapid increase in the drag coefficient which accompanies the smaller increase in lift at higher angles of attack near stall is observed. Jacobs and Sherman (56) acknowledged that the experimental drag data in this Reynolds number region have error greater than the estimated  $\pm 0.001$  for the larger Reynolds number results. The agreement between the present numerical solution and the experimental data is within ten drag counts in the region of the maximum lift to drag ratio.

The presented numerical solutions for two-dimensional incompressible turbulent viscous flow over airfoils were obtained with several parametric studies. The effects associated with varying the turbulence transition values and the SOR iteration parameters including time step size have already been discussed. The influence of other turbulence model parameters, far field boundary conditions, and grid fineness on the numerical solutions have also been investigated.

The turbulence model contains several parameters which can vary. The effects that changes in these parameters have on the flow field near the airfoil surface and on the values of lift and drag were examined. The value of the nominal inner eddy viscosity parameter  $k_1$  was increased by 20% at a  $5^\circ$  angle of attack. The lift coefficient subsequently increased by 2%

while the drag coefficient increased by 5% or six drag counts. These integrated effects are caused by the observed small increase of velocity in the inner boundary layer on the upper surface. The outer eddy viscosity parameter  $k_2$  was next increased by 50%. The result was an increase in turbulent mixing with a corresponding thicker boundary layer. The velocities near the edge of the upper surface boundary layer decreased which caused an 8% loss of lift with no apparent effect on the calculated drag.

Values for the constants in the inner eddy viscosity parameter  $k_1$  relaxation factor given by Equation 65 were obtained from a parametric study at an angle of attack of  $11.5^\circ$ . This angle of attack was chosen because the effects of the relaxation are significant only for angles of attack near stall. A solution was initially computed without the relaxation factor  $f$ . The laminar separation bubble remained closed with trailing edge separation beginning at mid-chord. The calculated values for the lift and drag coefficients were 0.98 and 0.064, respectively. An examination of the lift curve in Figure 34 reveals that this solution exhibits the character of leading edge stall where an approximate linear behavior is sustained until separation abruptly occurs. Leading edge stall does occur for the NACA 0012 airfoil for Reynolds numbers greater than about 500,000 (56, 89). Thus the mechanism for leading edge stall seems present within the modified turbulence model. A numerical solution was next obtained using the relaxation factor with a relaxation distance  $s_r = 0.25$  and a delay distance  $s_d = 0$ . in nondimensional distances. The laminar bubble remain closed, but the trailing edge separation region was significantly larger and moved to within the 20% chord location ( $x = -0.3$ ). The lift coefficient decreased substantially to a value of 0.8 while the drag coefficient increased moderately to a value of 0.074. The final solution

which has been previously discussed was calculated using distances  $s_r = 0.5$  and  $s_d = 0.1$ . The computed lift and drag coefficients became 0.84 and 0.068, respectively, and are in agreement with the experimental data. The sensitivity of the numerical solution to these parameters has thus been obtained. The last set of distance parameters was used in calculating the solutions for the other angles of attack. The onset of trailing edge separation for the  $5^\circ$  and  $7.5^\circ$  solutions, seen in Figures 4 and 5, indicates that the relaxation factor was not activated. Thus the relaxation model for parameter  $k_1$  affects the flow field only near stall where the pressure gradient approaches zero over a large portion of the upper surface.

The relaxation distance  $WL_2$  in the near wake turbulence model given by Equation 74 was also investigated. Numerical solutions were obtained at  $5^\circ$  angle of attack for relaxation distances equal to 5 and 100 times the lower surface boundary layer thickness near the trailing edge. No changes in either the surface pressure distribution or the integrated force coefficients were observed. In two recent near wake calculations with similar relaxation models, Waskiewicz (98) used a value of 30 trailing edge boundary layer thicknesses and Hasen (99) used 10 boundary layer thicknesses. The relaxation distance of 5 boundary layer thicknesses was retained since the agreement of the Reynolds stress field discussed previously was improved for this choice.

The effect on the solution of the placement and type of far field boundary conditions should be considered in any computational work. In this investigation, two types of boundary conditions at different locations were examined. The four angle of attack solutions that have been discussed were computed using the freestream far field boundary conditions described in Sections III.B and IV.C at a circular outer boundary of radius 10 chords. The effect of the far field boundary placement on an inviscid

solution for Joukowski airfoils was previously accomplished (82). This analysis indicated that a radius of 10 chords was sufficient as discussed in Section IV.C. The effect of the boundary placement on the present viscous solution was examined by using an alternate outer boundary. The  $J = 40$  contour with a semi-major x axis of 4.77 and semi-minor y axis of 4.64 was chosen as the new outer boundary because it approximates a circle with half the previous radius. The numerical solution was then obtained for  $\alpha = 5^\circ$  and compared with the solution using the 10 chord radius outer boundary. The average values for the lift and drag coefficients were identical. The solution with the closer far field boundary had a small oscillatory behavior with variations in the lift and drag coefficients of 1% and 2%, respectively. Further examination of the near surface flow field revealed that the laminar separation bubble had a small scale unsteadiness which locally affected the pressure field.

The far field potential flow boundary condition model developed in Appendix F was next applied with the outer boundary locations of 10 chords and about 5 chords in turn. This model approximates the small perturbations from the freestream conditions for the velocity and pressure fields at a large but finite distance caused by the presence of a body in the flow field. In this approach, the upstream boundary conditions for both velocity and pressure became the calculated values from the inviscid potential flow model. The downstream boundary condition for pressure also became the corrected value rather than the freestream value. The no change downstream boundary condition for the velocity components was retained. The solution was calculated with the revised far field boundary conditions at the 10 chord radius circular outer boundary. The boundary conditions were initially updated every 200 time steps ( $0.2T$ ) by using the latest calculated value of the circulation. After three characteristic

time periods  $T$ , the mean values of the lift and drag coefficients were virtually identical with the previous freestream boundary condition results. However, while the lift coefficient had variations of less than 1% from the mean value, the calculated drag coefficient was periodic with a period of  $0.4T$  and variations of  $\pm 10\%$ . Since the period of the oscillations was twice the period of the boundary condition update and the circulation was essentially a constant at this time, the outer boundary conditions (except the no change downstream condition) were kept at the current values and the solution was advanced 1.5 characteristic time periods. At this time, the lift coefficient had a steady value of 0.425 and the drag coefficient became  $0.011 \pm 2\%$  (two drag counts). These computed results are within 1% of the corresponding coefficients calculated from the solution using the simple freestream conditions. Thus the more accurate boundary condition which includes the effect of a finite distance from the body induces very small changes in the computed flow field near the airfoil.

The modified far field potential flow boundary conditions were also used at the near-circular five chord radius outer boundary defined above to obtain a solution again for  $\alpha = 5^\circ$ . After two characteristic times, the outer modified freestream boundary conditions were held constant since the lift coefficient had small variations less than 1%. The solution exhibited a small oscillatory behavior similar to the freestream boundary condition result even after four characteristic time periods. The lift coefficient had a mean value within 1% of the freestream boundary condition value with variations below 1%. The drag coefficient had the same average value as the previous result, but the oscillations were larger with a deviation from the mean of approximately  $\pm 10\%$  (10 drag counts). The unsteadiness was again observed to emanate from the laminar separation bubble.

Small pressure oscillations propagated downstream on the upper surface of the airfoil and were eventually damped out near the trailing edge. In each case no changes were made in any of the turbulence or other parameters during the computations. Small changes in the turbulence transition near the bubble would probably prevent the unsteadiness.

The far field boundary condition study has indicated that the use of the freestream boundary conditions at the large but finite distance from the airfoil surface is sufficient for the computation of the near surface flow field and force coefficients. Variations in the outer boundary placement and the use of a more accurate far field boundary condition had negligible effects on the present numerical solution.

The numerical implementation of the downstream no change boundary condition was also investigated. Second order accurate central spatial and upwind differences were used in separate solutions for an angle of attack of 7.5°. No difference ( $\pm 0.01\%$ ) was observed in the surface pressure distributions or computed force coefficients between the two boundary conditions. The computed velocities at locations across the wake on the outer boundary for the two cases differed by less than 1%. The upwind difference formulation was chosen because of the associated convective properties.

The sensitivity of the numerical solution to the fineness of the grid was examined. The 7.5° angle of attack case was chosen because both the laminar separation bubble and a region of separated flow near the trailing edge are present. A coarse grid was obtained from the 79x44 grid by deleting the odd numbered  $n$  contours except for the body contour. The coarse 79x23 grid was a subset of the full coordinate system and was used to study the effect of boundary layer resolution on the numerical solution. The turbulence parameters and SOR acceleration parameters were unchanged from the previous solution. The coarse grid computation was

carried out over four characteristic time periods. The calculated values for the lift and drag coefficients approached a "steady" periodic state after two characteristic times with a period of  $0.6T$ . The mean value of the lift coefficient, averaged over the last two characteristic times, became  $0.606 \pm 2\%$  compared with the full grid solution value of 0.606. The computed mean drag coefficient was  $0.0260 \pm 15\%$  compared with the  $79 \times 44$  grid solution result of 0.0240. Values for the wake velocities in the freestream direction along the outer boundary for each solution compared within 1%. The unsteadiness was found to originate from the oscillating laminar separating shear layer which forms the front portion of the bubble. The edge of the boundary layer varied between the  $J=3$  and  $J=4$   $\eta$  contours, as defined by the  $79 \times 23$  grid system, at the  $1\frac{1}{2}$  chord location. This motion also caused the bubble to vary in length and produced pressure oscillations along the upper surface. This unsteadiness is probably attributed to the reduced resolution of the bubble in the  $\eta$  direction. Similar sensitivity has already been discussed concerning the resolution of the extremely short bubble in the  $\xi$  direction at larger angles of attack.

The computed flow field near the airfoil and the calculation of the force coefficients using the coarse grid are in agreement with the results for the complete  $79 \times 44$  grid. A quadratic Richardson's extrapolation on the computed drag coefficients indicates an error of  $\pm 0.0007$ . This agreement indicates that the solution obtained with the full  $79 \times 44$  coordinate system is adequate to obtain  $\pm 10$  drag counts and therefore sufficiently approximates the limiting numerical solution obtained from an extremely fine grid. The coarse grid computation further indicates that the numerical multi-grid approach (100) may be implemented for complex flows using general grid transformations. The use of only one-half the grid points, for instance, during most of the time marching procedure would significantly reduce the computer time required for an equivalent numerical solution.

## SECTION VI

### CONCLUSIONS AND RECOMMENDATIONS

Numerical solutions have been obtained for two-dimensional incompressible turbulent flow over airfoils near stall. The time dependent Reynolds averaged incompressible Navier-Stokes equations in the primitive variables of velocity and pressure together with a Poisson pressure equation are numerically solved. An algebraic eddy viscosity approach is modified for separated adverse pressure gradient flows and used to model turbulent closure of the laminar separation bubble and the subsequent turbulent boundary layer. A deficiency in the standard model is detected and corrected by using a "limiting" technique. A body-fitted coordinate system is numerically transformed to a rectangular grid in the computational plane. The set of transformed partial differential equations is solved with an implicit finite difference method. Successive-over-relaxation iteration is used to solve the system of linearized difference equations at each time step.

Numerical solutions are presented for a NACA 0012 airfoil near stall at a chord Reynolds number of 170,000. A short laminar separation bubble located near the upper surface suction pressure peak is obtained. Computed laminar separation bubble characteristics including the criteria for separation, bubble type, and turbulent transition agree with empirical results. Surface mean pressure distributions are presented and found to compare favorably with experimental data. The separation bubble is observed for angles of attack of 5° and 7.5°. For larger angles of attack, the small bubble essentially disappeared within the numerical resolution of the streamwise grid spacing. The steep leading edge suction pressure peak is well defined for each angle of attack. Velocity profiles at four stations

along the upper airfoil surface are compared with experimental results. The experimental data were obtained at similar grid point locations so that interpolation was not required. The calculated lift and drag coefficients are in excellent agreement with the experimental data. The lift coefficients are within 5% of the experimental values near stall, and the computed drag coefficients are within 10 drag counts in the region of maximum lift to drag ratio. The effects of viscous separation on the lift coefficient curve which produces a maximum value are seen and contrasted with a numerically obtained inviscid potential solution with Kutta condition. The observed phenomena of trailing edge stall is predicted where the rear separation point moves forward with increasing angle of attack.

The sensitivity of the numerical solution has been examined in several areas. A far field potential flow boundary condition which modifies the freestream conditions for use at a large but finite distance from the airfoil was considered for two outer boundary placements. The study showed that the use of the infinite freestream conditions at an outer circular boundary of radius 10 chords produces negligible influence on the near flow field and calculated values for the force coefficients. A coarse 79x23 grid, compared with the 79x44 grid, was used to evaluate truncation error. An analysis of convergence for successive-over-relaxation iteration predicts an upper limit on the time increment for the implicit finite difference method. Numerical experiments confirmed this upper bound. Several parameters within the turbulence model were systematically varied. The only significant sensitivity occurred near the downstream side of the laminar separation bubble. Small changes in turbulent transition length and location were found to significantly change the flow field. This sensitivity may be related to incipient turbulent separation which results in failure to close the separation

bubble. This leading edge stall phenomena is observed at higher Reynolds numbers for the NACA 0012 airfoil.

The agreement between the numerical solutions and the experimental data and empirical results indicates that the eddy viscosity approach modified for separated adverse pressure gradient flows adequately models the turbulence on the upper airfoil surface. The near stall airfoil aerodynamic characteristics are consequently accurately predicted by the numerical method.

The results of this investigation have suggested areas for further research. A more exhaustive study of the laminar separation bubble should be accomplished to better understand the phenomena of leading edge stall. The computation of a geometry with detailed experimental results for this purpose is desirable. Further research in adapting the multi-grid technique would significantly increase the computational efficiency and appears feasible as a result of the coarse grid calculation. Turbulence modelling is an area of substantial interest and should be pursued in conjunction with experimental investigations. The improved accuracy of current computational aerodynamics also indicates that the errors in experimental measurements should be analyzed in a more rigorous manner so that comparisons can be better evaluated. The method should also be employed in time dependent problems to further exploit the time marching technique.

## REFERENCES

1. Winslow, Alan M., "Numerical Solution of the Quasilinear Poisson Equation in a Nonuniform Triangle Mesh", J. Comp Phys., 1 (1966), 14<sup>a</sup>.
2. Chu, Wen-Hwa, "Development of a General Finite Difference Approximation for a General Domain, Part I: Machine Transformation", J. Comp. Phys., 8 (1971), 392.
3. Amsden, A. and Hirt, C., "A Simple Scheme for Generating General Curvilinear Grids", J. Comp. Phys., 11 (1973), 348.
4. Thompson, J. F., Thames, F. C., and Mastin, C. W., "Automatic Numerical Generation of Body-Fitted Curvilinear Coordinate System for Fields Containing Any Number of Arbitrary Two-Dimensional Bodies", J. Comp. Phys., 15 (1974), 299.
5. Thompson, J. F., Thames, F. C., and Mastin, C. W., "Boundary-Fitted Curvilinear Coordinate Systems for Solution of Partial Differential Equations on Fields Containing Any Number of Arbitrary Two-Dimensional Bodies", NASA-CR-2729, 1977.
6. Thompson, J. F., Thames, F. C., and Mastin, C. W., "TOMCAT- A Code for Numerical Generation of Boundary-Fitted Curvilinear Coordinate Systems on Fields Containing Any Number of Arbitrary Two-Dimensional Bodies", J. Comp. Phys., 24 (1977), 274.
7. Hodge, J. K. and Stone, A. L., "Numerical Solution for Airfoils Near Stall in Optimized Boundary-Fitted Curvilinear Coordinates", AIAA J., 17 (1979), 458.
8. Steger, J. L. and Sorenson, R. L., "Automatic Mesh-Point Clustering Near a Boundary in Grid Generation with Elliptic Partial Differential Equations", J. Comp. Phys., 33 (1979), 405.
9. Sorenson, R. L., "A Computer Program to Generate Two-Dimensional Grids About Airfoils and Other Shapes by the Use of Poisson's Equation", NASA-TM-81198, 1980.
10. Mastin, C. W. and Thompson, J. F., "Three-Dimensional Body-Fitted Coordinate Systems for Numerical Solution of the Navier-Stokes Equations", AIAA Paper 78-1147, 1978.
11. Meyder, R., "Solving the Conservation Equations in Fuel Rod Bundles Exposed to Parallel Flow by Means of Curvilinear-Orthogonal Coordinates", J. Comp. Phys., 17 (1975), 53.
12. Theodorsen, T. and Garrick, I. E., "General Potential Theory of Arbitrary Wing Sections", NACA-TR-452, 1933.
13. Ives, David C., "A Modern Look at Conformal Mapping Including Multiply Connected Regions", AIAA J., 14 (1976), 1006.

14. Gibeling, H. J., Shamroth, S. J., and Eiseman, P. R., "Analysis of Strong-Interaction Dynamic Stall for Laminar Flow on Airfoils", NASA-CR-2969, 1978.
15. Eiseman, Peter R., "A Coordinate System for a Viscous Transonic Cascade Analysis", J. Comp. Phys., 26 (1978), 307.
16. Eiseman, Peter R., "A Multi-Surface Method of Coordinate Generation", J. Comp. Phys., 33 (1979), 118.
17. Eiseman, Peter R., "Coordinate Generation with Precise Controls", ICASE Rept 80-16, 1980.
18. Boussinesq, J., "Theorie de l'écoulement tourbillant", Mem. Pres. Acad. Sci. XXIII, 46 (1877).
19. Prandtl, L., "Bericht über Untersuchungen zur ausgebildeten Turbulenz", ZAMM, 5 (1925), 136.
20. Cebeci, T. and Smith, A. M. O., article from Computation of Turbulent Boundary Layers, AFOSR-IFP Conf., 1 (1968), Stanford Univ. Press, 346.
21. Mellor, G. L. and Herring, H. J., "Two Methods of Calculating Turbulent Boundary Layer Behavior Based on Numerical Solutions of the Equations of Motion", Computations of Turbulent Boundary Layers, AFOSR-IFP Conf., 1 (1968), Stanford Univ. Press, 331.
22. Patankar, S. V. and Spalding, D. B., article from Computations of Turbulent Boundary Layers, AFOSR-IFP Conf., 1 (1968), Stanford Univ. Press, 356.
23. Van Driest, E. R., "On Turbulent Flow Near a Wall", J. Aerospace Sci., 23 (1956), 1007.
24. Cebeci, T. and Smith, A. M. O., Analysis of Turbulent Boundary Layers, Academic Press, NY, 1974.
25. Launder, B. E. and Spalding, D. B., Mathematical Models of Turbulence, Academic Press, NY, 1972.
26. Prandtl, L., "Über ein neues Formelsystem für die ausgebildete Turbulenz", Nachrichten von der Akad. der Wissenschaften in Göttingen, (1945), 6.
27. Glushko, G. S., "Turbulent Boundary Layer on a Flat Plate in an Incompressible Fluid", NASA-TM-F-10080, 1966.
28. Mellor, G. L. and Herring, H. J., article from Computations of Turbulent Boundary Layers, AFOSR-IFP Stanford Conf., 1 (1968), Stanford Univ. Press, 247.
29. Wolfshtein, M., "The Velocity and Temperature Distribution in One-Dimensional Flow with Turbulence Augmentation and Pressure Gradient", Int. J. Heat Mass Transfer, 12 (1969), 301.

30. Bradshaw, P., Ferriss, D., and Atwell, N., "Calculation of Boundary-Layer Development Using the Turbulence Energy Equation", J. Fluid Mech., 28 (1967), 593.
31. Nee, V. and Kovasznay, L., "Simple Phenomenological Theory of Turbulent Shear Flows", J. Phys. Fluids, 12 (1969), 473.
32. Kolmogorov, A. N., "Equations of Turbulent Motion in an Incompressible Fluid", IZV Akad. Nauk. SSSR, Ser. Fiz., 6 (1942), 56.
33. Ng, K. H. and Spalding, D. B., "Turbulence Model for Boundary Layer Near Walls", J. Phys. Fluids, 15 (1972), 20.
34. Rotta, J. C., "Statistische Theorie nichthomogener Turbulenz", Z. Phys., 129 (1951), 546.
35. Saffman, P., "A Model for Inhomogeneous Turbulent Flow", Proc. Roy. Soc. London, 317 (1970), 417.
36. Wilcox, D. and Rubesin, M., "Progress in Turbulence Modeling for Complex Flow Fields Including Effects of Compressibility". NASA-TP-1517, 1980.
37. Jones, W. and Launder, B., "The Prediction of Laminarization with a Two-Equation Model of Turbulence". Int. J. Heat Mass Transfer, 15 (1972), 301.
38. Donaldson, C. and Rosenbaum, H., "Calculation of Turbulent Shear Flows Through Closure of the Reynolds Equations by Invariant Modeling", NASA-CR-128172, 1968.
39. Hanjalic, K. and Launder, B., "A Reynolds Stress Model of Turbulence and its Application to Thin Shear Layers", J. Fluid Mech., 52 (1972), 609.
40. Kolovandin, B. and Vatutin, I., "Statistical Transfer Theory in Non-Homogeneous Turbulence", Int. J. Heat Mass Transfer, 15 (1972), 2371.
41. Ferziger, J., "Large Eddy Numerical Simulations of Turbulent Flows", AIAA J., 15 (1977), 1261.
42. Walker, R., "Numerical Solution of the Navier-Stokes Equations for Incompressible Viscous Laminar Flow Past a Semi-Infinite Flat Plate", MS Thesis, Mississippi State University, 1974.
43. Pai, Shih, Viscous Flow Theory, Part I Laminar Flow, D. Van Nostrand, NY, 1956.
44. Thames, F., "Numerical Solution of the Incompressible Navier-Stokes Equations about Arbitrary Two-Dimensional Bodies", Ph D Dissertation, Mississippi State University, 1975.
45. Mehta, U. and Lavan, Z., "Starting Vortex, Separation Bubbles, and Stall: A Numerical Study of Laminar Unsteady Flow Around an Airfoil", J. Fluid Mech., 67 (1975), 227.

46. Reddy, R. and Thompson, J., "Numerical Solution of Incompressible Navier-Stokes Equations in the Integro-Differential Formulation Using Boundary-Fitted Coordinate Systems", AIAA Paper 77-650, 1977.
47. Sankar, N. and Wu, J. C., "Viscous Flow Around Oscillating Airfoils - A Numerical Study", AIAA Paper 78-1225, 1978.
48. Sankar, N. and Tassa, Y., "Reynolds Number and Compressibility Effects on Dynamic Stall of a NACA 0012 Airfoil", AIAA Paper 80-0010, 1980.
49. Briley, W. and McDonald, H., "Solution of the Multidimensional Compressible Navier-Stokes Equations by a Generalized Implicit Method", J. Comp. Phys., 24 (1977), 372.
50. Sugavanam, A. and Wu, J., "Numerical Study of Separated Turbulent Flow Over Airfoils", AIAA Paper 80-1441, 1980.
51. Harlow, F. and Welch, J., "Numerical Calculation of Time-Dependent Viscous Incompressible Flow of Fluid with Free Surface", Phys. of Fluids, 8 (1965), 2182.
52. Hirt, C. and Harlow, F., "A General Corrective Procedure for the Numerical Solution of Initial Value Problems", J. Comp. Phys., 2 (1967), 114.
53. Hodge, J. K., "Numerical Solution of Incompressible Laminar Flow About Arbitrary Bodies in Body-Fitted Curvilinear Coordinates", Ph D Dissertation, Mississippi State University, 1975.
54. Ghia, K., Hankey, W., and Hodge, J., "Study of Incompressible Navier-Stokes Equations in Primitive Variables Using Implicit Numerical Technique", AIAA Paper 77-0648, 1977.
55. Chien, J., "Vorticity-Stream Function Formulation of Compressible and Incompressible Turbulent Internal Flows", AEDC-TR-79-13, 1979.
56. Jacobs, E. and Sherman, A., "Airfoil Characteristics as Affected by Variations of the Reynolds Number", NACA Rept 586, 1937.
57. Deiwert, G., "Numerical Simulation of High Reynolds Number Transonic Flows", AIAA J., 13 (1975), 1354.
58. MacCormack, R. W. and Paullay, A., "Computational Efficiency Achieved by Time Splitting of Finite Difference Operators", AIAA Paper 72-154, 1972.
59. Steger, J., "Implicit Finite Difference Simulation of Flow About Arbitrary Two-Dimensional Geometries", AIAA J., 16 (1978), 679.
60. Beam, R. and Warming, R., "An Implicit Finite Difference Algorithm for Hyperbolic Systems in Conservative-Law-Form", J. Comp. Phys., 22 (1976), 87.
61. Walitt, L., King, L., and Liu, C., "Computation of Viscous Transonic Flow About a Lifting Airfoil", AIAA Paper 77-679, 1977.

62. Trulio, J., "Theory and Structure of the AFTON Codes", AFWL-TR-66-19, 1966.
63. Cebeci, T., Smith, A. M. O., and Mosinskis, G., "Calculations of Compressible Adiabatic Turbulent Boundary Layers", AIAA J., 8 (1970), 1974.
64. Shamroth, S. and Gibeling, H., "A Compressible Solution of the Navier-Stokes Equations for Turbulent Flow About an Airfoil", NASA-CR-3183, 1979.
65. McAlister, K., Carr, L., and McCroskey, W., "Dynamic Stall Experiments on the NACA 0012 Airfoil", NASA-TP-1100, 1978.
66. Bland, S., "AGARD Two-Dimensional Aeroelastic Configurations", AGARD-AR-156, 1979.
67. Abbott, I. and Von Doenhoff, A., Theory of Wing Sections, Dover Pub., NY, 1959.
68. Chorin, A., "Numerical Solution of the Navier-Stokes Equations", Math. Comp., 22 (1968), 745.
69. Shang, J., Hankey, W., and Dwoyer, D., "Compressible Turbulent Boundary Layer Solutions Employing Eddy Viscosity Models", ARL 73-0041, 1973.
70. Coles, D., "The Law of the Wake in the Turbulent Boundary Layer", J. Fluid Mech., 1 (1956), 191.
71. Jobe, C. and Hankey, W., "Turbulent Boundary Layer Calculations in Adverse Pressure Gradient Flows", AIAA Paper 80-136, 1980.
72. McCullough, G. and Gault, D., "Examples of Three Representative Types of Airfoil Section Stall at Low Speed", NACA-TN-2502, 1951.
73. Bachalo, W. and Johnson, D., "An Investigation of Transonic Turbulent Boundary Layer Separation Generated on an Axisymmetric Flow Model", AIAA paper 79-1479, 1979.
74. Baker, A. and Orzechowski, J., "An Interaction Algorithm for Prediction of Mean and Fluctuating Velocities in Two-Dimensional Aerodynamic Wake Flows", NASA-CR-3301, 1980.
75. Dhawan, S. and Narasimha, R., "Some Properties of Boundary-Layer Flow During the Transition from Laminar to Turbulent Motion", J. Fluid Mech., 3 (1958), 418.
76. Narasimha, R. and Prabhu, A., "Equilibrium and Relaxation in Turbulent Wakes", J. Fluid Mech., 54 (1972), 1.
77. Green, J., Weeks, D., and Broome, J., "Prediction of Turbulent Boundary Layers and Wakes in Compressible Flow by a Lag-Entrainment Method", ARC-R/M-3791, 1977.

78. Inouye, M., Marvin, J., and Sheaffer, Y., "Turbulent-Wake Calculations with an Eddy-Viscosity Model", AIAA J., 10 (1972), 216.
79. Burggraf, O. R., "Comparative Study of Turbulence Models for Boundary Layers and Wakes", ARL-74-31, 1974.
80. Bradshaw, P., Dean, R., and McEligot, D., "Calculation of Interacting Turbulent Shear Layers: Duct Flow", Trans. ASME, Series I: J. Fluids Eng., 95 (1973), 214.
81. Varga, R., Matrix Iterative Analysis, Prentice-Hall, New Jersey, 1962.
82. Ghia, U., Hodge, J., and Hankey, W., "An Optimization Study for Generating Surface-Oriented Coordinates for Arbitrary Bodies in High-Re Flow", AFFDL-TR-77-117, 1977.
83. Roache, P., Computational Fluid Mechanics, Hermosa Publishers, NM, 1976.
84. Unpublished Experimental Data on NACA 0012 Airfoil Section, Air Force F. J. Seiler Research Laboratory.
85. Gault, D., "An Experimental Investigation of Regions of Separated Laminar Flow", NACA-TN-3505, 1955.
86. Gaster, M., "The Structure and Behavior of Laminar Separation Bubbles", ARC-R/M-3595, 1969.
87. Hoad, D., Young, W., and Meyers, J., "Velocity Measurements about a NACA 0012 Airfoil with a Laser Velocimeter", NASA Langley Rept, 1978.
88. Arena, A. and Mueller, T., "Laminar Separation, Transition, and Turbulent Reattachment near the Leading Edge of Airfoils", AIAA J., 18 (1980), 747.
89. Gregory, N. and O'Reilly, C., "Low-Speed Aerodynamic Characteristics of NACA 0012 Airfoil Section, Including the Effects of Upper-Surface Roughness Simulating Hoar Frost", ARC-R/M-3726, 1973.
90. Wallis, R., "Boundary Layer Transition at the Leading Edge of Thin Wings and its Effect on General Nose Separation", ICAS 2nd Congress, Zurich, 1960.
91. Curie, N. and Skan, S., "Approximate Methods for Predicting Separation Properties of Laminar Boundary Layers", Aero. Quarterly, 8 (1957), 257.
92. Owen, P. and Klanfer, L., "On the Laminar Boundary Layer Separation from the Leading Edge of a Thin Aerofoil", RAE Rept 2508, 1953.
93. Crabtree, L., "The Formation of Regions of Separated Flow on Wing Surfaces", ARC-R/M-3122, 1957.
94. Crabtree, L., "Prediction of Transition in the Boundary Layer on an Aerofoil", J. Royal Aerc. Soc., 62 (1958), 525.

95. Roberts, W., "Calculation of Laminar Separation Bubbles and Their Effect on Airfoil Performance", AIAA J., 18 (1980), 25.
96. Coles, D. and Wadcock, A., "A Flying-Hot-Wire Study of Two-Dimensional Mean Flow Past a NACA 4412 Airfoil at Maximum Lift", AIAA Paper 78-1196, 1978.
97. Pope, A. and Harper, J., Low Speed Wind Tunnel Testing, John Wiley and Sons, NY, 1966.
98. Waskiewicz, J., Shang, J. and Hankey, W., "Numerical Simulation of Near Wakes Utilizing a Relaxation Turbulence Model", AIAA Paper 79-148, 1979.
99. Hasen, G., "Navier-Stokes Solutions for an Axisymmetric Nozzle with a Thick Base Annulus in Supersonic Flow", Ph D Dissertation, Air Force Institute of Technology, to be published.
100. Brandt, A., "Multi-Level Adaptive Computations in Fluid Dynamics", AIAA Paper 79-1455, 1979.
101. Klunker, E. B., "Contribution to Methods for Calculating the Flow About Thin Lifting Wings at Transonic Speeds - Analytic Expressions for the Far Field", NASA-TN-D-6530, 1971.

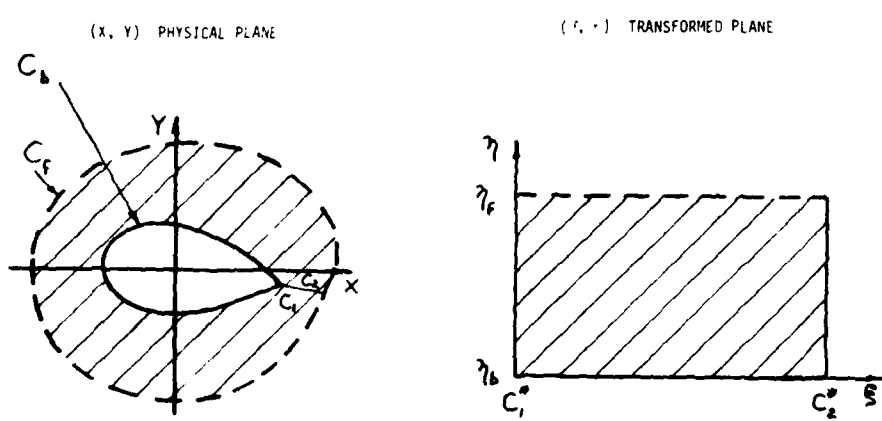


FIGURE 1 PHYSICAL AND TRANSFORMED PLANES

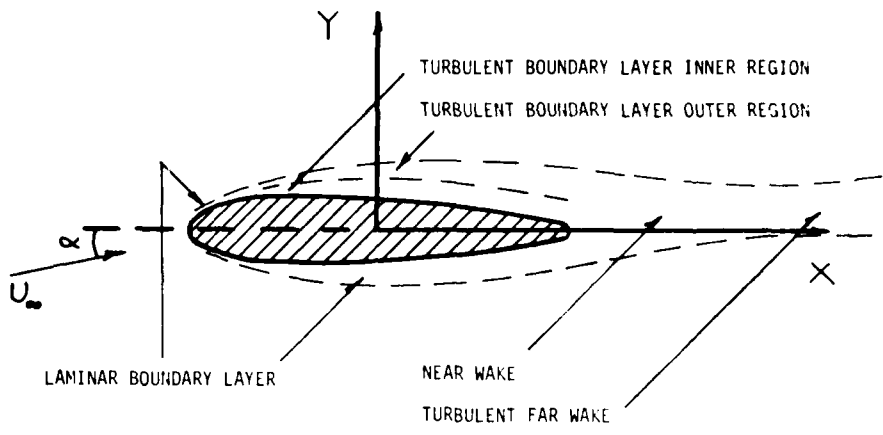


FIGURE 2 REGIONS OF TURBULENT FLOW

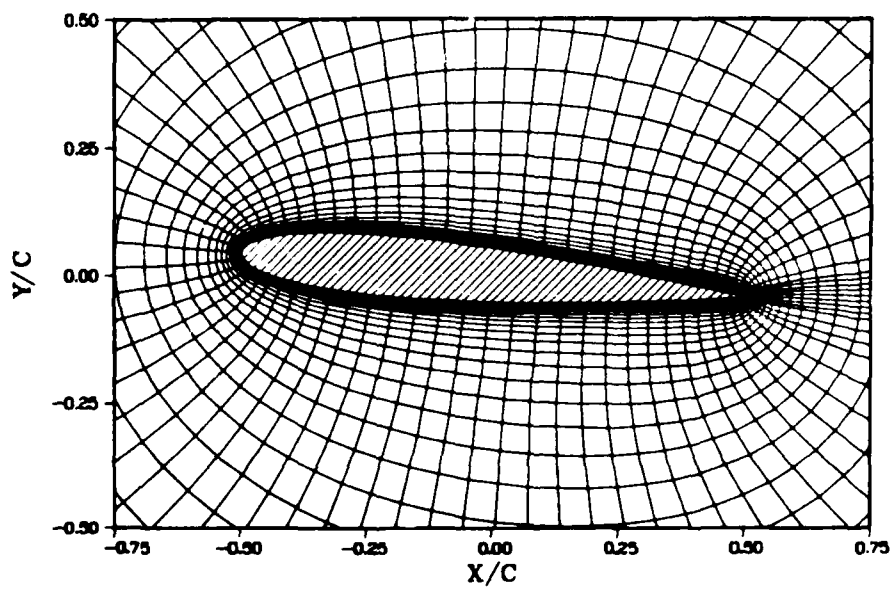


FIGURE 3 PORTION OF 79x44 BODY-FITTED GRID (FIRST 30 CONSTANT  $\gamma$  LINES)

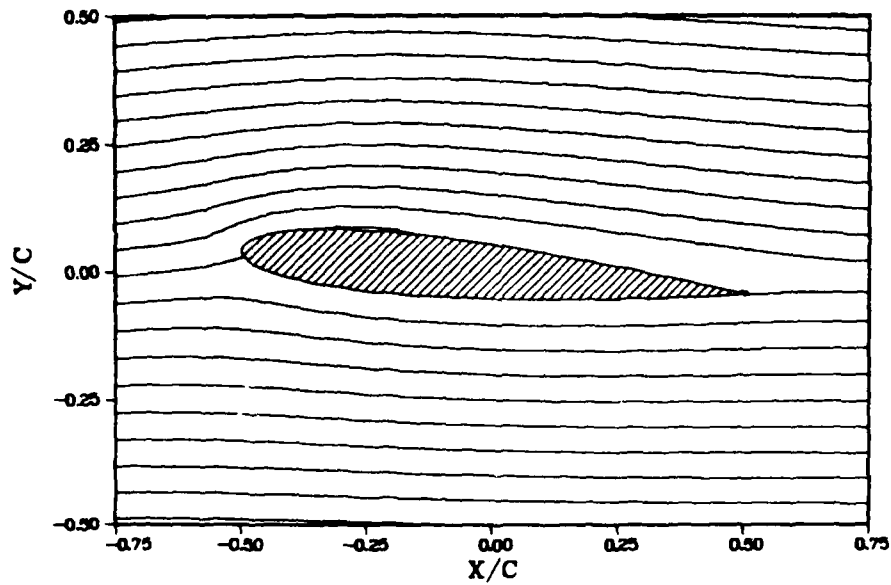


FIGURE 4 MEAN FLOW STREAMLINE CONTOURS ( $\alpha = 5^\circ$ )

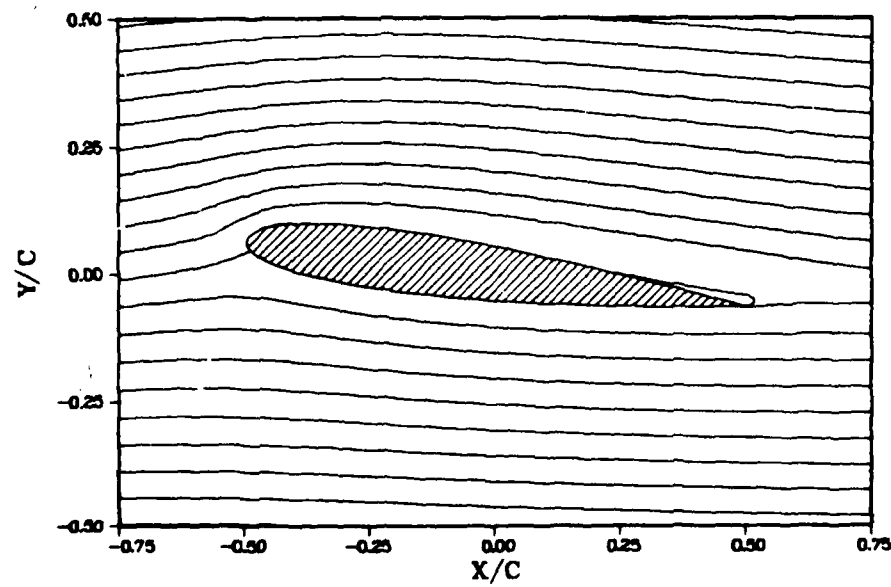


FIGURE 5 MEAN FLOW STREAMLINE CONTOURS ( $\alpha = 7.5^\circ$ )

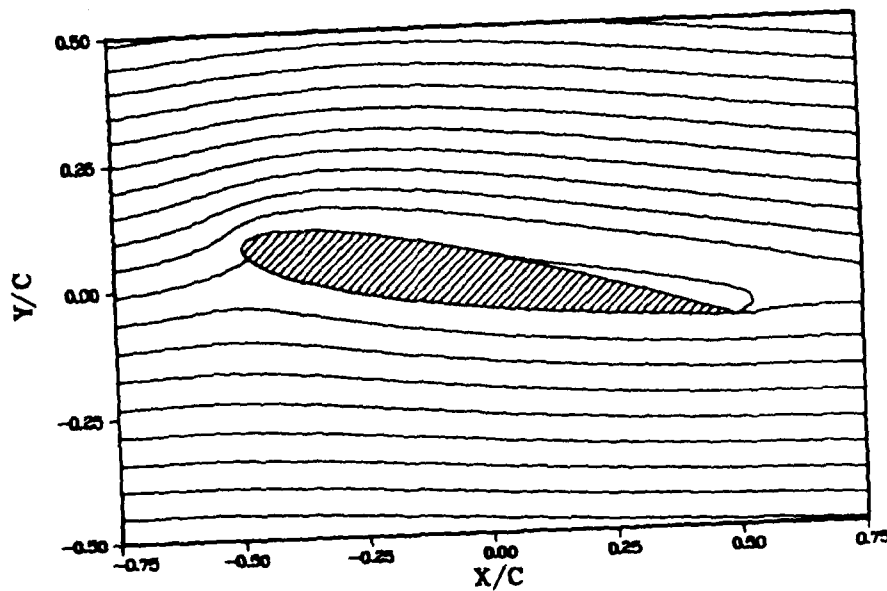


FIGURE 6 MEAN FLOW STREAMLINE CONTOURS ( $\alpha = 9.5^\circ$ )

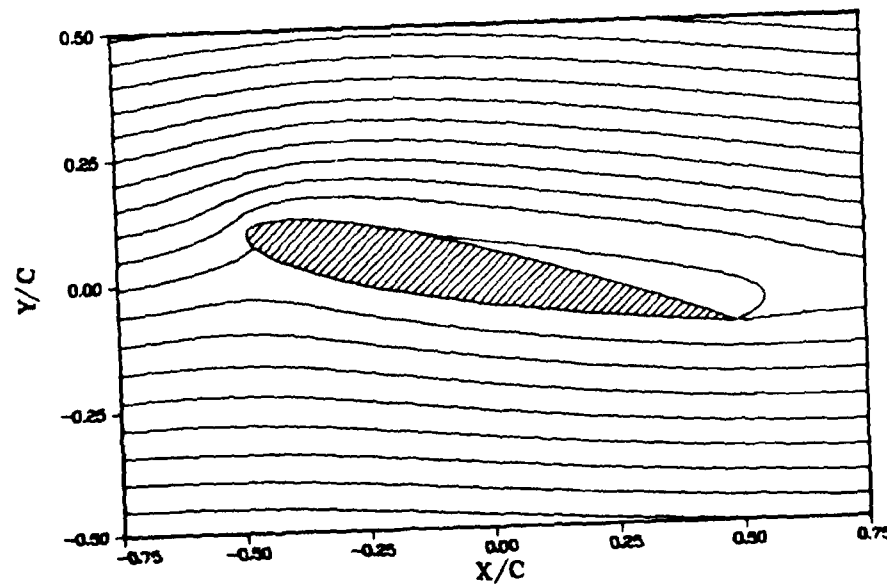


FIGURE 7 MEAN FLOW STREAMLINE CONTOURS ( $\alpha = 11.5^\circ$ )

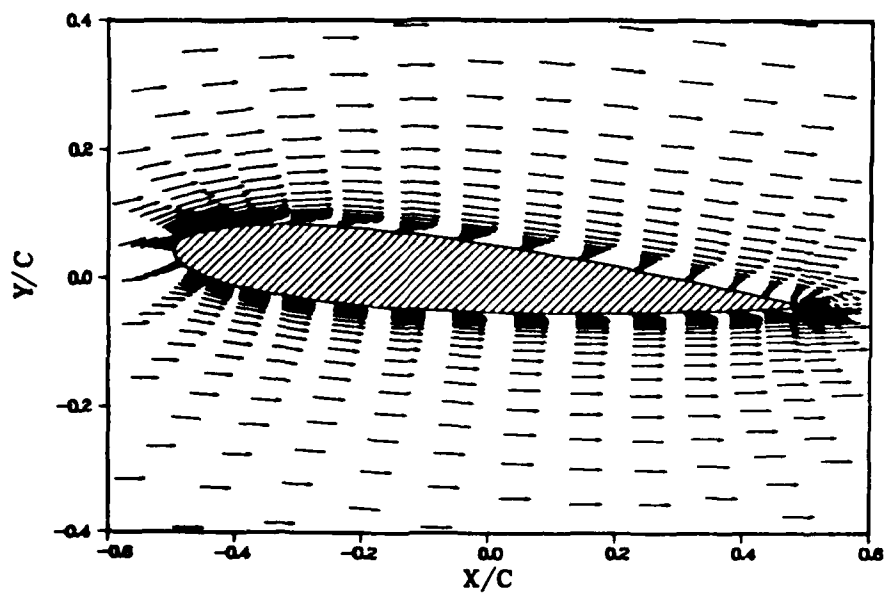


FIGURE 8 MEAN FLOW VELOCITY FIELD ( $\alpha = 5^\circ$ )

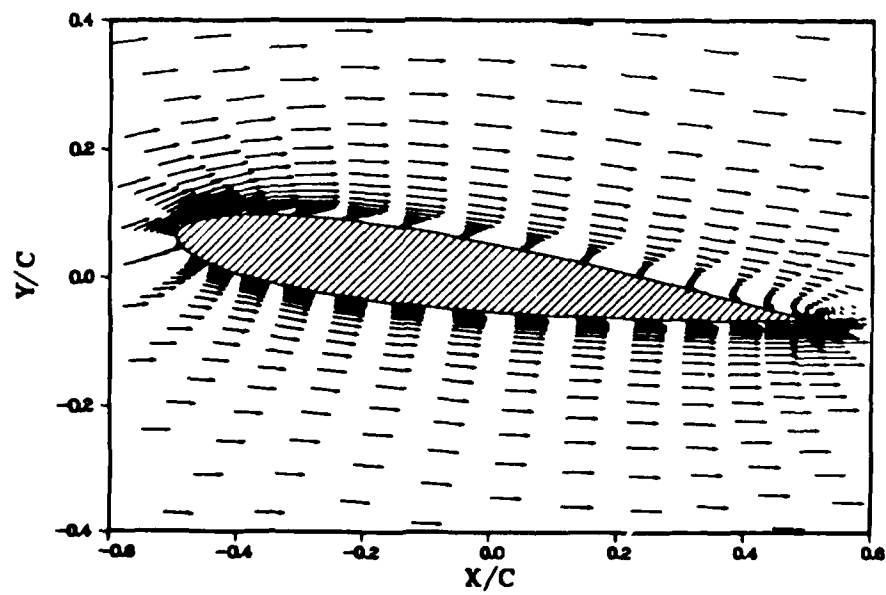


FIGURE 9 MEAN FLOW VELOCITY FIELD ( $\alpha = 7.5^\circ$ )

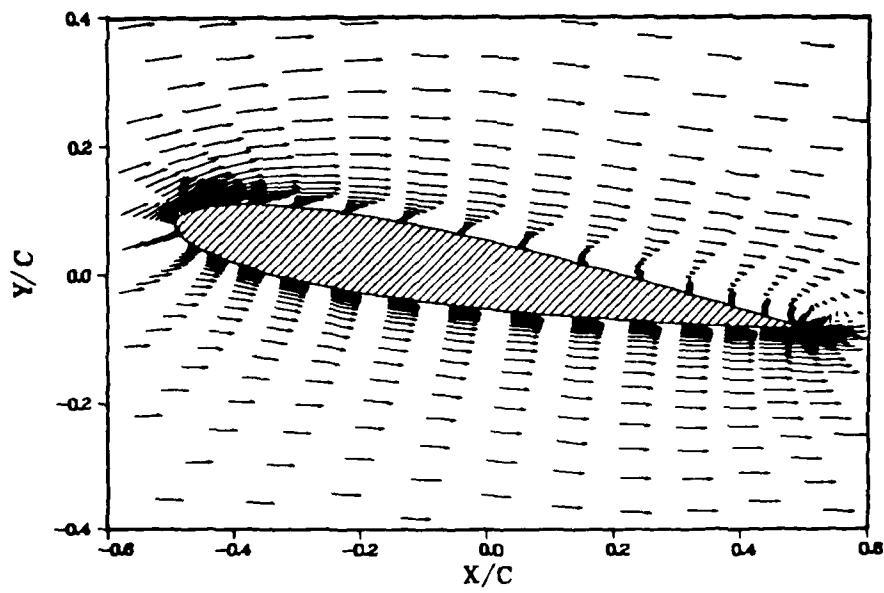


FIGURE 10 MEAN FLOW VELOCITY FIELD ( $\alpha = 9.5^\circ$ )

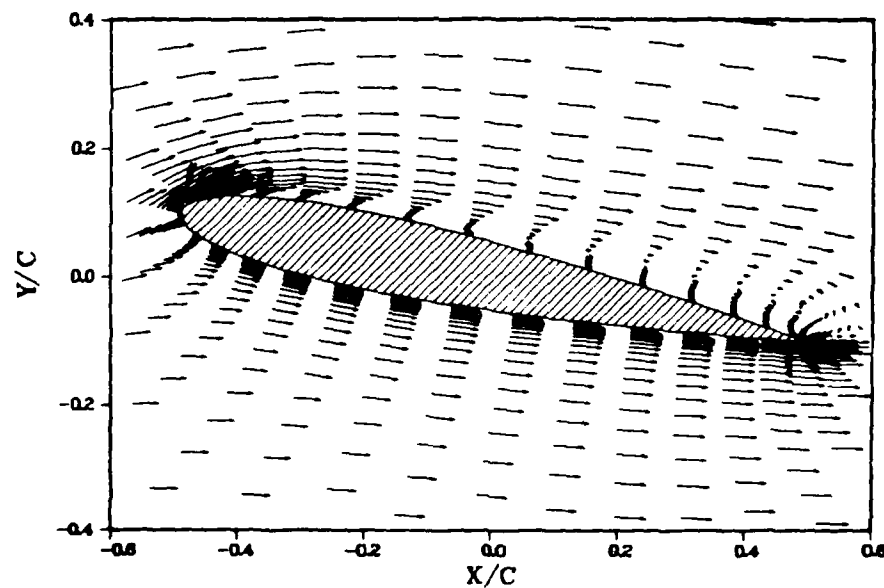


FIGURE 11 MEAN FLOW VELOCITY FIELD ( $\alpha = 11.5^\circ$ )

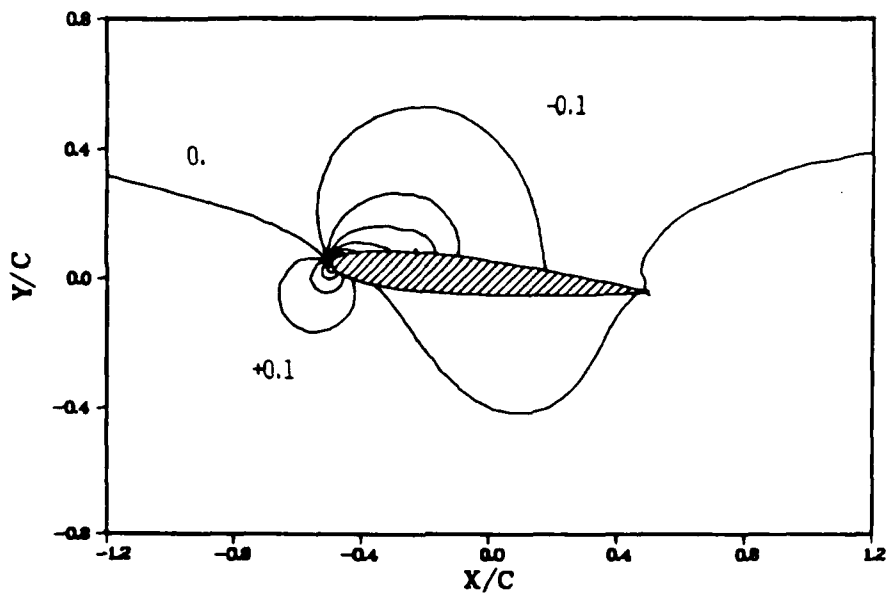


FIGURE 12 MEAN FLOW PRESSURE CONTOURS ( $\alpha = 5^\circ$ )

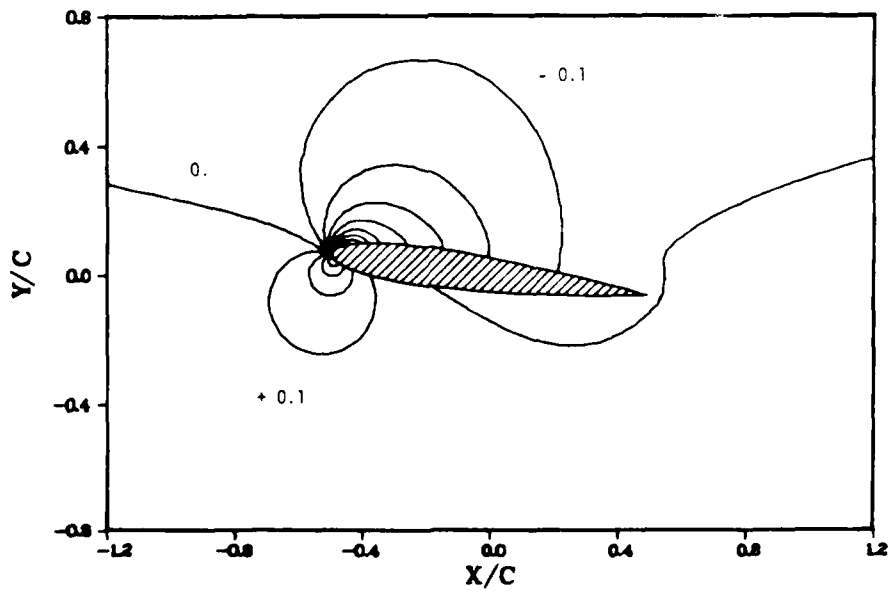


FIGURE 13 MEAN FLOW PRESSURE CONTOURS ( $\alpha = 7.5^\circ$ )

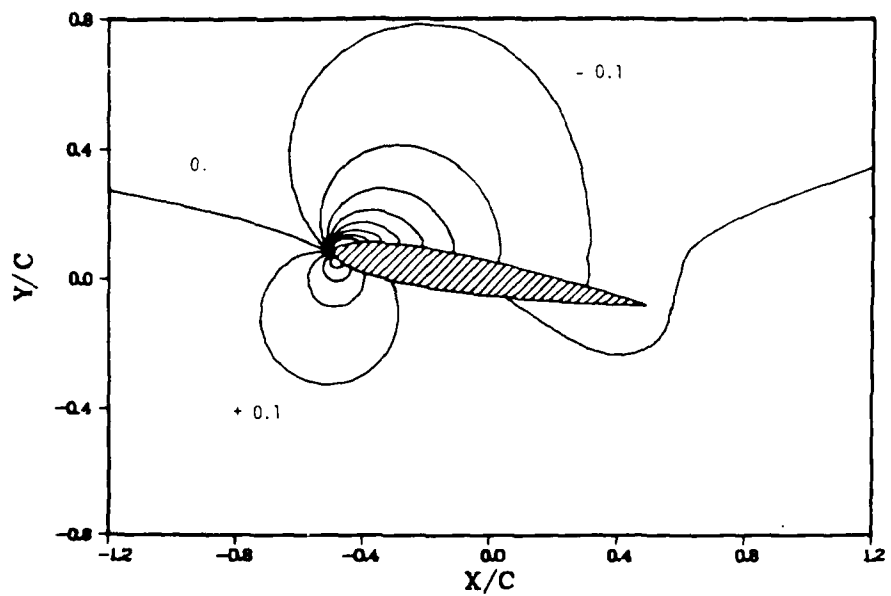


FIGURE 14 MEAN FLOW PRESSURE CONTOURS ( $\alpha = 9.5^\circ$ )

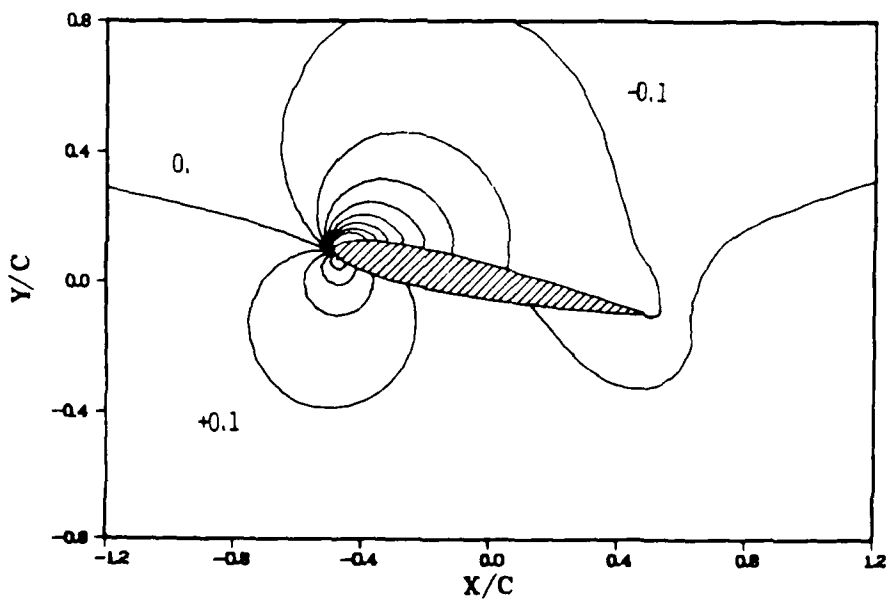


FIGURE 15 MEAN FLOW PRESSURE CONTOURS ( $\alpha = 11.5^\circ$ )

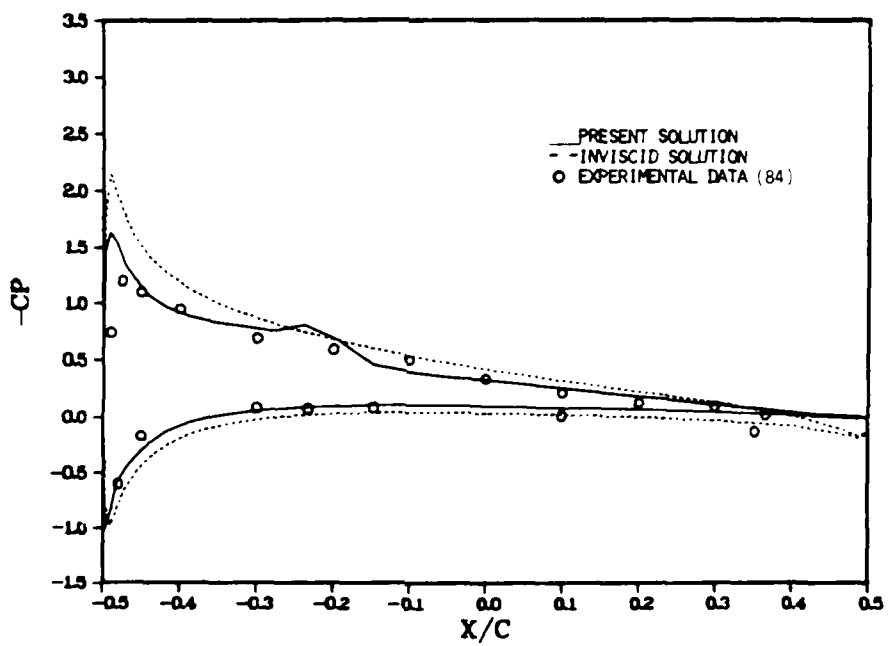


FIGURE 16 SURFACE MEAN PRESSURE COEFFICIENTS ( $\alpha = 5^\circ$ )

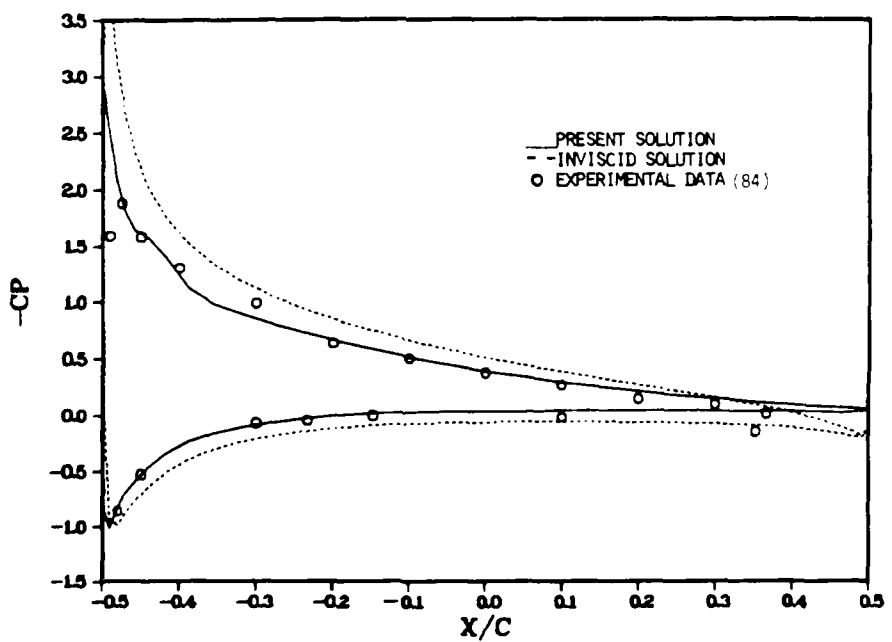


FIGURE 17 SURFACE MEAN PRESSURE COEFFICIENTS ( $\alpha = 7.5^\circ$ )

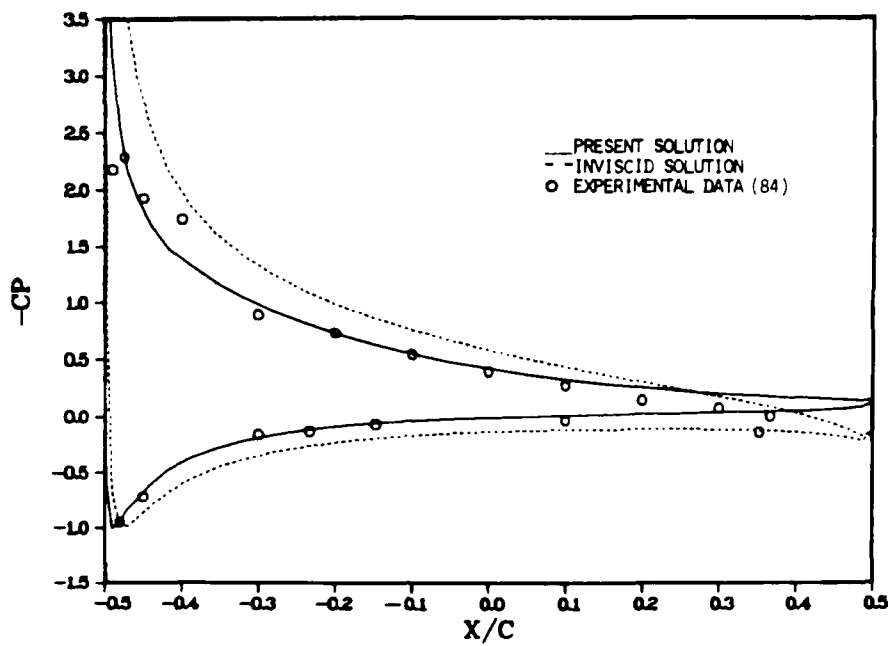


FIGURE 18 SURFACE MEAN PRESSURE COEFFICIENTS ( $\alpha = 9.5^\circ$ )

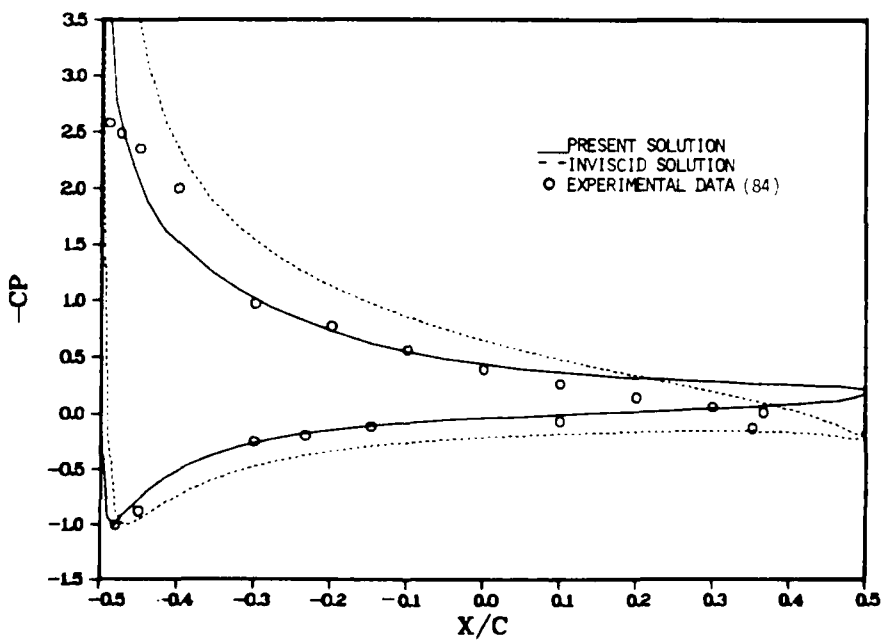


FIGURE 19 SURFACE MEAN PRESSURE COEFFICIENTS ( $\alpha = 11.5^\circ$ )

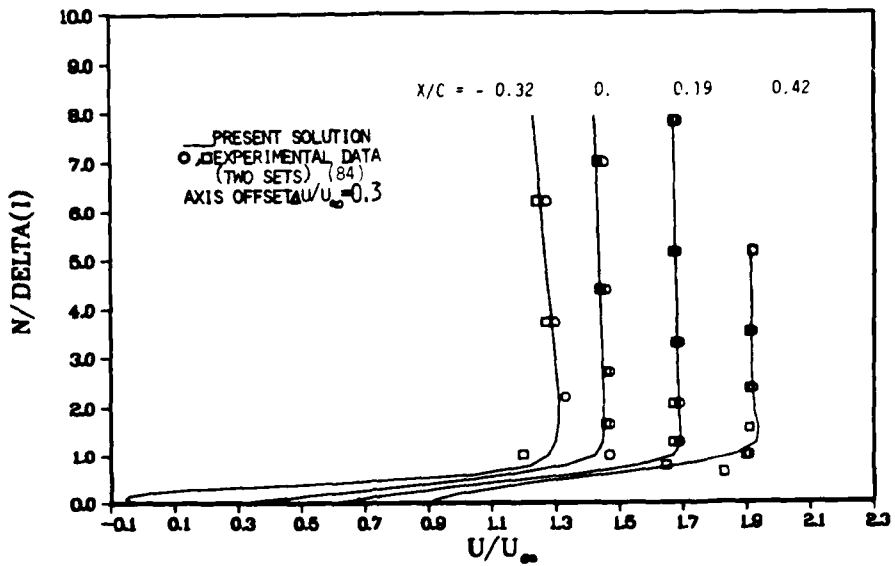


FIGURE 20 MEAN FLOW VELOCITY VERSUS SURFACE NORMAL DISTANCE NONDIMENSIONALIZED BY COMPUTED BOUNDARY LAYER THICKNESS AT CHORD LOCATIONS ON UPPER SURFACE ( $\alpha = 5^\circ$ )

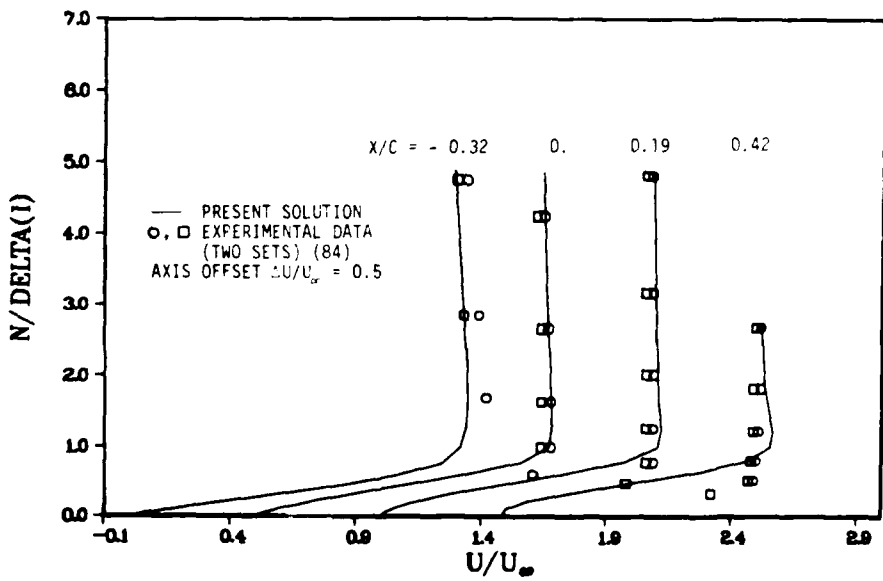


FIGURE 21 MEAN FLOW VELOCITY VERSUS SURFACE NORMAL DISTANCE NONDIMENSIONALIZED BY COMPUTED BOUNDARY LAYER THICKNESS AT CHORD LOCATIONS ON UPPER SURFACE ( $\alpha = 7.5^\circ$ )

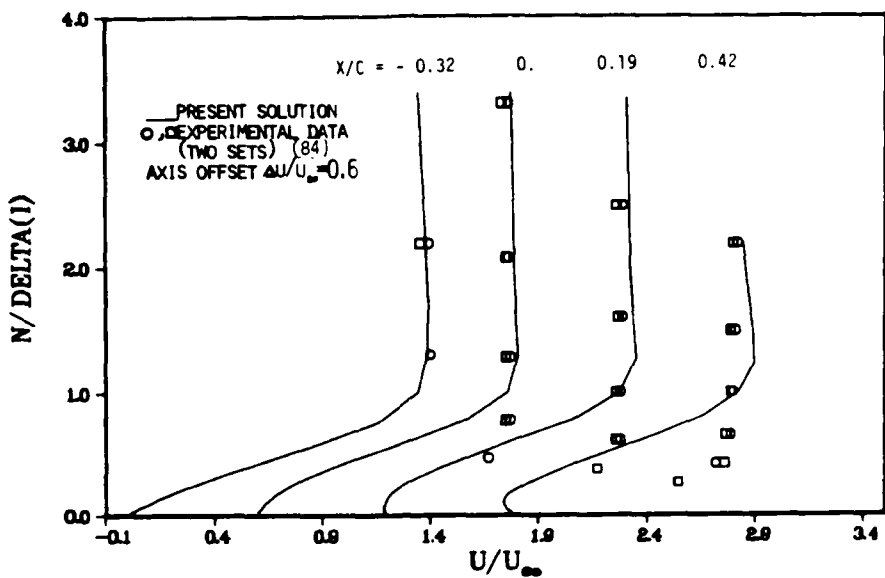


FIGURE 22 MEAN FLOW VELOCITY VERSUS SURFACE NORMAL DISTANCE NONDIMENSIONALIZED BY COMPUTED BOUNDARY LAYER THICKNESS AT CHORD LOCATIONS ON UPPER SURFACE ( $\alpha = 9.5^\circ$ )

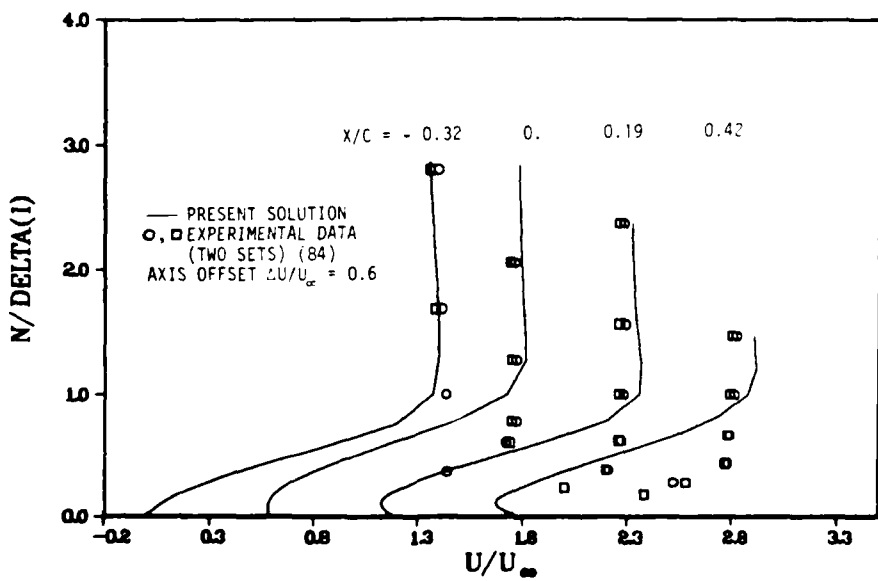


FIGURE 23 MEAN FLOW VELOCITY VERSUS SURFACE NORMAL DISTANCE NONDIMENSIONALIZED BY COMPUTED BOUNDARY LAYER THICKNESS AT CHORD LOCATIONS ON UPPER SURFACE ( $\alpha = 11.5^\circ$ )

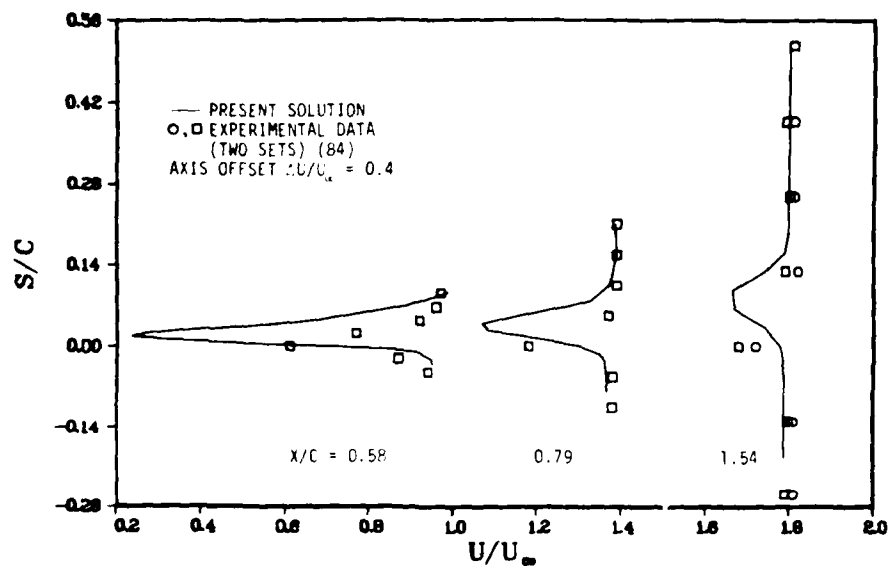


FIGURE 24 WAKE MEAN FLOW VELOCITY PROFILES AT CHORD LOCATIONS WITH ORIGIN ON CHORDLINE ( $\alpha = 5^\circ$ )

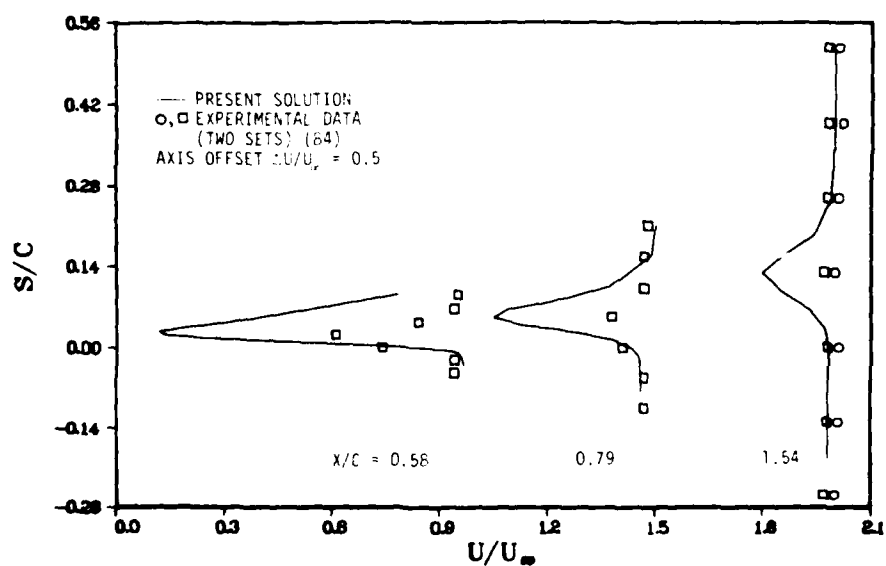


FIGURE 25 WAKE MEAN FLOW VELOCITY PROFILES AT CHORD LOCATIONS WITH ORIGIN ON CHORDLINE ( $\alpha = 7.5^\circ$ )

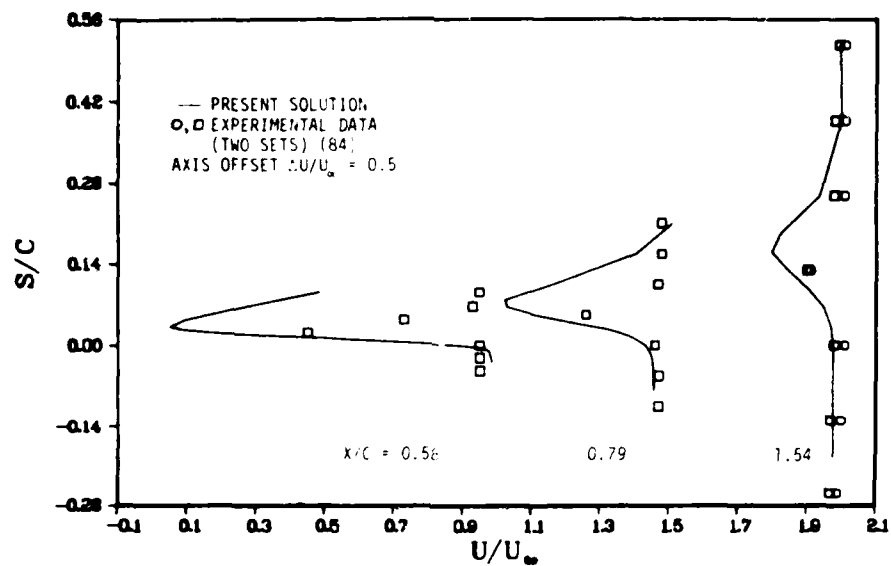


FIGURE 26 WAKE MEAN FLOW VELOCITY PROFILES AT CHORD LOCATIONS WITH ORIGIN ON CHORDLINE ( $\alpha = 9.5^\circ$ )

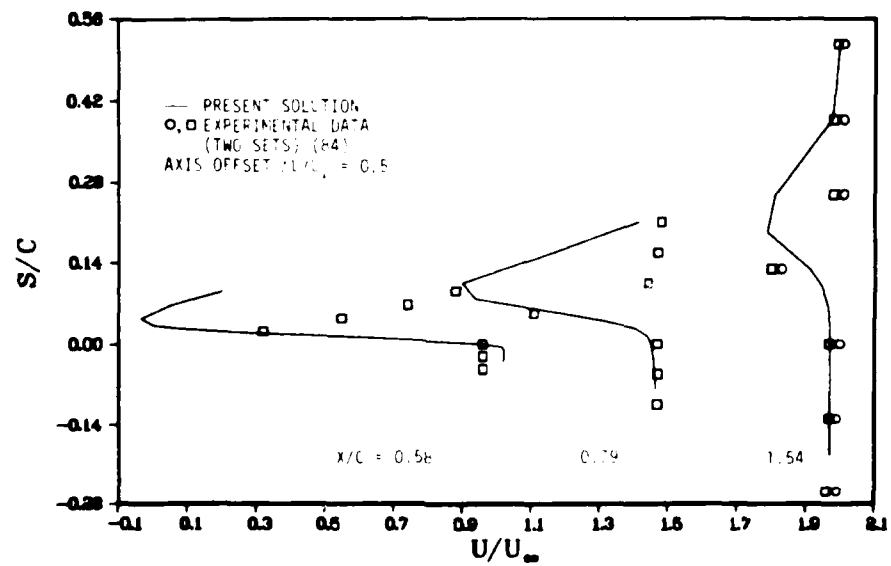


FIGURE 27 WAKE MEAN FLOW VELOCITY PROFILES AT CHORD LOCATIONS WITH ORIGIN ON CHORDLINE ( $\alpha = 11.5^\circ$ )

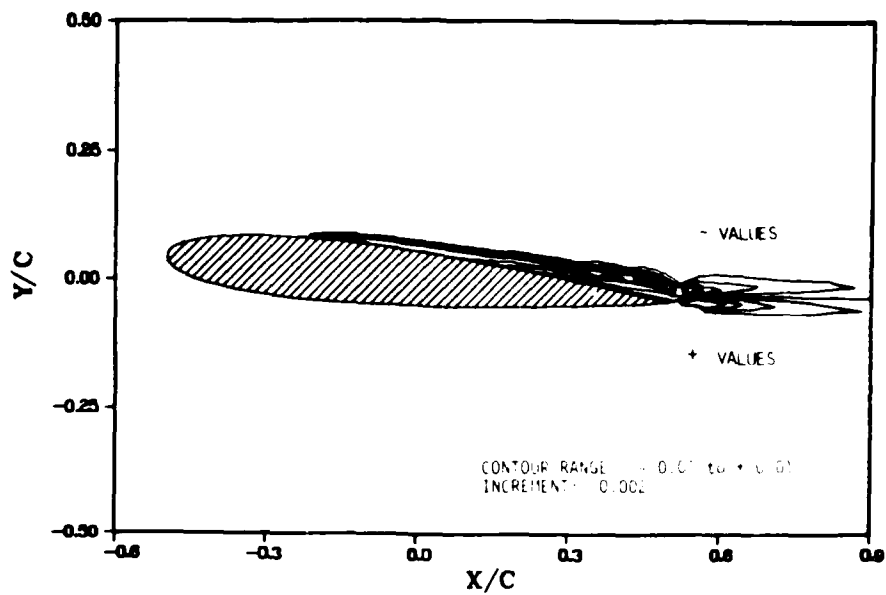


FIGURE 28 REYNOLDS STRESS  $\bar{U}'\bar{V}'$  CONTOURS ( $\alpha = 5^\circ$ )

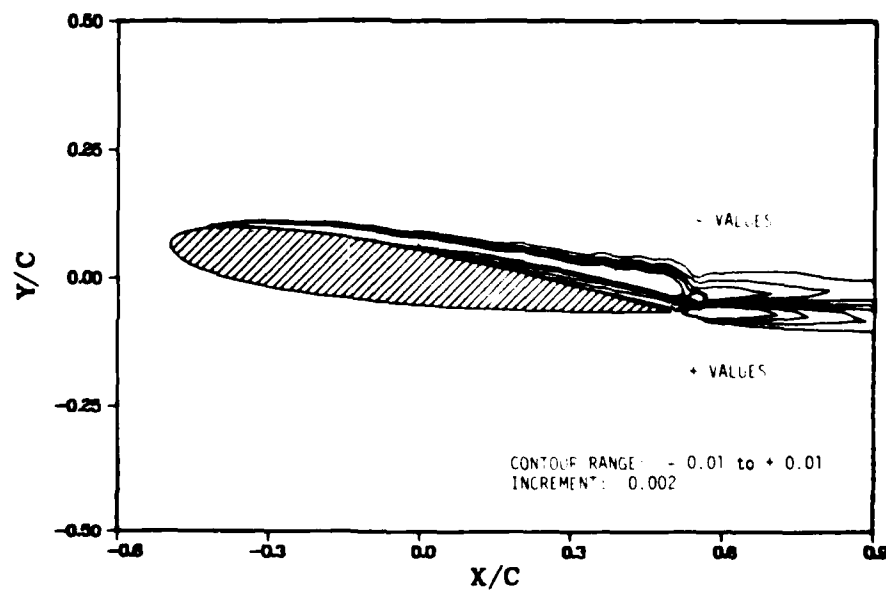


FIGURE 29 REYNOLDS STRESS  $\bar{U}'\bar{V}'$  CONTOURS ( $\alpha = 7.5^\circ$ )

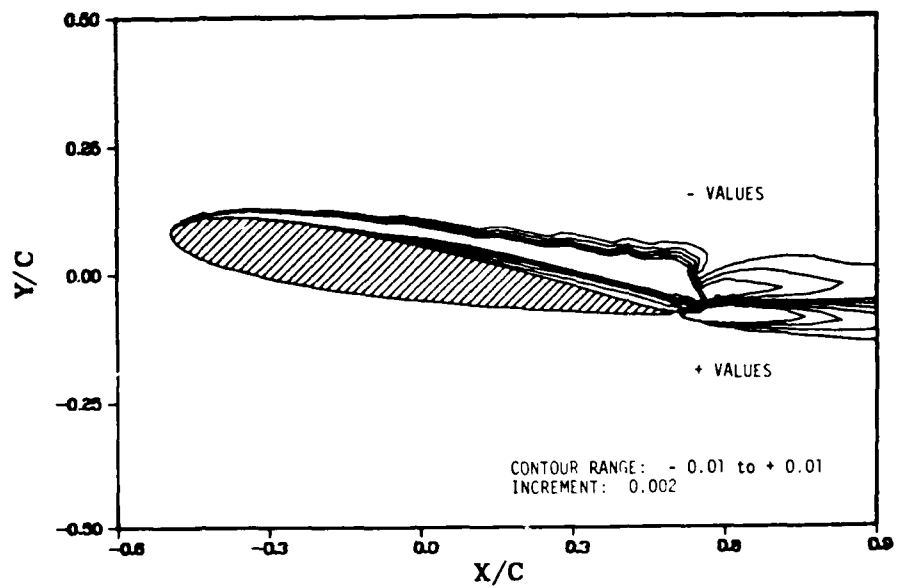


FIGURE 30 REYNOLDS STRESS  $\bar{U}'\bar{V}'$  CONTOURS ( $\alpha = 9.5^\circ$ )

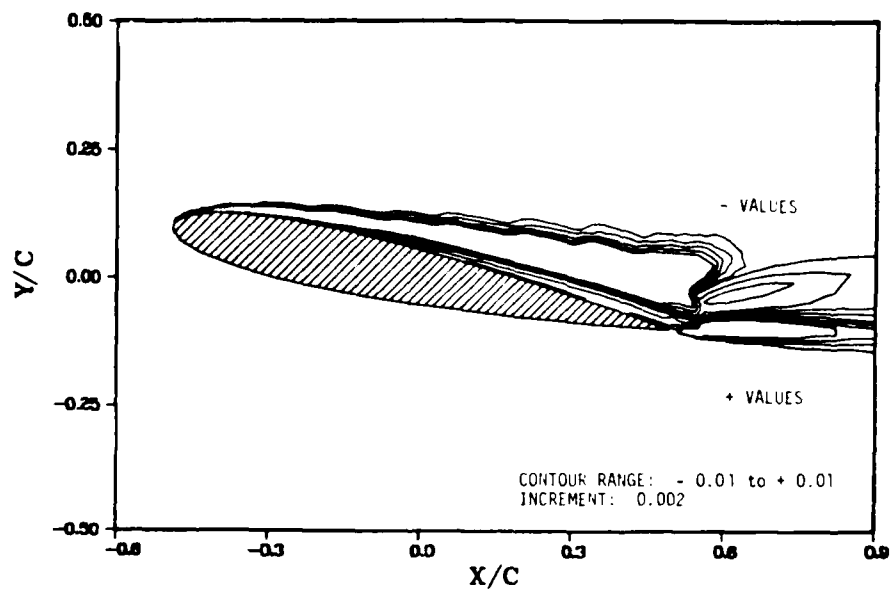


FIGURE 31 REYNOLDS STRESS  $\bar{U}'\bar{V}'$  CONTOURS ( $\alpha = 11.5^\circ$ )



Figure 31. Contour plots of double correlations  $\langle u'u' \rangle / (q_{ref})^2$ ,  $\langle u'v' \rangle / (q_{ref})^2$ , and  $\langle v'v' \rangle / (q_{ref})^2$ . Contour interval 0.01 or 0.005.

FIGURE 32 EXPERIMENTAL REYNOLDS STRESS  $\bar{u}'\bar{v}'$  CONTOURS FOR NACA 4412 AIRFOIL  
( $\alpha = 14^\circ$  AND  $Re = 1.5 \times 10^6$ ), REF. 96

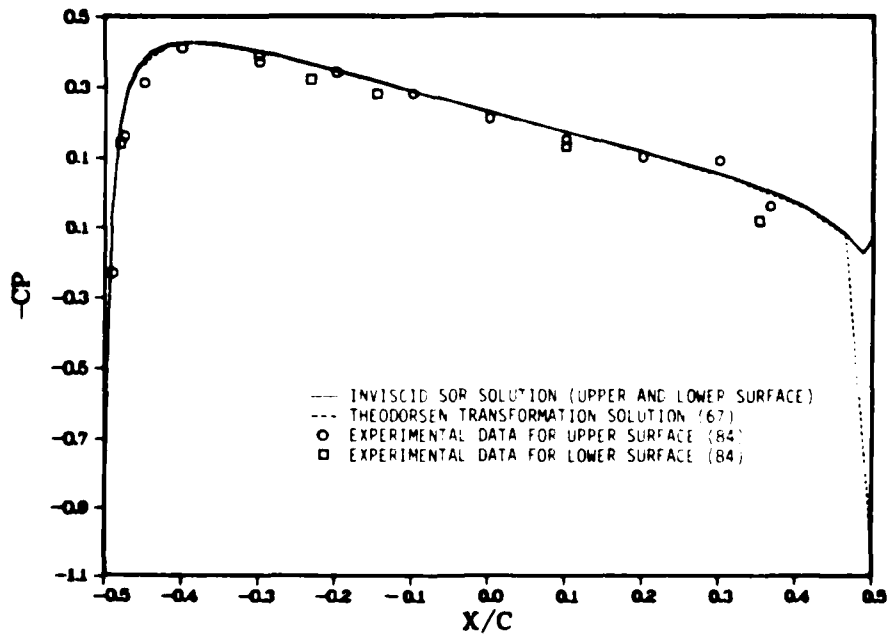


FIGURE 33 SURFACE MEAN PRESSURE COEFFICIENTS COMPARING NUMERICAL INVISCID METHODS WITH EXPERIMENTAL DATA AT  $\alpha = 0^\circ$

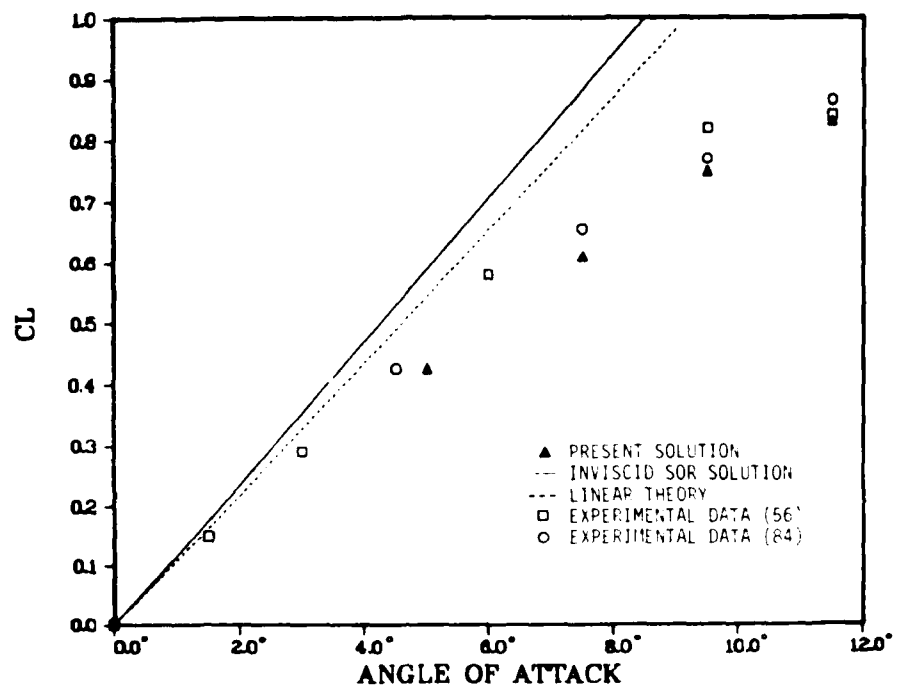


FIGURE 34 LIFT COEFFICIENT CURVE

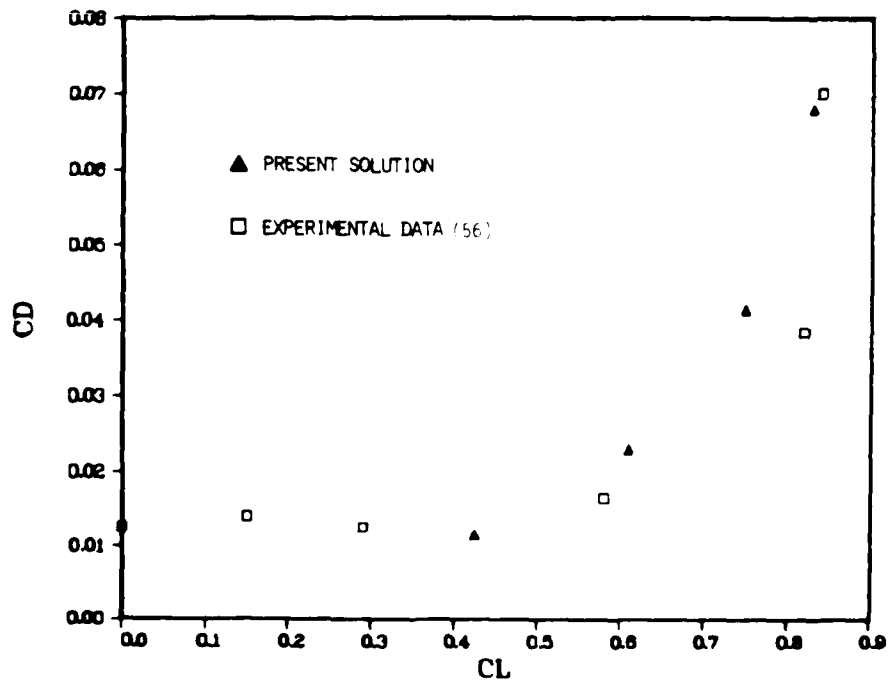


FIGURE 35 DRAG POLAR CURVE

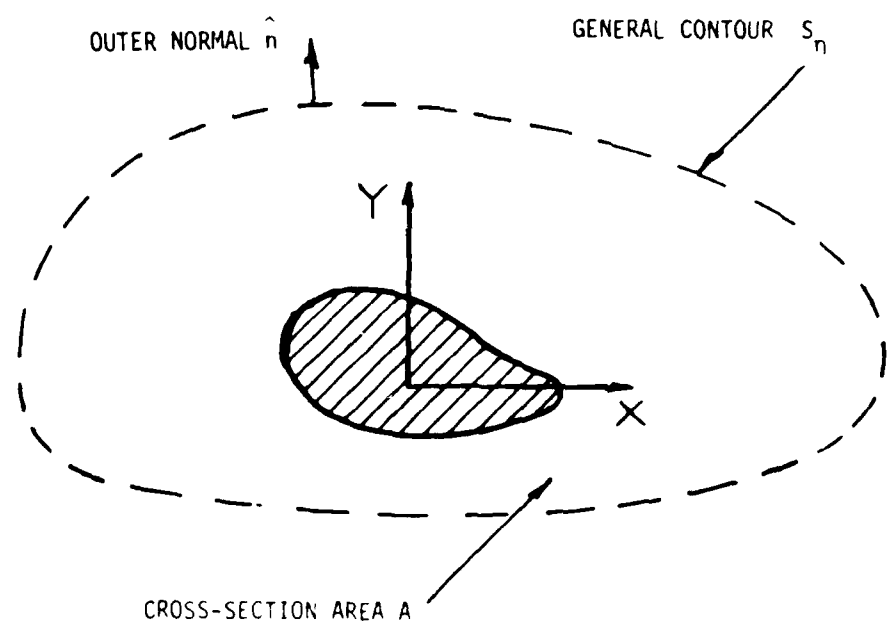


FIGURE 36 CONTOUR INTEGRATION GEOMETRY FOR TWO-DIMENSIONAL FLOW

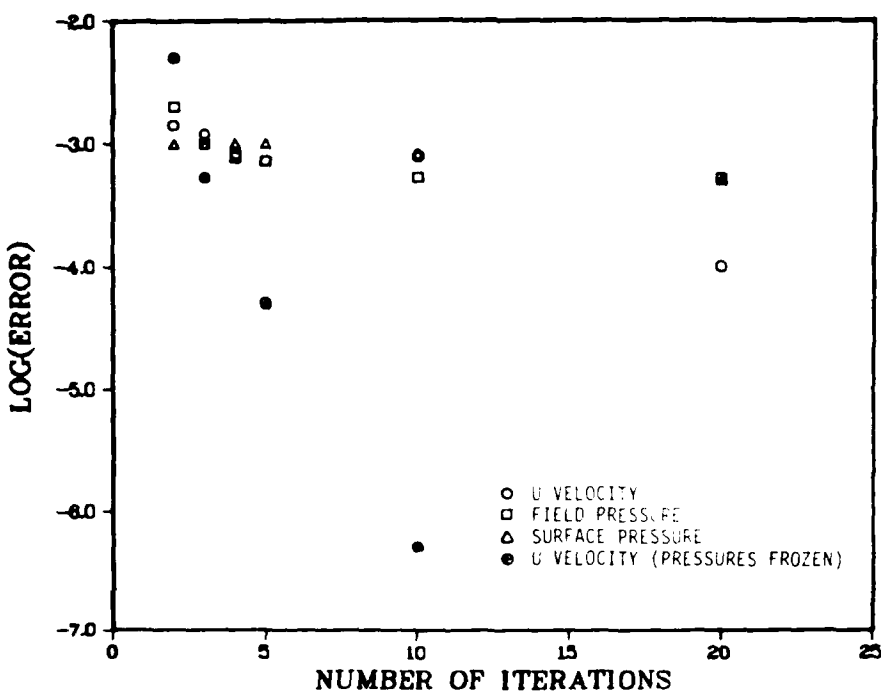


FIGURE 3.7 MAXIMUM ERROR OF SOR SOLUTION FOR U, P, AND  $P_b$  VERSUS NUMBER OF ITERATIONS WITH  $\Delta t = 0.0005$  AND  $\alpha = 8^\circ$

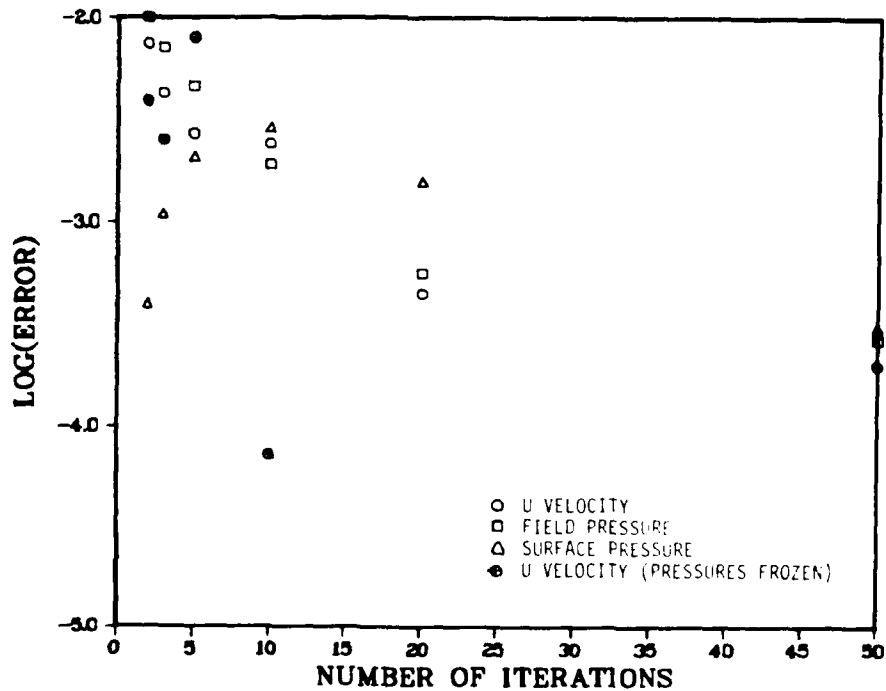


FIGURE 3.8 MAXIMUM ERROR OF SOR SOLUTION FOR U, P, AND  $P_b$  VERSUS NUMBER OF ITERATIONS WITH  $\Delta t = 0.001$  AND  $\alpha = 8^\circ$

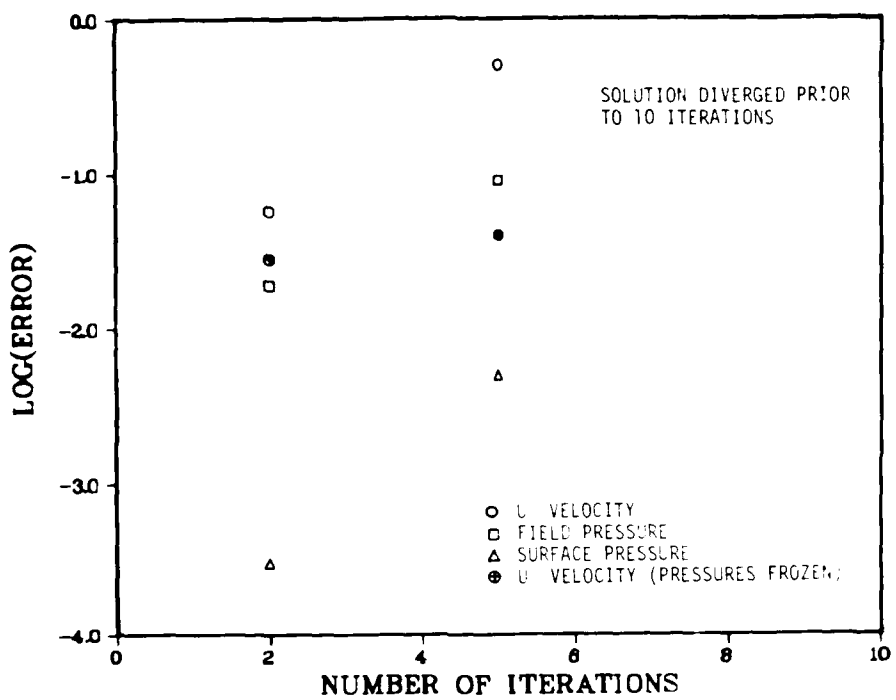


FIGURE 39 MAXIMUM ERROR OF SOR SOLUTION FOR U, P, AND  $P_b$  VERSUS NUMBER OF ITERATIONS WITH  $\Delta t = 0.005$  AND  $\alpha = 8^\circ$

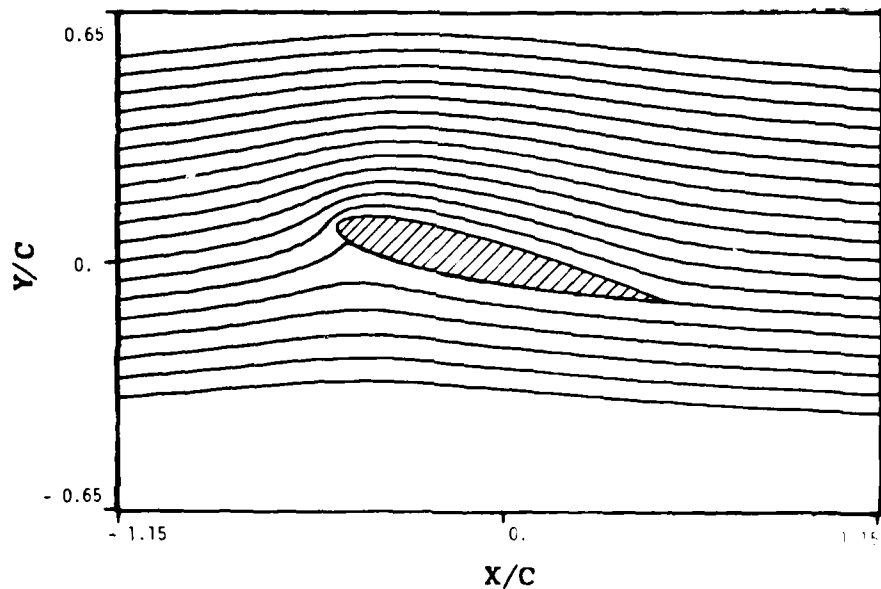


FIGURE 40 INVISCID FLOW STREAMLINE CONTOURS ( $\alpha = 11.5^\circ$ )

## APPENDIX A

### GRID TRANSFORMATION RELATIONSHIPS

Several of the definitions and coordinate transformation relations in the transformed plane are summarized below. The notation used by Thames (44) and Hodge (53) is retained. The physical plane is the  $(x, y)$  coordinate system and the computational plane is the  $(\xi, \eta)$  coordinate system. The following function definitions are used:

$f(x, y, t)$  - a twice differentiable scalar function.

$\underline{F}(x, y, t) = i F_1(x, y, t) + j F_2(x, y, t)$  a twice differentiable vector function where  $i$  and  $j$  are Cartesian unit vectors.

#### Transformation Definitions

$$r = \sqrt{x_r^2 + y_r^2} \quad (A.1)$$

$$\xi = x_r \frac{\partial}{\partial x} + y_r \frac{\partial}{\partial y} \quad (A.2)$$

$$\eta = x_r^2 + y_r^2 \quad (A.3)$$

$$D_1 = (\alpha x_{rr} - 2\beta x_{r\xi} + \gamma x_{\xi\xi}) \quad (A.4)$$

$$D_2 = (\alpha y_{rr} - 2\beta y_{r\xi} + \gamma y_{\xi\xi}) \quad (A.5)$$

$$J = x_r y_{r\xi} - x_{r\xi} y_r \quad (A.6)$$

$$\sigma = (y_r D_1 - x_r D_2)/J \quad (A.7)$$

$$\tau = (x_r D_2 - y_r D_1)/J \quad (A.8)$$

#### Derivatives of Scalar Functions in Transformed Plane

$$f_x = \frac{\partial f}{\partial x} = (y_r f_\xi - y_\xi f_r)/J \quad (A.9)$$

$$f_y = \frac{\partial f}{\partial y} = (x_r f_\xi - x_\xi f_r)/J \quad (A.10)$$

$$f_t = \frac{\partial f}{\partial t} = (\partial f / \partial t)_{\xi, r} \text{ for fixed coordinates} \quad (A.11)$$

### Vector Operators in the Transformed Plane

Gradient:

$$\underline{\nabla} f = [(y_r f_\xi - y_\xi f_r) \hat{i} + (x_r f_\xi - x_\xi f_r) \hat{j}] / J \quad (\text{A.12})$$

Divergence:

$$\underline{\nabla} \cdot \underline{F} = [y_r (F_1)_\xi - y_\xi (F_1)_r + x_r (F_2)_\xi - x_\xi (F_2)_r] / J \quad (\text{A.13})$$

Curl:

$$\underline{\nabla} \times \underline{F} = k [y_r (F_2)_\xi - y_\xi (F_2)_r - x_\xi (F_1)_\xi + x_r (F_1)_\xi] / J \quad (\text{A.14})$$

Laplacian:

$$\nabla^2 f = [(f_{\xi\xi} - 2f_{\xi r} + f_{rr}) / J^2 + (\epsilon/J^2) f_r + (\epsilon/J^2) f_\xi] \quad (\text{A.15})$$

### Unit Normal and Tangent Vectors in Physical Plane

Normal to  $\tau$  line:

$$\underline{n}^{(\tau)} = \underline{\tau}_r / |\underline{\tau}| = (-y_\xi \hat{i} + x_\xi \hat{j}) / \sqrt{-\epsilon} \quad (\text{A.16})$$

Normal to  $\xi$  line:

$$\underline{n}^{(\xi)} = \underline{\xi}_r / |\underline{\xi}| = (y_r \hat{i} - x_r \hat{j}) / \sqrt{-\epsilon} \quad (\text{A.17})$$

Tangent to  $\tau$  line (increasing  $\xi$  direction):

$$\underline{t}^{(\tau)} = \underline{n}^{(\tau)} \times \hat{k} = (x_\xi \hat{i} + y_\xi \hat{j}) / \sqrt{-\epsilon} \quad (\text{A.18})$$

Tangent to  $\xi$  line (increasing  $\tau$  direction):

$$\underline{t}^{(\xi)} = -\underline{n}^{(\xi)} \times \hat{k} = (x_r \hat{i} + y_r \hat{j}) / \sqrt{-\epsilon} \quad (\text{A.19})$$

### Integrals in the Transformed Plane

Area Integral:

$$\int_R f(x, y) dx dy = \int_{R^*} f(x(\xi, \tau), y(\xi, \tau)) |J| dA \quad (\text{A.20})$$

where  $R^*$  is the region  $R$  mapped into the  $(\xi, \tau)$  plane.

Vector Line Integral:

$$\int_{s_r} \underline{F}(x, y) ds = \int_{\xi_{\min}}^{\xi_{\max}} \underline{F}(x(\xi, r_p), y(\xi, r_p)) \cdot \overline{\gamma} d\xi \quad (A.21)$$

where contour  $s_r$  is any constant  $r$  line in the physical plane,  $s$  is arclength along  $s_r$ , and  $r_p$  is the value of  $r$  for the chosen contour  $s_r$ .

## APPENDIX B

FINITE DIFFERENCE APPROXIMATIONS

This appendix presents the finite difference approximations that are used in this investigation. The differences are formulated using a function  $f(\xi, \tau)$  in the computational or transformed plane. The  $\xi$  and  $\tau$  spacings are assumed constant with value unity. The truncation error term is given in derivative form assuming  $\Delta\xi$  and  $\Delta\tau$  are equal. The approximations are second order accurate unless otherwise specified. Time differences are expressed by  $\Delta t$ . The superscript  $n$  denotes the  $n^{\text{th}}$  time interval and is understood when omitted. The differences are given for a  $(\xi, \tau)$  point location denoted by subscripts  $(i, j)$  and are understood when omitted. Space derivatives with respect to only  $\xi$  are presented because the corresponding  $\tau$  derivatives are identical with subscripts  $(i, j)$  reversed.

First time derivative, backward difference, first order:

$$f_{t^-} = (f^n - f^{n-1})/\Delta t - \Delta t f_{tt}/2 + \dots \quad (\text{B.1})$$

First derivative, backward difference, first order:

$$f_{\tau^-} = (f_j - f_{j-1}) - f_{\tau\tau}/2 + \dots \quad (\text{B.2})$$

First derivative, central difference:

$$f_{\tau} = (f_{j+1} - f_{j-1})/2 - f_{\tau\tau\tau}/6 + \dots \quad (\text{B.3})$$

First derivative, forward difference:

$$f_{\tau} = (-f_{j+2} + 4f_{j+1} - 3f_j) - f_{\tau\tau\tau}/3 + \dots \quad (\text{B.4})$$

First derivative, backward difference:

$$f_{\tau} = (f_{j-2} - 4f_{j-1} + 3f_j) + f_{\tau\tau\tau}/3 + \dots \quad (\text{B.5})$$

Second derivative, central difference:

$$f_{nn} = (f_{j+1} - 2f_j + f_{j-1}) - f_{rrr}/12 + \dots \quad (B.6)$$

Second derivative, forward difference:

$$f_{rrr} = (-f_{j+3} + 4f_{j+2} - 5f_{j+1} + 2f_j) + 11f_{rrr}/12 + \dots \quad (B.7)$$

Second derivative, backward difference:

$$f_{rrr} = (f_{j-3} - 4f_{j-2} + 5f_{j-1} - 2f_j) - 11f_{rrr}/12 + \dots \quad (B.8)$$

Cross derivative, central difference:

$$\begin{aligned} f_{\xi n} = & (f_{i+1, j+1} - f_{i+1, j-1} + f_{i-1, j-1} - f_{i-1, j+1})/4 \\ & - (f_{\xi \xi n} + f_{\xi r n})/24 + \dots \end{aligned} \quad (B.9)$$

Cross derivative, central in  $\xi$  and forward in  $n$  differences:

$$\begin{aligned} f_{\xi n} = & \{-3(f_{i+1} - f_{i-1}) + 4(f_{i+1, j+1} - f_{i-1, j+1}) \\ & - (f_{i+1, j+2} - f_{i-1, j+2})\}/4 + (f_{\xi \xi n} + f_{\xi r n})/6 + \dots \end{aligned} \quad (B.10)$$

Cross derivative, central in  $\xi$  and backward in  $n$  differences:

$$\begin{aligned} f_{\xi n} = & \{3(f_{i+1} - f_{i-1}) - 4(f_{i+1, j-1} - f_{i-1, j-1}) \\ & + (f_{i+1, j-2} - f_{i-1, j-2})\}/4 - (f_{\xi \xi n} + f_{\xi r n})/6 + \dots \end{aligned} \quad (B.11)$$

## APPENDIX C

### GRID MODIFICATION FOR WAKE RESOLUTION

This appendix describes the technique that is used to insert additional grid lines in the region of the airfoil wake. The body-fitted coordinate grid system becomes coarse at distances far from the body. The coarse grid may reduce the resolution of the velocity defect in the viscous far wake region. In order to increase wake resolution, eight additional  $\xi$  lines are placed downstream of the airfoil with body points on the rounded trailing edge. The original numerically generated grid has 71  $\xi$  and 44  $\eta$  lines. Linear interpolation between adjoining  $\xi$  lines of the form  $x_p(I, J) = \{x(I-1, J) + x(I, J)\}/2$  is used to locate a  $\xi$  line between lines  $I = 1$  and  $I = 2$ ,  $I = 2$  and  $I = 3$ ,  $I = 69$  and  $I = 70$ , and  $I = 70$  and  $I = 71$ . The procedure is repeated using the new lines as well except only one additional line is located below the  $I = 1$  cut. In this way the fine grid spacing has an asymmetry for better wake resolution at angle of attack. The final 79 by 44 grid is shown in Figure 3. Table C.I gives the numbered I index ( $\xi$  line) designation for the grid systems in the wake region.

TABLE C.I

## I Index (' Line) Designation for Grid Systems in Wake

71 x 44 System	75 x 44 System	79 x 44 System
69	71	72
-	72	73
-	-	74
70	73	75
-	-	76
-	74	77
-	-	78
71, 1	75, 1	79, 1
-	-	2
-	2	3
2	3	4
-	4	5
3	5	6

## APPENDIX D

### CONTOUR INTEGRAL METHOD FOR DETERMINING BODY FORCE COEFFICIENTS

The determination of the resultant force that a flow field exerts on a body usually involves the calculation of surface pressure and viscous stresses and the summation of these forces over the body surface. An alternate approach is to apply a control volume analysis to a region enclosing the body. In the foregoing discussion, a control volume analysis for a body in a two dimensional flow is presented.

Consider a general body immersed in a flow field with surface  $\sigma_B$ . Define a fixed control volume V with outer surface  $\sigma_r$  and inner surface  $\sigma_B$ . Conservation of linear momentum for the fluid in V is expressed by the Cauchy Integral Equation of Motion

$$\frac{D}{Dt} \int_V \rho v \, dV = \int_V \rho b \, dV + \int_{\sigma} n \cdot T \, ds \quad (D.1)$$

where  $\rho$  is the density,  $v$  velocity field,  $b$  body force per unit mass,  $n$  unit outward surface normal vector,  $T$  traction stress, and  $\sigma$  is the total surface  $\sigma_B + \sigma_r$ . Apply the Reynolds Transport Theorem to the material derivative term and the Divergence Theorem to the surface integral and obtain from Equation D.1 for the  $i^{\text{th}}$  Cartesian vector component

$$\int_V \frac{\partial}{\partial t} (\rho v_i) \, dV + \int_V \delta_j (\rho v_i v_j - T_{ji}) \, dV = 0 \quad (D.2)$$

Apply the Divergence Theorem to the second volume integral and express the resulting surface integral as separate integrals over  $\sigma_B$  and  $\sigma_r$  to obtain

$$\int_V \frac{\partial}{\partial t} (\rho v_i) dV + \int_{C_B} n_j (\rho v_i v_j - T_{ji}) ds + \int_{C_r} n_j (\rho v_i v_j - T_{ji}) ds = 0 \quad (D.3)$$

Now, on the solid non-porous body surface  $C_B$ ,  $n_j v_j = 0$ . The integral of the resultant traction force over  $C_B$  is the net force exerted by the body on the control volume fluid. Therefore, the force  $F$  exerted by the fluid on the body is given by

$$F_i = - \int_{C_B} n_j T_{ji} ds \quad (D.4)$$

Substitute Equation D.4 into D.3 and use the above surface condition to obtain a general expression for the force exerted by the fluid on the body.

$$F_i = - \frac{\partial}{\partial t} \int_V \rho v_i dV + \int_{C_r} n_j (T_{ji} - \rho v_i v_j) ds \quad (D.5)$$

Now consider the case of two-dimensional flow in the x-y plane. Then Equation D.5 becomes the following expression for the force per length of span  $f$

$$f_i = - \frac{\partial}{\partial t} \int_A \rho v_i dA + \int_{S_r} n_j (T_{ji} - \rho v_i v_j) ds \quad (D.6)$$

where  $A$  is the cross sectional area of the control volume and  $S_r$  is the outer perimeter of  $A$  as shown in Figure 36.

Substitute for the traction stress  $T_{ji} = -p_{ji} + \tau_{ji}$  in Equation D.6 and obtain

$$f_i = \int_{S_r} n_j (-p_{ji} + \tau_{ji} - \rho v_i v_j) ds - \frac{\partial}{\partial t} \int_A \rho v_i dA \quad (D.7)$$

where  $p$  is the pressure,  $\tau_{ji}$  is the laminar viscous stress and  $\delta_{ij}$  is the Kronecker Delta Function. Next express the flow variables in terms of turbulent mean and fluctuating variables, assume incompressible flow, and Reynolds average Equation D.7 to obtain

$$\bar{f}_i = \int_{S_i} n_j (-\bar{p})_{ji} + \bar{\tau}_{ji} - (\bar{v}_i \bar{v}_j + \bar{v}'_i \bar{v}'_j) ds - \frac{1}{\tau_t} \int_A \bar{v}_i dA \quad (D.8)$$

The term  $-\bar{v}'_i \bar{v}'_j$  is the turbulent Reynolds stress  $\bar{\tau}_{tji}$ . Let the total stress be defined as  $\bar{\tau}_{tji} = \bar{\tau}_{ji} + \bar{\tau}_{tji}$ . Then Equation D.8 becomes

$$\bar{f}_i = \int_{S_i} n_j (-\bar{p})_{ji} + \bar{\tau}_{tji} - (\bar{v}_i \bar{v}_j) ds - \frac{1}{\tau_t} \int_A \bar{v}_i dA \quad (D.9)$$

Introduce the following nondimensional variables in Equation D.9

$\bar{p} = \frac{\bar{p} - p_\infty}{U_\infty}$ ,  $\bar{v}_i = \frac{\bar{v}_i}{U_\infty}$ ,  $x_i = \frac{x_i}{L}$ , and  $t = \frac{tU_\infty}{L}$ , and note that  $\bar{\tau}_{tji} = \frac{L}{U_\infty} \bar{\tau}_{tji}$  where  $U_\infty$  is the freestream velocity and  $L$  is a reference length in the  $x$  direction. Also, define the force coefficient  $C_{f_i} = \frac{\bar{f}_i}{\rho U_\infty^2 L}$  and obtain from Equation D.9

$$C_{f_i} = 2 \int_{S_i} n_j (-\bar{p})_{ji} + \frac{1}{\tau_t} L \bar{\tau}_{tji} - (\bar{v}_i \bar{v}_j) ds - 2 \frac{1}{\tau_t} \int_A \bar{v}_i dA \quad (D.10)$$

where all variables are understood to be mean dimensionless variables. Now the turbulent eddy viscosity concept is used where

$$\bar{\tau}_{tji} = C_M \cdot (\bar{v}_i \bar{v}_j + \bar{v}'_i \bar{v}'_j)$$

$$= C_M \frac{U_\infty L}{M}$$

and define  $Re_t = \frac{U_\infty L}{M}$  which transforms Equation D.10 to the following

$$C_{f_i} = 2 \int_{S_i} n_j (-\bar{p})_{ji} + \frac{1}{Re_t} (C_M \bar{v}_i \bar{v}_j + \bar{v}'_i \bar{v}'_j) - (\bar{v}_i \bar{v}_j) ds - 2 \frac{1}{\tau_t} \int_A \bar{v}_i dA \quad (D.11)$$

Expand Equation D.11 into  $x$  and  $y$  component equations

$$C_{f_x} = 2 \int_{S_r} (-n_1 p + \frac{1}{Re_t} [2n_1 \frac{\partial u}{\partial x} + n_2 (\frac{\partial u}{\partial y} + \frac{\partial v}{\partial x})] - (u n_1 + v n_2) ds$$

$$= 2 \frac{1}{Re_t} \int_A u dA \quad (D.12a)$$

$$C_{f_y} = 2 \int_{S_r} (-n_2 p + \frac{1}{Re_t} [n_1 (\frac{\partial u}{\partial y} + \frac{\partial x}{\partial x}) + 2n_2 \frac{\partial v}{\partial y}] - (u v n_1 + v^2 n_2) ds$$

$$= 2 \frac{1}{Re_t} \int_A v dA \quad (D.12b)$$

where  $n_1$  and  $n_2$  are the x and y components of the unit outward normal vector  $n$  for the outer boundary  $s_r$  of area A. Equations (D.12a) and (D.12b) are expressions for the x and y force coefficients exerted by a two-dimensional incompressible turbulent flow on an arbitrary two-dimensional body where path  $s_r$  encloses the body and an eddy viscosity method is used to model turbulence.

Lift and drag coefficients are then obtained from the force coefficients as follows where  $\alpha$  is the geometric angle of attack.

$$C_L = C_{f_y} \cos \alpha - C_{f_x} \sin \alpha \quad (D.13)$$

$$C_D = C_{f_y} \sin \alpha + C_{f_x} \cos \alpha \quad (D.14)$$

## APPENDIX E

### TIME INCREMENT INFLUENCE ON SOR CONVERGENCE

Implicit SOR methods have been shown by linear stability analyses to be unconditionally stable. However, convergence has required a small time step size in this investigation and elsewhere. The following analysis indicates the relationship between the time step size and convergence.

Consider the system of difference equations to be written in the following matrix form:

$$AU = b \quad (E.1)$$

where A is the coefficient matrix, U is the vector of unknown primitive variables at time step n with u, v, p grouped together for each (i,j) point location, and b is a vector of "constants". For example, the x component of the momentum equation, Equation 92, at the (i,j) point is

$$\begin{aligned} Q u_{ij}^{(s)} &= u_{ij}^{n-1} + \Delta t [-YETA (p_{i+1,j} - p_{i-1,j}) + YXI (p_{i,j+1} - p_{i,j-1}) \\ &+ VC_1 (4u_{IC1,j} - u_{IC2,j}) + VC_2 (4u_{i,JC1} - u_{i,JC2}) + UV_1 (4u_{IV1,j} - \\ &u_{IV2,j}) + UV_2 (4u_{i,JV1} - u_{i,JV2}) + \frac{1}{RET} (\ALFA (u_{i+1,j} + u_{i-1,j}) \\ &+ \GAMA (u_{i,j+1} + u_{i,j-1}) + \BETA (u_{i+1,j+1} - u_{i+1,j-1} + u_{i-1,j+1} - \\ &u_{i-1,j-1})) - u_{ij}^{(s-1)} - p] \end{aligned} \quad (E.2)$$

where all coefficients are evaluated at point (i,j) and primitive variables are at time step n unless given otherwise, and Q is given by

$$Q = 1 + 3 \Delta t (VC_1 + VC_2 + UV_1 + UV_2) + \frac{2}{RET} (\ALFA + \GAMA)$$

Rearrange Equation E.2 and obtain

$$-VC_1 u_{IC2,j} - UV_1 u_{IV2,j} + \frac{\BETA}{RET} u_{i-1,j-1} + 4VC_1 u_{IC1,j} + 4UV_1 u_{IV1,j}$$

$$\begin{aligned}
& + \frac{\text{ALFA}}{\text{RET}} u_{i-1,j} + \text{YETA } p_{i-1,j} - \frac{\text{BETA}}{\text{RET}} u_{i-1,j+1} = \text{VC } u_i \text{ JC2} - \text{VV } u_i \text{ JV2} \\
& + \frac{\text{GAMA}}{\text{RET}} u_{i,j-1} + 4 \text{ VC } u_i \text{ JC1} + 4 \text{ VV } u_i \text{ JV1} - \text{YXI } p_i \text{ j-1} - \frac{Q}{\Delta t} u_{ij}^{(s)} \\
& + \frac{\text{GAMA}}{\text{RET}} u_{i,j+1} + \text{YXI } p_i \text{ j+1} - \frac{\text{BETA}}{\text{RET}} u_{i+1,j-1} + \frac{\text{ALFA}}{\text{RET}} u_{i+1,j} - \text{YEIA } p_{i+1,j} \\
& + \frac{\text{BETA}}{\text{RET}} u_{i+1,j+1} = - \frac{u_{ij}^{n-1}}{\Delta t} + u_{ij}^{(s-1)} D
\end{aligned} \tag{E.3}$$

A similar y component of momentum equation is obtained if u is replaced by v; - YETA by YEIA; and YXI by - XI.

The finite difference pressure Equation 94 becomes

$$\begin{aligned}
& - \text{UV } p_{IV2,j} + \text{BETA } p_{i-1,j-1} + 4 \text{ UV } p_{IV1,j} + \text{ALFA } p_{i-1,j} \\
& - \text{BETA } p_{i-1,j+1} - \text{VV } p_i \text{ JV2} + \text{GAMA } p_i \text{ j-1} + 4 \text{ VV } p_i \text{ JV1} - B p_{ij} \\
& + \text{GAMA } p_i \text{ j+1} - \text{BETA } p_{i+1,j-1} + \text{ALFA } p_{i+1,j} + \text{BETA } p_{i+1,j+1} = -\text{RHS}
\end{aligned} \tag{E.4}$$

where  $B=2(\text{ALFA}+\text{GAMA}) + 3(\text{UV} + \text{VV})$  and  $\text{RHS} = -\frac{D^{n-1}}{\Delta t} + [(\text{UX})^2 + 2(\text{VX})(\text{UY}) + (\text{VY})^2]$

Convergence theorems (81) for systems of linear equations with constant coefficients show that a necessary and sufficient condition for convergence requires that the coefficient matrix be diagonally dominant. If this criteria is applied to the above quasi-linear system, the following convergence criteria, inequality E.6 from the momentum equation and inequality E.8 from the pressure equation, are obtained:

$$\begin{aligned}
& 5(\text{UC} + \text{VC} + \text{UV} + \text{VV}) + \frac{2}{\text{RET}}(\text{ALFA} + \text{GAMA}) \\
& + \frac{3}{\text{RET}} \text{BETA} + 2(\text{YXI} + \text{YETA}) < \frac{Q}{\Delta t} \\
\text{or } & 3(\text{UC} + \text{VC} + \text{UV} + \text{VV}) + \frac{2}{\text{RET}}(\text{ALFA} + \text{GAMA}) + \frac{1}{\Delta t}
\end{aligned} \tag{E.5}$$

which becomes

$$\Delta t \cdot 2(\text{UC} + \text{VC} + \text{UV} + \text{VV}) + \frac{3}{\text{RET}} \text{BETA} + 2(\text{YXI} + \text{YETA}) < 1 \tag{E.6}$$

and

$$2(|\text{ALFA}| + |\text{GAMA}|) + 4|\text{BETA}| + 5(|\text{UV}| + |\text{VV}|) < 0 \\ 2(|\text{ALFA}| + |\text{GAMA}|) + 3(|\text{UV}| + |\text{VV}|) \quad (\text{E.7})$$

$$\text{or } 4|\text{BETA}| + 2(|\text{UV}| + |\text{VV}|) < 0 \quad (\text{E.8})$$

The convergence criteria, Equation E.6, provides a limit on  $\Delta t$  as a function of both the grid geometry and flow field solution. The right hand side of the inequality has its smallest magnitude near the trailing edge and increases rapidly away from the airfoil. An order of magnitude analysis of the grid coefficients and an examination of the computational solutions indicate that diagonal dominance occurs if  $\Delta t < 0.0003$  for points near the trailing edge,  $\Delta t < 0.001$  elsewhere near the body, and  $\Delta t < 1$  in the far field. The pressure equation convergence criteria, Equation E.8, has no  $\Delta t$  dependence and is approximately satisfied only at points far from the body where the left hand side approaches zero. These criteria can only indicate a possible time step restriction since the system of equations has variable coefficients and lower order nonlinearities.

A numerical experiment was conducted to determine the time step effect on convergence. A computation for the flow over the NACA 0012 airfoil at an angle of attack of eight degrees was used. The solution was advanced one time step with the time step size and number of iterations per time step varied. The solution converged for time steps of 0.0005 and 0.001 while diverging for a time step of 0.005. The relative maximum error magnitudes for the u component of velocity, surface pressure  $p_b$ , and field pressure  $p$  as functions of number of iterations are shown for each time step in Figures 37, 38, and 39. The relative error is defined as  $(f_n - f_{n-1})/f_n$ . The v component of velocity errors behave similarly to the u component. Next, the pressure was held fixed and the convergence of the velocity was monitored (Figures 37, 38, and 39). The rapid rate of convergence is

observed. The u and v velocity components were also held fixed in turn to test convergence. In both cases, convergence was similar to the general solution case. These numerical experiments indicate that the convergence of pressure is slow and that convergence is dependent on time step sizes similar to those predicted by the simple analysis above.

## APPENDIX F

### FAR FIELD BOUNDARY CONDITIONS

The far field boundary for a numerical solution must usually be at a finite distance from the body of interest. This constraint may pose difficulties if the only known far field boundary conditions are those at infinity. This analysis uses complex variable methods for incompressible potential flow and develops approximate far field boundary conditions for use at a finite distance.

Consider a circular cylinder radius  $a$  and center at the origin, with positive clockwise circulation  $\Gamma$ , in a uniform stream (velocity  $U_\infty$ ), at angle of attack  $\alpha$ . This coordinate system is identical with the physical plane of the airfoil. The complex velocity is

$$\tilde{W}(\tilde{z}) = U_\infty e^{-iz\alpha} - \frac{(2\pi a^2 U_\infty)}{2\pi} \frac{e^{iz\alpha}}{\tilde{z}} + i \frac{\Gamma}{2\pi} \frac{1}{\tilde{z}} \quad (F.1)$$

where the first term is the uniform stream contribution, the second term is a doublet of strength  $2\pi a^2 U_\infty$ , and the third term is a vortex of strength  $\Gamma$ .

Next, use the Kutta-Joukowski Theorem for lift and the definition of the lift coefficient to obtain

$$\Gamma = (1/2) C_L U_\infty c \quad (F.2)$$

where  $c$  is the airfoil chord.

Nondimensionalize Equation F.1 velocities with the freestream velocity  $U_\infty$  and lengths with the airfoil chord  $c$  and substitute Equation F.2 into F.1 and obtain

$$W(z) = e^{-iz} - \left(\frac{a}{c}\right)^2 \frac{e^{iz}}{z^2} + i \frac{C_L}{4} \frac{1}{z} \quad (F.3)$$

where  $W$  is the nondimensional complex velocity and  $z$  is the nondimensional complex variable  $z = x + iy$ .

Airfoil transformations such as the Joukowski and Trefftz Transformations transform a cylinder into an airfoil with a chord of four radii. Thus, for a given chord  $c$ , choose the cylinder radius to be  $1/4$   $c$  which gives a scaling factor  $\frac{a}{c} = 1/4$  in the doublet. Then the complex velocity for the flow around the scaled cylinder becomes

$$W(z) = e^{-iz} - \frac{e^{iz}}{16z^2} + i \frac{C_L}{4} \frac{1}{z} \quad (F.4)$$

Expression F.4 can then be used to approximate the far field potential flow over the airfoil of chord  $c$  with circulation  $\Gamma$  in the same physical plane.

Let the far field boundary be a circle of radius  $r_f$  where  $z = r_f e^{i\theta}$ ,  $0 \leq \theta < 2\pi$ . Substitute for  $z$  in Equation F.4 and obtain

$$W_f(\theta) = e^{-i\theta} - \frac{e^{i\theta}}{16r_f^2} e^{-2i\theta} + i \frac{C_L}{4r_f} \frac{1}{r_f} e^{-i\theta} \quad (F.5)$$

Combine the exponential terms in F.5 and use the fact that  $W = u - iv$ ,

where  $u$  and  $v$  are the  $x$  and  $y$  velocity components, to obtain

$$u_f(\theta) = \cos \theta - \frac{1}{16r_f^2} \cos (\theta - 2\theta) + \frac{C_L}{4r_f} \sin \theta \quad (F.6a)$$

$$v_f(\theta) = \sin \theta + \frac{1}{16r_f^2} \sin (\theta - 2\theta) - \frac{C_L}{4r_f} \cos \theta \quad (F.6b)$$

In both Equations F.6, the first term is the freestream velocity contribution, the second term is the doublet contribution, and the third term is the vortex contribution. As  $r_f$  approaches infinity, the infinity freestream boundary conditions for  $u$  and  $v$  are recovered. Also, the doublet term is of higher order in  $1/r_f$  than the vortex term for the case of a lifting airfoil and may be omitted.

The far field pressure is obtained by applying Bernoulli's equation for irrotational incompressible flow and using the nondimensional form for pressure. The result for the far field boundary is

$$p_f(0) = 1/2 [1 - (u_f^2 + v_f^2)] \quad (F.7)$$

The far field boundary conditions of Equations F.6 and F.7 modify the infinity freestream conditions by incorporating effects on the flow of body thickness and circulation at a large but finite distance from the airfoil.

Transonic small disturbance theory for slender bodies and airfoils has similar expressions for the far field conditions. Klunker (101) has obtained an asymptotic solution applicable at large distances from thin airfoils. This form has been used as a numerical outer boundary condition. For the limiting case of incompressible two-dimensional flow, the doublet and vortex strengths are compared below with the general forms found in Equation F.1.

The nondimensional velocity potential doublet in the far field from Klunker becomes

$$\frac{1}{d} = \frac{1}{2\pi} \frac{x}{x^2+y^2} - 2 \int_0^c F(s) ds \quad (F.8)$$

where  $F(s)$  is the airfoil thickness function. The doublet strength is thus

$$2 \int F(s) ds. \quad \text{The NACA four digit airfoil thickness function (67) is}$$

$$F(s) = \frac{cf}{0.2} \left( .2969 \left(\frac{s}{c}\right)^{1/4} - .126 \frac{s}{c} - .3516 \left(\frac{s}{c}\right)^{3/4} + .2843 \left(\frac{s}{c}\right)^{5/4} - .1015 \left(\frac{s}{c}\right)^{7/4} \right) \quad (F.9)$$

where  $c$  is the airfoil chord,  $f$  is the maximum thickness as a fraction of chord and  $s$  is the chord distance,  $0 \leq s \leq c$ .

Substitute the thickness function Equation F.9 into the doublet strength expression and obtain the following doublet strength from transonic small disturbance theory:

$$n_D = 0.685 fc^2 \quad (F.10)$$

For the case of a NACA 0012 airfoil,  $\epsilon_D = 0.0822c^2$ . The corresponding doublet strength in the simple potential flow model from Equation F.1 is  $2\pi(\frac{c}{4})^2$  or  $.3972c^2$ . Klunker points out that the doublet may be neglected in the far field for finite circulation flows because the vortex contribution is of order  $(\frac{1}{r_f})$  compared with an order  $(\frac{1}{r_f})^2$  for the doublet.

The vortex potential term of Klunker for the case of incompressible two-dimensional flow is

$$\phi_v = \frac{\Gamma}{2\pi} \left[ \frac{\pi}{2} \operatorname{sgn}(y) + \tan^{-1}\left(\frac{x}{y}\right) \right] \quad (\text{F.11})$$

where  $\Gamma$  is the clockwise circulation, the inverse tangent function is defined on the interval  $(-\frac{\pi}{2}, \frac{\pi}{2})$ , and the angle within braces is defined clockwise from the negative  $x$  axis. This potential function is identical with the vortex function in Equation F.1 where the clockwise strength  $s$  again  $\Gamma$  and the angular orientation is the right hand polar coordinate  $\theta$  defined counterclockwise from the positive  $x$  axis.

Thus the far field potential for each method differs only in the thickness or doublet term. Furthermore, for flows with finite circulation this difference is negligible because the vortex term dominates.

## APPENDIX G

### NUMERICAL INVISCID FLOW RESULTS

A numerical solution for the inviscid flow over the NACA 0012 airfoil is obtained for comparison with both the Naiver-Stokes computation and the experimental data. The numerical algorithm, developed by Thames (44), which solves Laplace's equation for the stream function in two-dimensional flow is used. The method uses SOR iteration to solve the system of equations written in terms of body-fitted coordinates. The stream function value on the body can either be specified or computed by imposing a given circulation or a Kutta condition.

The stream function equation for two-dimensional flow is

$$\psi_{xx} + \psi_{yy} = 0 \quad (G.1)$$

Rewrite Equation G.1 in terms of the transformed variables in the computational plane using expressions in Appendix A to obtain

$$\alpha \psi_{\xi\xi} - 2\beta \psi_{\xi\eta} + \alpha \psi_{\eta\eta} + \sigma \psi_\eta + \tau \psi_\xi = 0 \quad (G.2)$$

The boundary condition for the stream function on the outer boundary, which is a radius of ten chords, is the freestream value

$$\psi_f = y_f \cos \alpha_L - x_f \sin \alpha_L \quad (G.3a)$$

where  $(x_f, y_f)$  are coordinates on the outer computational boundary and  $\alpha_L$  is the angle of attack. Hodge and Chia (82) have shown by an inviscid analysis that this boundary condition induces an error in lift of less than 1% for angles of attack less than 10°. The boundary condition on the body is

$$\psi_b = \text{constant} \quad (G.3b)$$

The constant can be specified or determined by imposing a given circulation or a Kutta condition. The Kutta condition which matches the upper

and lower trailing edge surface velocities by extrapolation is selected. The details for each option are given by Thames (44).

The derivatives in the transformed Equation G.2 are approximated by central difference formulas found in Appendix E. The resulting system of equations is solved by SOR as described by Thames (44). Solutions are obtained for  $0^\circ$ ,  $5^\circ$ ,  $7.5^\circ$ ,  $9.5^\circ$ , and  $11.5^\circ$  for the NACA 64-12 airfoil section. The body surface pressure coefficients can be calculated from the stream function solution as follows. The body pressure coefficient is defined as

$$C_p = 1 - (u^2 + v^2) \quad (G.4)$$

where at a location on the body  $u$  and  $v$  are the  $x$  and  $y$  components of the flow velocity nondimensionalized by the freestream velocity. Use the definition of the stream function to obtain

$$C_p = 1 - ((\psi_y)^2 + (\psi_x)^2) \quad (G.5)$$

Then rewrite the Equation G.5 in terms of the transformed variables and note that  $\psi_\xi = 0$  on the body to give

$$C_p = 1 - \frac{\alpha}{J} (\psi_\eta)^2 \quad (G.6)$$

where all quantities are evaluated on the body surface. The body pressure coefficients, calculated using Equation G.6 with second order one-sided differences, are plotted in Figures 16, 17, 18, 19, and 33. A typical streamline plot for  $\alpha = 11.5^\circ$  is shown in Figure 40. The numerical inviscid solution is also compared with an analytical solution (67) which uses Theodorsen's (12) method. The excellent agreement is seen in Figure 40 where both solutions are plotted.

## APPENDIX H

### EXPERIMENTAL DATA

This appendix presents the unpublished data which have been obtained experimentally at the Air Force Frank J. Seiler Research Laboratory, USAF Academy, Colorado, by laboratory personnel and used in this work.

Airfoil upper and lower surface mean pressure coefficient measurements for nominal attack angles of  $0^\circ$ ,  $5^\circ$ ,  $8^\circ$ ,  $10^\circ$ , and  $12^\circ$  at a chord Reynolds number of 170,000 are given in Table H.I. The pressure coefficient is defined as the static pressure, relative to freestream static pressure, nondimensionalized by the freestream dynamic pressure as follows:  $C_p = (p - p_\infty) / (\rho u_\infty^2)$ . The two sets of hot wire anemometry velocity field data near the upper and lower airfoil surfaces on designated paths are presented in Table H.II. The velocity field and Reynolds stress  $\bar{u}'\bar{v}'$  data for the near wake region are presented in Table H.III. The data have been nondimensionalized by the measured freestream velocity. The spatial locations in the physical coordinate system for each path are given in Table H.IV where location  $(0,0)$  is the airfoil center and the  $x$  axis lies along the airfoil chord.

The spatial measurement locations correspond with computational grid point locations on constant  $\xi$  lines or  $\tau$  lines in the physical plane. The experimental lead time necessitated the use of the original  $71 \times 44$  grid system. The  $I, J$  index notation designates, however, the point indexing  $(\xi, \tau)$  in the final  $79 \times 44$  grid described in Appendix C.

TABLE H.1 Experimental Surface Pressure Coefficients for NACA 0012  
At Various Angles of Attack, Re = 170,000

x/c LOCATION	Angle of Attack											
	0°	5°	8°	10°	12°		UPPER	LOWER	UPPER	LOWER	UPPER	LOWER
-4.9	0.23	-	-0.74	-	-1.59	-	-2.18	-	0.95	-	-2.58	-
-4.8	-	-0.14	-	0.60	-	0.86	-	-2.29	-	-2.49	-	1.01
-4.75	-0.16	-	-1.20	-	-1.88	-	-1.93	0.72	-	-2.35	0.88	-
-4.5	-0.31	-0.65	-1.10	0.17	-1.58	0.53	-1.74	-	-	-2.00	-	-
-4.0	-0.41	-	-0.95	-	-1.30	-	-0.89	0.16	-0.97	0.25	-	-
-3.0	-0.37	-0.39	-0.69	-0.08	-0.99	0.07	-0.05	-	0.13	-	0.20	-
-2.33	-	-0.32	-	-0.07	-	-0.63	-	-0.73	-	-0.77	-	-
-2.0	-0.34	-	-0.59	-	-0.08	-	0.01	-	0.07	-	-0.56	0.12
-1.47	-	-0.28	-	-0.50	-	-0.50	-	-0.54	-	-0.39	-	-
-1.0	-0.28	-	-0.33	-	-0.37	-	-0.39	-	-0.27	0.04	-0.26	0.07
0.0	-0.21	-	-0.21	-0.01	-0.26	0.02	-0.14	-	-0.14	-	-0.06	-
.1	-0.15	-0.13	-0.21	-0.01	-0.26	0.02	-0.09	-	-0.07	-	-0.06	-
.2	-0.10	-	-0.12	-	-0.14	-	-0.15	-	-0.14	-	-0.14	-
.3	-0.07	-	-0.09	-	-0.09	-	-0.13	-	-0.14	-	-0.13	-
.353	-	0.08	-	-0.02	-	-0.01	-	0.0	-	-0.01	-	-
.367	0.04	-	-0.02	-	-	-	-	-	-	-	-	-

TABLE II Experimental Velocity Field Measurements (Two Sets) Near Surface of NACA 0012 Airfoil

Case A: -5°, Set 1  $Re = 170,000$  and Set 2  $Re = 168,000$ 

J INDEX	PATH I = 49			PATH I = 56			PATH I = 60			
	u <sub>1</sub>	u <sub>2</sub>	v <sub>1</sub>	u <sub>1</sub>	u <sub>2</sub>	v <sub>1</sub>	u <sub>1</sub>	u <sub>2</sub>	v <sub>1</sub>	v <sub>2</sub>
15	-	-	-	-	1.17*	-	-.18*	-	-	-.17*
17	1.33	-	-.0	-	1.17	1.16	-.16	1.09*	1.07*	-.16*
19	1.30	1.27	.01	.01	1.17	1.16	-.14	1.09	1.07	-.15
21	1.27	1.24	.02	.02	1.16	1.14	-.13	1.09	1.08	-.14
23	-	1.20	-.03	-.03	1.15	1.13	-.1	1.08	1.07	-.12
25	-	-	-	-	-	-	-	1.08	1.07	-.1

J INDEX	PATH I = 66			PATH I = 12		
	u <sub>1</sub>	u <sub>2</sub>	v <sub>1</sub>	u <sub>1</sub>	u <sub>2</sub>	v <sub>1</sub>
13	-	-	-	-	1.0	-
15	-	.93*	-	-.16*	-.99	0.
17	1.01*	1.0*	-.16*	-.15*	.99	-.99
19	1.01	1.01	-.15	-.14	.99	-.99
21	1.02	1.01	-.13	-.13	.99	-.98
23	1.02	1.01	-.12	-.12	-	-.99
25	1.02	1.02	-.1	-.1	-	-.02

\*Large RMS values occurred

TABLE H.J.II (Continued)

Case B: 8, Set 1 Re = 172,000 and Set 2 Re = 166,000

J INDEX	PATH I = 49			PATH I = 56			PATH I = 60		
	u <sub>1</sub>	u <sub>2</sub>	v <sub>1</sub>	u <sub>1</sub>	u <sub>2</sub>	v <sub>1</sub>	u <sub>1</sub>	u <sub>2</sub>	v <sub>1</sub>
15	-	-	-	1.11*	-	.20*	-	.98*	-
17	1.42	-	-.08	1.18	1.14	-.19	-.18	1.09*	1.06*
19	1.39	1.33	-.05	1.18	1.14	-.18	-.17	1.09	1.06
21	1.34	1.50	-.03	1.17	1.14	-.16	-.15	1.09	1.06
23	-	1.25	0.	1.15	1.12	-.14	-.13	1.09	1.06
25	-	-	-	-	-	-	-	1.08	1.06

J INDEX	PATH I = 66			PATH I = 72		
	u <sub>1</sub>	u <sub>2</sub>	v <sub>1</sub>	u <sub>1</sub>	u <sub>2</sub>	v <sub>1</sub>
13	-	-	-	-	.98	-.03
15	-	.82*	-	-.18*	-	-.03
17	.99*	.97*	-.19*	-.18*	.98	.96
19	1.0	.98	-.18	-.17	.98	.96
21	1.01	.99	-.16	-.15	.99	.96
23	1.02	.99	-.14	-.14	-	-.04
25	1.02	1.0	-.12	-.12	.96	-

\*Large RMS values occurred.

TABLE II, II (Continued)

Case C:  $\epsilon = 10$ , Set 1 Re = 170,000 and Set 2 Re = 170,000

J TNDFX	PATH I = 49			PATH I = 56			PATH I = 60					
	$u_1$	$u_{\infty}$	$v_1$	$v_2$	$u_1$	$u_{\infty}$	$v_1$	$v_2$	$u_1$	$u_{\infty}$	$v_1$	$v_2$
15	-	-	-	-	1.07*	-	-	-	-	-	.97*	-
17	1.40	-	-.11	-	1.17	1.15	-.17	-.20	1.08*	1.06*	-.23*	-.21*
19	1.39	1.35	-.09	-.09	1.17	1.15	-.20	-.19	1.08	1.06	-.21	-.20
21	1.37	1.32	-.07	-.06	1.16	1.15	-.18	-.17	1.09	1.07	-.19	-.18
23	-	1.27	-	-.05	1.16	1.13	-.16	-.15	1.09	1.06	-.17	-.16
25	-	-	-	-	-	-	-	-	1.08	1.06	-.14	-.14
PATH I = 66												
15	-	-	-	-	-	-	.98	-	-.05	-	-	
17	-	.75*	-	-	-.17*	-	-	.97	-	-.05	-	
19	.92*	.96*	-.19*	-.19*	-.19*	-	.98	.97	-.06	-.05	-	
21	.99	.97	-.19	-.18	-.18	-	.99	.97	-.06	-.05	-	
23	1.0	.99	-.17	-.17	-.17	-	.99	.97	-.06	-.05	-	
25	1.01	.99	-.16	-.15	-.15	-	.97	-	-.05	-	-	
27	1.02	1.0	-.14	-.15	-.15	-	-	-	-	-	-	

\*Large negative values occurred.

TABLE II. II (Continued)

Case 0:  $\tau = 12$ , Set 1 Re = 170,000 and Set 2 Re = 170,000

T ND X	PATH I = 49			PATH I = 56			PATH I = 60					
	$u_1$	$u_2$	$v_1$	$v_2$	$u_1$	$u_2$	$v_1$	$v_2$	$u_1$	$u_2$	$v_1$	$v_2$
15	-	-	-	-	.84*	-	-.20*	-	-	.80*	-	-.20*
17	1.43*	-	-.16*	-	1.12*	1.14*	-.24*	-.24*	1.01*	1.0*	-.24*	-.24*
19	1.41	1.38	-.14	-.13	1.17	1.15	-.24	-.23	1.07	1.06	-.23	-.23
21	1.39	1.35	-.11	-.10	1.17	1.15	-.21	-.20	1.08	1.06	-.21	-.21
23	-	1.32	-	-.07	1.16	1.14	-.18	-.18	1.09	1.06	-.18	-.18
25	-	-	-	-	-	-	-	-	1.08	1.06	-.16	-.16

T ND X	PATH I = 66			PATH I = 72				
	$u_1$	$u_2$	$v_1$	$v_2$	$u_1$	$u_2$		
15	-	-	-	-	.99	-	-.08	
17	-	.58*	-	-.13*	-	.97	-	-.07
19	.79*	.78*	-.16*	-.18*	.98	.97	-.08	-.07
21	.98*	.97*	-.10*	-.20*	.98	.97	-.08	-.07
23	.99	.98	-.19	-.18	.98	.97	-.08	-.07
25	1.01	.99	-.17	-.17	-	.96	-	-.07

\*Large positive values occurred.

TABLE II. Experimental Velocity Field and Reynolds Stress<sup>4</sup> Measurements in the Near Wake of  
NACA 0012 Airfoil

Case A:  $\delta = 5^\circ$ , Set 1 Re = 170,000 and Set 2 Re = 168,000

I INDEX	PATH J = $15 \frac{u^* v^*}{u^* v^*}$			PATH J = $21 \frac{u^* v^*}{u^* v^*}$			PATH J = $27 \frac{u^* v^*}{u^* v^*}$			PATH J = 33 $\frac{u^* v^*}{u^* v^*}$			
	$u_2$	$v_2$	$u_2$	$v_2$	$u_2$	$v_2$	$u_2$	$v_2$	$u_2$	$v_2$	$u_2$	$v_2$	
66	.94	-.16	-.0005	1.01	-.13	0.	1.01	-.08	0.	1.0	1.0	-.03	0.
67	.91	-.16	-.0006	1.0	-.13	0.	1.01	-.08	0.	1.01	1.0	-.04	-.03
68	.90	-.15	-.0006	.99	-.13	0.	1.01	-.08	0.	1.01	.99	-.04	-.04
69	.88	-.15	-.0008	.98	-.12	0.	1.0	-.08	0.	1.0	1.0	-.04	0.
70	.83	-.15	-.001	.97	-.12	0.	.99	-.08	0.	1.01	.99	-.04	-.04
71	-	-	-	.96	-.11	0.	.99	-.07	0.	1.01	.99	-.05	-.05
72	-	-	-	.92	-.1	0.	.99	-.07	0.	1.01	1.0	-.05	0.
75	-	-	-	.77	-.08	-.002	.97	-.05	-.0005	1.02	.99	-.05	0.
79	.33	-.09	-.006	.61	-.05	.001	.78	-.03	.001	.92	.88	-.05	0.
4	.94	0.	-.0002	.87	-.02	.003	.98	-.06	0.	1.01	1.0	-.05	-.05
6	-	-	-	.94	-.03	0.	.98	-.05	0.	1.01	.99	-.04	-.04
7	-	-	-	.95	-.02	0.	.99	-.05	0.	.99	.98	-.04	0.
8	.97	0.	0.	.96	-.02	0.	.98	-.04	0.	.99	.98	-.03	0.
9	.98	0.	0.	.97	-.02	0.	.99	-.03	0.	1.0	.99	-.03	0.
I INDEX PATH I = 75													
17	.62	-.12	-.002	.35	-.10	-.006	.62	.05	.01				
19	.70	-.11	-.002	.49	-.06	-.001	.79	.02	.007				
21	.78	-.09	-.002	.60	-.03	.003	.88	-.03	.003				
23	.85	-.07	-.001	.67	-.03	.003	.94	-.05	.0005				
25	.93	-.06	-.0009	.73	-.04	.002	.97	-.06	0.				
27	.96	-.05	-.0005	.78	-.04	.001	.98	-.06	0.				
29	.98	-.05	-.0001	.82	-.05	.0007	.99	-.06	0.				
31	.99	-.05	0.	.83	-.04	.0004	.99	-.06	0.				
33	.99	-.05	0.	.99	-.05	.0003	.99	-.05	0.				
I INDEX PATH I = 4													
Set 2 only.													

TABLE II, III (Continued)

Case B:  $\delta = 8$ , Set 1 Re 172,000 and Set 2 Re 166,000

INDEX	PATH I		PATH J		PATH I		PATH J		PATH I		PATH J		
	$\frac{u_1}{u'v'}$	$\frac{v_1}{u'v'}$	$\frac{u_2}{u'v'}$	$\frac{v_2}{u'v'}$	$\frac{u_1}{u'v'}$	$\frac{v_1}{u'v'}$	$\frac{u_2}{u'v'}$	$\frac{v_2}{u'v'}$	$\frac{u_1}{u'v'}$	$\frac{v_1}{u'v'}$	$\frac{u_2}{u'v'}$	$\frac{v_2}{u'v'}$	
66	.82	-.18	-.001	.99	-.15	0.	1.0	-.1	0.	1.0	.98	-.05	-.04
67	.80	-.17	-.002	.98	-.15	0.	1.0	-.1	0.	1.01	.99	-.05	-.05
68	.75	-.16	-.002	.97	-.15	0.	.99	-.1	0.	1.01	.99	-.05	-.05
69	.73	-.15	-.002	.96	-.14	0.	.98	-.1	0.	1.01	.98	-.06	-.06
70	.64	-.14	-.002	.95	-.14	0.	.98	-.1	0.	1.01	.98	-.06	-.06
71	—	—	—	.94	-.13	0.	.97	-.1	0.	1.02	.98	-.07	-.07
72	—	—	—	.84	-.12	—	.97	-.09	0.	1.01	.98	-.07	-.07
73	—	—	—	.61	-.1	—	.88	-.09	—	.001	1.0	.97	-.07
74	.41	.05	.0006	.74	-.09	.0018	.91	-.07	.001	1.01	.98	-.07	-.07
75	.94	-.04	0.	.94	-.06	0.	.97	-.07	0.	1.01	.98	-.06	0.
76	—	—	—	.94	-.05	0.	.97	-.07	0.	1.0	.97	-.05	0.
77	—	—	—	.94	-.05	0.	.97	-.06	0.	.99	.97	-.05	0.
78	.95	-.04	0.	.95	-.05	0.	.97	-.06	0.	.99	.97	-.04	0.
79	.95	-.04	0.	.96	-.05	0.	.97	-.05	0.	1.0	.97	-.05	0.
80	—	—	—	—	—	—	—	—	—	—	—	—	—
INDEX	PATH I		PATH J		PATH I		PATH J		PATH I		PATH J		
81	.58	-.08	-.004	.59	.03	.0005	.93	-.04	0.	.93	-.04	0.	—
82	.50	-.08	-.003	.58	.002	.001	.94	-.05	0.	.94	-.05	0.	—
83	.61	-.1	-.003	.79	-.02	.002	.94	-.06	0.	.94	-.06	0.	—
84	.71	-.1	-.002	.86	-.05	.002	.95	-.07	0.	.95	-.07	0.	—
85	.81	-.1	-.002	.87	-.05	.002	.96	-.07	0.	.96	-.07	0.	—
86	.91	-.09	-.0007	.9	-.06	.001	.97	-.07	0.	.97	-.07	0.	—
87	.93	-.08	-.0003	.93	-.07	.0007	.97	-.07	0.	.97	-.07	0.	—
88	.97	-.08	0.	.96	-.07	.0003	.97	-.06	0.	.97	-.06	0.	—
89	.98	-.07	0.	.97	-.06	0.	.97	-.05	0.	.97	-.05	0.	—

TABLE H, III (Continued)

Case C:  $Re = 10^4$ , Set 1  $pe$  170,000 and Set 2  $Re$  170,000

I	TNDFX	PATH J = 15 $\frac{u^*v^*}{u^*v^*}$			PATH J = 21 $\frac{u^*v^*}{u^*v^*}$			PATH J = 27 $\frac{u^*v^*}{u^*v^*}$			PATH J = 33 $\frac{u^*v^*}{u^*v^*}$		
		$u_1$	$v_1$	$u_2$	$v_2$	$u_1$	$v_1$	$u_2$	$v_2$	$u_1$	$v_1$	$u_2$	$v_2$
66	.73	-.17	-.009	.99	-.16	0.	1.01	-.11	0.	1.01	.99	-.05	0.
67	.70	-.16	-.009	.98	-.16	0.	1.0	-.11	0.	1.01	.99	-.06	0.
68	.64	-.15	-.005	.97	-.15	0.	.99	-.11	0.	1.01	.99	-.07	0.
69	.59	-.13	-.005	.95	-.15	0.	.98	-.11	0.	1.01	.99	-.07	0.
70	.50	-.12	-.005	.95	-.14	0.	.98	-.11	0.	1.01	.99	-.07	0.
71	-	-	-	.93	-.14	-.0009	.98	-.1	0.	1.01	.98	-.08	0.
72	-	-	-	.73	-.12	-.002	.97	-.1	0.	1.01	.98	-.08	0.
73	-	-	-	.45	-.07	-.003	.76	-.09	-.002	.91	.90	-.07	-.0008
74	.93	-.04	0.	.95	-.07	0.	.96	-.09	.0002	1.01	.98	-.07	0.
75	-	-	-	.95	-.07	0.	.95	-.08	0.	1.0	.97	-.07	0.
76	-	-	-	.95	-.07	0.	.97	-.07	0.	.99	.97	-.06	0.
77	-	-	-	.95	-.06	0.	.97	-.07	0.	.99	.97	-.05	0.
78	.95	-.05	0.	.96	-.06	0.	.97	-.06	0.	.99	.97	-.05	0.
79	.95	-.05	0.	.97	-.06	0.	.97	-.06	0.	1.0	.97	-.04	0.
J	TNDFX	PATH I	75	PATH I	79	PATH I	79	PATH I	79	PATH I	79	PATH I	79
17	.27	-.02	-.0006	.86	-.02	0.	.95	-.06	0.	.95	-.06	0.	.95
19	.54	-.04	-.002	.94	-.06	0.	.95	-.06	0.	.95	-.06	0.	.95
21	.46	-.07	-.003	.95	-.07	0.	.95	-.07	0.	.95	-.07	0.	.95
23	.57	-.09	-.003	.95	-.07	0.	.96	-.08	0.	.96	-.08	0.	.96
25	.70	-.09	-.003	.96	-.08	.0002	.97	-.08	0.	.97	-.08	0.	.97
27	.77	-.09	-.002	.96	-.09	.0002	.97	-.08	0.	.97	-.08	0.	.97
29	.84	-.09	-.002	.98	-.08	.0001	.97	-.08	0.	.97	-.08	0.	.97
31	.87	-.07	-.001	.98	-.08	0.	.98	-.07	0.	.98	-.07	0.	.98
33	.90	-.07	-.0008	.98	-.07	0.	.98	-.07	0.	.98	-.07	0.	.98

Case D:  $\epsilon = 1.12$ , set 1 Re = 170,000 and set 2 Re = 170,000

TABLE H. III (Continued)

J INDEX	PATH I = 75	PATH I = 79				PATH I = 4			
		$\frac{u_1}{u'v'}$	$\frac{v_1}{u'v'}$	$\frac{u_2}{u'v'}$	$\frac{v_2}{u'v'}$	$\frac{u_1}{u'v'}$	$\frac{v_1}{u'v'}$	$\frac{u_2}{u'v'}$	$\frac{v_2}{u'v'}$
PATH J = 15									
66	.57	-.15	-.004	.99	-.18	0.	1.0	-.13	0.
67	.52	-.13	-.004	.97	-.18	0.	1.0	-.13	0.
68	.47	-.11	-.004	.97	-.17	0.	.99	-.13	0.
69	.44	-.11	-.004	.95	-.17	0.	.98	-.13	0.
70	.37*	-.1	-.004	.88	-.17	-.001	.98	-.13	0.
71	-	-	-	.74	-.14	-.003	.97	-.12	0.
72	-	-	-	.55	-.1	-.004	.94	-.12	-.0006
75	-	-	-	.32*	-.06	-.002	.61	-.08	-.002
79	.72	0.	.0002	.96	-.06	.0002	.97	-.09	.0002
4	.96	-.07	0.	.96	-.08	0.	.97	-.09	0.
6	-	-	-	.96	-.08	0.	.97	-.08	0.
7	-	-	-	.96	-.08	0.	.96	-.08	0.
8	.97	-.07	0.	.96	-.08	0.	.96	-.08	0.
9	.97	-.07	0.	.96	-.08	0.	.96	-.07	0.
PATH J = 21									
17	.21*	-.02	-.001	.65	.01	.0003	.96	-.07	0.
19	.26*	-.04	-.002	.90	-.03	.0003	.96	-.07	0.
21	.31*	-.05	-.005	.95	-.06	.0003	.96	-.08	0.
25	.39	-.06	-.003	.96	-.08	.0004	.96	-.08	0.
25	.50	-.08	-.003	.95	-.09	.0003	.96	-.09	0.
27	.59	-.08	-.001	.96	-.09	.0003	.96	-.09	0.
29	.69	-.07	-.0009	.97	-.09	0.	.97	-.09	0.
31	.75	-.07	-.0003	.97	-.09	0.	.96	-.08	0.
33	.79	-.08	-.0002	.97	-.08	0.	.97	-.07	0.
PATH J = 27									
144									

\* possible reverse flow occurred.

TABLE II, IV Physical Coordinate Grid Locations for Experimental Data Measurements

J INDEX	PATH I = 49		PATH I = 56		PATH I = 60	
	X/C	Y/C	X/C	Y/C	X/C	Y/C
15	-.321	.073	-.001	.079	.19	.068
17	-.322	.085	-.002	.096	.191	.087
19	-.325	.105	-.003	.124	.191	.117
21	-.352	.137	-.004	.169	.194	.165
23	-.345	.187	-.006	.237	.201	.236
25	-.373	.261	-.009	.339	.216	.338
PATH I = 66						
13	.414	.034	.414	.034	-.034	-.034
15	.415	.046	.415	.046	-.046	-.046
17	.418	.065	.418	.065	-.065	-.065
19	.424	.094	.424	.094	-.094	-.094
21	.438	.134	.438	.134	-.134	-.134
23	.464	.189	.464	.189	-.189	-.189
25	.510	.262	.510	.262	-.262	-.262

TABLE H. IV (Continued)

<i>I</i>	INDFX	PATH J = 15		PATH J = 21		PATH J = 27		PATH J = 33	
		x/c	y/c	x/c	y/c	x/c	y/c	x/c	y/c
66	.415	.046	.438	.134	.585	.360	.149	.928	
67	.442	.042	.469	.124	.631	.326	.1238	.832	
68	.465	.039	.496	.112	.672	.288	.1316	.729	
69	.483	.035	.520	.098	.708	.246	.1384	.619	
70	.497	.029	.540	.081	.737	.201	.1441	.502	
71	.507	.023	.555	.063	.761	.153	.1486	.381	
72	.513	.016	.566	.043	.778	.103	.1518	.256	
75	.517	.008	.573	.022	.789	.052	.1537	.129	
79	.518	0.	.575	0.	.792	0.	.1544	0.	
4	.517	-.008	.573	-.022	.789	-.052	.1537	-.129	
6	.513	-.016	.566	-.043	.778	-.103	.1518	-.256	
7	.507	-.023	.555	-.063	.761	-.153	.1486	-.381	
8	.497	-.029	.540	-.081	.737	-.201	.1441	-.502	
9	.483	-.035	.520	-.098	.708	-.246	.1384	-.619	
<i>J</i>	INDFX	PATH I = 75		PATH I = 79		PATH I = 4			
		x/c	y/c	x/c	y/c	x/c	y/c	x/c	y/c
17	.538	.011	.530	0.	.528	-.011			
19	.545	.016	.547	0.	.545	-.016			
21	.573	.022	.575	0.	.573	-.022			
23	.617	.029	.619	0.	.617	-.029			
25	.684	.039	.687	0.	.684	-.039			
27	.789	.052	.792	0.	.789	-.052			
29	.947	.070	.951	0.	.947	-.070			
31	1.184	.094	1.189	0.	1.184	-.094			
33	1.537	.129	1.544	0.	1.537	-.129			

## VITA

Harwood Allan Hegna was born on 30 January 1947 in Minneapolis, Minnesota. He graduated from Washburn High School in Minneapolis in 1965 and attended the University of Minnesota from which he was conferred the degree of Bachelor of Aeronautical Engineering with High Distinction in June 1969. He continued his education in the Graduate School of the University of Minnesota and received a Master of Science in Aeronautical Engineering degree in December 1971 with a thesis entitled, "The Rarefied Gas Flow Through a Slit". He was commissioned in the USAF through the ROTC program in June 1972 and entered active duty in August 1972. He served as an engineering plans and programs manager for the Ogden Air Logistics Center, Hill AFB, Utah. While on active duty, he completed the requirements and was awarded the degree of Master of Science in Mechanical Engineering from the University of Minnesota in March 1973. He attended Squadron Officer School in residence prior to his entering the School of Engineering, Air Force Institute of Technology in September 1976. He was married to Helen Ruth Henson of Orlando, Florida, on 25 August 1979. He is currently assigned to the Air Force Wright Aeronautical Laboratories in the Computational Aerodynamics Group.

Permanent Address 1824 Commerce Blvd.  
Orlando, Florida 32807

UNCLASSIFIED

SECURITY CLASSIFICATION OF THIS PAGE (When Data Entered)

REPORT DOCUMENTATION PAGE		READ INSTRUCTIONS BEFORE COMPLETING FORM
1. REPORT NUMBER AFIT/DS/AA/81-1	2. GOVT ACCESSION NO. 1D-H100 824	3. RECIPIENT'S CATALOG NUMBER
4. TITLE (and Subtitle)  THE NUMERICAL SOLUTION OF INCOMPRESSIBLE TURBULENT FLOW OVER AIRFOILS		5. TYPE OF REPORT & PERIOD COVERED  PhD Dissertation
		6. PERFORMING ORG. REPORT NUMBER
7. AUTHOR(s)  Harwood A. Hegna Captain		8. CONTRACT OR GRANT NUMBER(s)
9. PERFORMING ORGANIZATION NAME AND ADDRESS  Air Force Institute of Technology (AFIT-EN) Wright-Patterson AFB, Ohio 45433		10. PROGRAM ELEMENT, PROJECT, TASK AREA & WORK UNIT NUMBERS  2307N603
11. CONTROLLING OFFICE NAME AND ADDRESS  Air Force Wright Aeronautical Laboratories Flight Dynamics Laboratory Wright-Patterson AFB, Ohio 45433		12. REPORT DATE  February 1981
14. MONITORING AGENCY NAME & ADDRESS (if different from Controlling Office)		13. NUMBER OF PAGES  168
		15. SECURITY CLASS. (of this report)  Unclassified
		15a. DECLASSIFICATION/DOWNGRADING SCHEDULE
16. DISTRIBUTION STATEMENT (of this Report)  Approved for public release; distribution unlimited		
 17. DISTRIBUTION STATEMENT (for the abstract entered in Block 20, if different from Report) <b>FREDRIC C. LYNCH, Major, USAF</b> <b>Director of Public Affairs</b> Air Force Institute of Technology (ATC) Wright-Patterson AFB, OH 45433		
18. SUPPLEMENTARY NOTES  25 MAR 1981		
19. KEY WORDS (Continue on reverse side if necessary and identify by block number)  Aerodynamics Airfoils Viscous Flow Navier-Stokes Numerical Methods		
20. ABSTRACT (Continue on reverse side if necessary and identify by block number)  - Numerical solutions are obtained for two-dimensional incompressible turbulent viscous flow over airfoils of arbitrary geometry. A body-fitted coordinate system is numerically transformed to a rectangular grid in the computational plane. The time dependent Reynolds averaged Navier-Stokes equations in the primitive variables of velocity and pressure are used. Turbulence is modelled with an algebraic eddy viscosity technique modified for separated adverse pressure gradient flows. The set of transformed partial differential equations is solved		

UNCLASSIFIED

SECURITY CLASSIFICATION OF THIS PAGE(When Data Entered)

with an implicit finite difference method. Numerical solutions for a NACA 0012 airfoil near stall at a chord Reynolds number of 170,000 are favorably compared with surface pressure and velocity field measurements. A small laminar separation bubble near the suction pressure peak is observed. Computed lift and drag coefficients agree well with experimental values.

UNCLASSIFIED

SECURITY CLASSIFICATION OF THIS PAGE(When Data Entered)

